SIZE REDUCTION OF AN UWB LOW-PROFILE SPIRAL ANTENNA

DISSERTATION

Presented in Partial Fulfillment of the Requirements for

the Degree Doctor of Philosophy in the

Graduate School of The Ohio State University

By

Brad A. Kramer, M.S., B.S.

* * * * *

The Ohio State University

2007

Dissertation Committee:

Professor John L. Volakis, Adviser

Adjunct Professor Chi-Chih Chen

Associate Professor Fernando L. Teixeira

Approved by

Adviser

Graduate Program in
Electrical and Computer
Engineering

ABSTRACT

Fundamental physical limitations restrict antenna performance based on its electrical size alone. These fundamental limitations are of the utmost importance since the minimum size needed to achieve a particular figure of merit can be determined from them. In this dissertation, the physical limitations on the size reduction of a broadband antenna is examined theoretically and experimentally. This is in contrast to previous research that focused on narrowband antennas. Specifically, size reduction using antenna miniaturization techniques is considered and explored through the application of high-contrast material and reactive loading. A particular example is the miniaturization of a broadband spiral using readily available high-contrast dielectrics and a novel inductive loading technique. Using either dielectric or inductive loading, it is shown that the size can be reduced by more than a factor of two which is close to the observed theoretical limit.

To enable the realization of a conformal antenna without the loss of the antenna's broadband characteristics, a novel ground plane is introduced. The proposed ground plane consists of a traditional metallic ground plane coated with a layer of ferrite material. It is shown that the ferrite coated ground plane minimizes the negative effects that occur when the spacing between a traditional metallic ground plane and antenna becomes electrically small.

ACKNOWLEDGMENTS

I would like to acknowledge all of my committee members, especially my advisor, Professor John Volakis for his guidance and advice. I would also like to thank Dr. Chen and Ming Lee for the interesting discussions and insight on antennas and other topics. Additionally, I would like to thank John Moniz, program officer at the Office of Naval Research, for sponsoring this work. Lastly, I would like to thank the staff and fellow students of the ElectroScience Laboratory for their support.

VITA

August 19, 1978	Born - Newark, Ohio
March, 2002	Bachelor of Science in Electrical and Computer Engineering The Ohio State University
May, 2003 - present	Graduate Research Associate, The Ohio State University - Columbus, OH
December, 2004	Masters of Science in Electrical and Computer Engineering The Ohio State University

FIELDS OF STUDY

Major Field: Electrical Engineering

Studies in:

Electromagnetics
Communications and Signal Processing

TABLE OF CONTENTS

Page

LIST OF TABLES

Table **Page**

LIST OF FIGURES

Figure **Page**

CHAPTER 1

INTRODUCTION

1.1 Motivation, Challenges and Objective

A common approach used to cover a large frequency range which encompasses many different communication systems is to employ a separate antenna for each system. An advantage of this approach is that it meets the specific needs of each communication system. However, when a platform such as an airplane, ship or automobile requires the use of many communication systems, this approach has several problems such as space, payload, cost and electromagnetic compatibility/interference (EMC/EMI). Therefore, there is significant interest in antennas that are smaller in size (aperture and profile) and multi-functional. In the commercial sector, for instance, the interest originates from consumer demand for multimedia and wireless applications. This is evident in the automotive industry where consumers expect automobiles to be enabled with the latest multimedia and wireless products which can operate from AM radio broadcast frequencies up to 2.5 GHz for Bluetooth applications [7]. The antennas must also be aesthetically pleasing implying a need for small and concealable antennas. There is also significant interest from the defense sector for a variety of reasons. One of the most notable is the military's reliance on

radio systems that operate below 100 MHz for long distance communication. At these frequencies, the wavelength is several meters ($\approx$ 3 meters at 100 MHz) making the physical antenna size prohibitively large for most applications and unacceptable for small platforms such as unmanned aerial vehicles (UAV). Currently, large airplanes and ground vehicles rely on blade and whip antennas which are highly visible and obtrusive. Thus, there is a multitude of reasons for developing small and low-profile broadband antennas to address the needs of smaller vehicles but to also deal with practical aspects relating to cost, integration and realizability.

In designing an antenna that meets the above requirements, there are several challenges that must be dealt with. First and foremost, the antenna must have sufficient bandwidth to facilitate the integration of multiple antennas into a single aperture. Since the applications of interest require bandwidths in excess of 100:1, this work focuses on ultra wide-band antennas (UWB) such as the spiral antenna. Since the spiral antenna belongs to the class of frequency independent antennas, it is are easily capable of bandwidths greater than 10:1 [8]. Such antennas are considered frequency independent because their pattern, impedance and other parameters vary little with frequency as compared to a multi-band antenna which can exhibit considerable variation. These characteristics make the spiral an ideal candidate for replacing a variety of antennas.

Even though the spiral has sufficient bandwidth, its size is too large for low frequency applications just like any other type of antenna. To reduce the size of the spiral, one must address the issue of deteriorating performance as the antenna becomes smaller. Generally, this issue is addressed by using antenna miniaturization techniques such as material and reactive loading. The basic idea is to increase the

antenna's electrical size without increasing its physical size. This can be accomplished by using high-contrast materials or reactive loading to reduce the phase velocity of the principle wave guided by the antenna. This effectively makes the antenna appear electrically larger and improves its performance at frequencies where it is electrically small. Each miniaturization approach has its own associated challenges and performance trade-offs. One of the main challenges with using dielectric or magnetic material is maintaining a reasonable antenna weight while achieving the desired miniaturization. This becomes an issue when large miniaturization factors are desired because a sufficient volume of high-contrast material is needed to achieve such miniaturization factors. Since these materials have a high density, the antenna weight can increase appreciably. Therefore, high-contrast materials must be used sparingly to maintain a reasonable weight. As an alternative, reactive loading can be used to achieve similar miniaturization factors with minimal increase in weight. Reactive loading refers to the enhancement of the capacitance and/or inductance of the antenna structure without using dielectric or magnetic materials. This usually involves modifying the antenna geometry in such a way that the local stored electric or magnetic energy density is increased. For instance, a common example of capacitive loading is the top loaded monopole [9]. For inductive loading, the normal mode helix and the meander-line antenna are the two most common examples [10,11]. The main issue with reactive loading is its implementation and integration into the antenna. For some antennas, it can be very difficult if not impossible to implement capacitive and/or inductive loading.

The last challenge that must be addressed is that of minimizing the antenna profile. This issue occurs because unidirectional radiation is required in most applications

necessitating the use of a metallic cavity or ground plane. Furthermore, the metallic back plane is also useful for shielding the electronics mounted behind the aperture. However, the presence of the ground plane has a significant impact on the antenna's performance depending upon the electrical separation between them. At frequencies where the separation is small, the metallic ground plane effectively shorts out the antenna leading to an increase in mismatch loss which reduces the realized gain and bandwidth of the antenna. This issue is traditionally dealt with by placing the ground plane a $\lambda/4$ away from the antenna at the lowest operating frequency. However, the resulting profile is impractical or intolerable for most applications. For the broadband spiral, one would ideally like to replace the metallic ground plane (perfect electric conductor) with a perfect magnetic conductor (PMC) which can be placed as close to the antenna aperture as desired without negative consequences. Such a conductor does not exist in nature but it can be emulated to an extent by using an artificial magnetic conductor (AMC) or some other kind of high impedance surface [5, 6]. However, these surfaces exhibit a multiband behavior and have bandwidth limitations making them unsuitable for broadband miniaturized apertures. In addition, since an AMC is composed of a frequency selective surface (FSS), the elements which make up the FSS must be at or near resonance to produce the desired effect. Therefore, for a miniature antenna operating in the VHF or UHF band, the element size can make the AMC surface larger than the antenna aperture which is extremely problematic and impractical.

In light of the aforementioned challenges, this thesis is organized into six chapters beginning with a chapter that discusses the fundamental limitations of electrically small antennas. Performance issues with electrically small antennas have been

typically discussed from the perspective of band-pass type antennas (narrow band). However, here the discussion is extended to include high-pass type antennas such as the spiral. In doing so, the extent to which a broadband antenna can be miniaturized is established in theory. In Chapter 3, the general concept of antenna miniaturization using inductive and/or capacitive loading is presented. The actual implementation of capacitive (dielectric) loading and inductive loading is treated separately in Chapters 4 and 5 respectively. Specifically, Chapter 4 examines the use of readily available dielectric materials for miniaturizing a spiral antenna where as Chapter 5 discusses the development of a novel method for implementing inductive loading for the spiral antenna. The final chapter addresses the low-profile issue by introducing a ferrite coated ground plane.

CHAPTER 2

FUNDAMENTAL LIMITATIONS OF ELECTRICALLY SMALL ANTENNAS

2.1 Introduction

An electrically small antenna is often defined using the concept of the radian sphere [12]. The radian sphere is a hypothetical sphere whose diameter 2a is equal to the largest linear dimension of the antenna that it encloses. When the electrical size ka (throughout $k = 2\pi/\lambda$) of the radian sphere is less than one (or $a \leq \lambda/2\pi$), the antenna enclosed by the sphere is considered to be electrically small. Therefore, any dipole-type antenna of length less than λ/π or a loop type antenna with a circumference less than λ is an electrically small antenna. These antennas exhibit low radiation resistance, high reactance, low efficiency and narrow bandwidth, all of which limit their performance. Such limitations have been a subject of interest since the early 1900's and many researchers have contributed to the goal of determining the optimum performance of an antenna in terms of directivity and impedance bandwidth. In this chapter, past research on this subject is reviewed and discussed with particular emphasis on how it applies to electrically small antennas. The presentation is in a predominately historical manner but not necessarily in chronological order.

In the following, the research related to super-directive antennas is discussed first. Essentially, the discussion on the fundamental limitations of antennas began with the research in this area. From this work, the idea of using a quality factor (Q) to quantify the physical limitations of an antenna was introduced. In section 2.3, the seminal work on radiation Q by Chu is presented and its importance in defining the limits on directivity and impedance bandwidth for an electrically small antenna is demonstrated in subsequent sections. The last section of this chapter builds on these fundamental limitations to establish a more useful limit for electrically small broadband antennas. It is remarked that radiation efficiency is not discussed because, unlike other quantities, the issue of radiation efficiency cannot be generalized to the extent that it only depends upon electrical size. The radiation efficiency inherently depends upon frequency dependent loss mechanisms and requires specific knowledge of the antenna structure and constituting materials.

2.2 Directivity Limit for an Antenna of Arbitrary Size

In the early 1900's a discussion began about whether it was possible for an aperture to have infinite directivity if the amplitude and phase of the current distribution is chosen properly. In one of the first published articles on this subject, Schelkunoff derived a current distribution for a linear array that could achieve superdirectivity [13]. That is, he determined the current distribution which resulted in a higher directivity than if the array was excited with uniform amplitude and linear phase (constant or progressive across the aperture). In later works, Taylor, Chu and Harrington showed that there is no mathematical limit to the directivity of an antenna of given size [2, 3, 14]. They demonstrated this by describing the radiated field from

an arbitrary source distribution inside a sphere of finite radius using a complete set of orthogonal spherical wave modes (TM and TE modes). In doing so, the directivity could be written in terms of the spherical wave mode coefficients A_{mn} (TM_{mn} modes) and B_{mn} (TE_{mn} modes) as follows

$$\begin{aligned} D(\theta,\phi) &= \frac{4\pi r^2\sqrt{\epsilon/\mu}\,|E(\theta,\phi)|^2}{P_{rad}} \\ &= \frac{\left|\sum_{m,n} j^n\left[A_{mn}P_n^m(cos\theta)+m\sqrt{\mu/\epsilon}B_{mn}P_n^m(cos\theta)\right]\right|^2}{\sum_{m,n}\left[|A_{mn}|^2+\frac{\mu}{\epsilon}|B_{mn}|^2\right]\frac{n(n+1)(n+m)!}{\epsilon_m(2n+1)(n-m)!}} \end{aligned} \tag{2.1}$$

where P_n^m is the Legendre function of the first kind, $\epsilon_m = 1$ for $m = 0$ and $\epsilon_m = 2$ for $m > 0$. With proper choice of spherical wave mode coefficients, they showed that the highest possible gain that could be achieved using spherical wave modes of order $n \leq N$ is

$$D_{max} = \sum_{n=1}^{N}(2n+1) = N^2 + 2N. \tag{2.2}$$

Therefore, the directivity is unbounded as long as the number of modes used to express the field is unrestricted, regardless of antenna size. The reason for this unbounded directivity stems from the inherent assumption that any or all of the spherical wave modes can be excited regardless of antenna size. Physically, this is not possible as demonstrated by Stratton. Stratton [2] is credited by Chu as being the first to demonstrate that the source distribution needed to realize superdirectivity diverges as the directivity of the system increases indefinitely. Therefore, it is physically impossible to excite all of the modes with a finite size antenna. However, Stratton's demonstration on the impracticality of superdirectivity did not completely resolve the issue because there wasn't a basis for limiting the number of modes and, therefore, no physical limit for the directivity. It was Chu who introduced the concept of the quality factor Q to demonstrate how the number of excited modes depended upon the

antenna size. The following section describes how Chu used the Q to define a cutoff for each spherical mode. In doing so, he provided a physical basis for limiting the number of modes used in determining the maximum directivity of a given antenna size. It is remarked that Taylor simultaneously and independently achieved a similar result [14].

2.3 Antenna Quality Factor

The quality factor is a fundamental concept in physics for characterizing an oscillating system. In general, the quality factor Q of an oscillating system is defined to be the total energy content of the oscillator at a given time divided by the energy loss per radian [15]:

$$Q \equiv \frac{W}{dW/d\phi}. \tag{2.3}$$

In electromagnetics, this is commonly stated differently by considering the rate of change of energy per unit time instead of per cycle. Therefore, the denominator in equation 2.3 is replaced using the relation $dW/d\phi = (dW/dt)\,(dt/d\phi) = (dW/dt)\,/\omega$ which leads to the following definition

$$Q \equiv \frac{\omega W}{dW/dt}. \tag{2.4}$$

For an antenna, the energy lost per cycle is caused by radiation and dissipation whereas W is the average stored energy. This means that the Q tells us how the energy of the oscillating system dies out, $dW/dt = -(\omega/Q)\,W$ [15]. That is, from equation 2.4 and assuming an oscillating system having initial energy W_0 at time $t = 0$, the total energy content of the system at any time t is given by $W = W_0 e^{-\omega t/Q}$ [15]. Therefore, the smaller the Q the more quickly the energy of the oscillation dissipates.

This means that an antenna with a low Q is a very effective radiator. Therefore, the Q is of significant physical importance for any oscillating system especially one that is radiating.

The first prominent publication on antenna Q and its use in describing the fundamental limitations of small antennas was by H. A. Wheeler in 1947 [16]. In his paper, he approximated a small antenna as either a lumped capacitor or a lumped inductor connected to a resistor representing the radiation resistance. Using this simple theory, Wheeler was able to show that the ratio between the antenna reactance and resistance (energy stored and energy radiated/dissipated), which he refers to as the power factor, had a lower bound determined only by the antenna's electrical size. However, Wheeler's circuit approximation for an electrically small antenna was only accurate for extremely small antennas.

A year later, a more comprehensive analysis was carried out by Chu [2]. In [2], Chu enclosed the entire antenna structure, its transmission line and oscillator inside the radian sphere. The field outside the sphere produced by the current or source distribution of the antenna was expressed using a complete set of orthogonal spherical modes (both TE and TM) which propagated radially outward. In this approach, space is treated as a waveguide but, unlike traditional waveguide modes, these modes do not have a cutoff frequency or wavelength. Instead, the modes have a "cut-off radius". That is, the size of the radian sphere and the current distribution of the antenna determines which modes can be excited and how effectively they can be excited. To demonstrate this, Chu assumed that the antenna produced the most favorable conditions for energy storage and power dissipation inside the sphere. Specifically, the antenna structure was assumed loss-less and did not store any energy inside the

sphere. Therefore, the antenna has a purely real input impedance at the frequency of interest. These conditions or constraints are important because now the entire energy in the system is in the field external to the sphere. This allows the problem to be analyzed without having to determine the actual "ideal" antenna current distribution and its impedance [2].

In order to determine the system Q, Chu had to separate the energy radiated (propagating) by the antenna from the energy associated with the near field (non-propagating). Since the total energy in the system is infinite [1] and the near-field components are nonlinear, this is not a trivial matter. Chu did this by transforming or reducing the field problem into an equivalent circuit problem by replacing the space outside the sphere with a number of independent equivalent circuits. Each equivalent circuit represented an orthogonal spherical wave mode used in describing the external field. The equivalent circuits were obtained from the wave impedance of each mode which completely describes the propagating and non-propagating energy associated with each mode. The wave impedances for outward traveling waves are given by

$$Z_{+r}^{TM} = \frac{E_\theta^+}{H_\phi^+} = -\frac{E_\phi^+}{H_\theta^+} = j\eta \frac{\hat{H}_n^{(2)}(kr)'}{\hat{H}_n^{(2)}(kr)}. \tag{2.5}$$

for TM modes and by

$$Z_{+r}^{TE} = \frac{E_\theta^+}{H_\phi^+} = -\frac{E_\phi^+}{H_\theta^+} = -j\eta \frac{\hat{H}_n^{(2)}(kr)}{\hat{H}_n^{(2)}(kr)'}. \tag{2.6}$$

[1] Why is the total energy in the system infinite? First of all, the system is being analyzed in steady state and the system is being driven by a continuous wave source (generator). Secondly, the problem domain extends from the surface of the sphere to infinity. Because the domain is infinite in extent, it takes an infinite amount of time to reach steady state (it takes an infinite amount of time for the initial radiated wave to reach infinity). During this time, the generator has been continuously "pumping" energy into the system. Consequently, the total energy in the system is infinite.

for TE modes where the function $\hat{H}_n(kr)$ is given in terms of the spherical Hankel function as

$$\hat{H}_n(kr) = kr\ h_n(kr)\,. \tag{2.7}$$

Using the recurrence formulas for spherical Bessel functions, Chu obtained a partial fraction expansion of the wave impedance for each mode. The resulting expansion was then interpreted as a high-pass RLC ladder network as shown in Fig. 2.1. The network consists of a cascade of series capacitances and shunt inductances with the resistive element at the end of the network used to represent the radiated or propagating energy. Now, the Q could be calculated using the equivalent circuit for each mode by

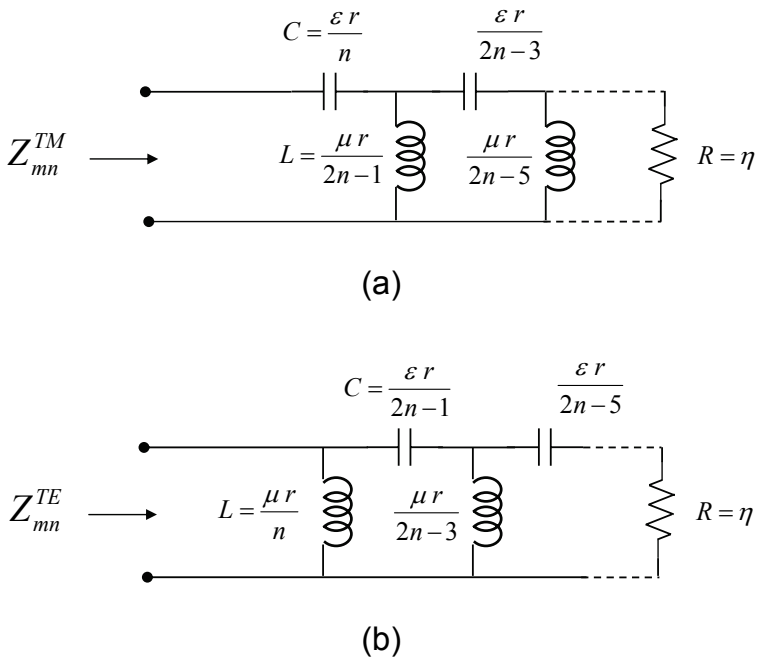

Figure 2.1: Equivalent circuits for the (a) TM_{mn} and (b) TE_{mn} modes of free space [2, 3].

summing the energy stored in each of the inductors and capacitors. Chu then defined a quality factor Q_n for each mode of order n as follows

$$Q_n = \begin{cases} \frac{2\omega \bar{W}_e}{\bar{P}} & \bar{W}_e > \bar{W}_m \\ \frac{2\omega \bar{W}_m}{\bar{P}} & \bar{W}_m > \bar{W}_e \end{cases} \tag{2.8}$$

where $\bar{W}_e$ and $\bar{W}_m$ are the average stored electric and magnetic energy in the inductors and capacitors, and $\bar{P}$ is the radiated energy (dissipated in the resistor). Chu then obtained a general expression for the Q by summing up the mean electric energy stored in all of the circuits and the total power radiated. The Q for this idealized antenna is given by

$$Q = \frac{\sum' A_n^2 \frac{n(n+1)}{2n+1} Q_n}{\sum' A_n^2 \frac{n(n+1)}{2n+1}} \tag{2.9}$$

where A_n is a spherical wave mode coefficient for mode n and Q_n is the Q of the mode. Considering each mode separately, Chu then showed that for a fixed a, the wave impedances for a given mode n are associated with low Q when $ka > n$ and with high Q when $ka < n$. This demonstrated the gradual cutoff phenomenon that occurs around $ka = n$. Note that equation 2.9 is in general not valid. It is only valid for the excitation of either TM_{mn} or TE_{mn} modes because in Chu's analysis he did not consider the case when both TM and TE modes were present simultaneously.

Another important result of Chu's work was the discovery of a lower bound on the radiation Q which depends only on the electrical size ka. Chu demonstrated this by considering the combination of $A_n's$ that would minimize equation 2.9. To find the required $A_n's$, equation 2.9 was differentiated with respect to A_n giving

$$Q_n \sum A_n^2 \frac{n\,(n+1)}{2n+1} = \sum A_n^2 \frac{n\,(n+1)}{2n+1} Q_n \tag{2.10}$$

The above equation can only be satisfied if there is one term in the summation because, for any given ka, the $Q_n's$ have different values [2]. Since the $n = 1$ mode

has the lowest Q, an antenna which excites only the $n = 1$ modes (TM_{m1} and/or TE_{m1}) and stores no energy inside the sphere it occupies has the lowest possible radiation Q. However, Chu's analysis only considered the presence of either TM or TE modes (omni-directional antenna) and, therefore, was not complete. Using the same methodology as Chu, Harrington considered the case when both TE and TM modes are present. In doing so, Harrington showed that the absolute lowest achievable radiation Q was obtained by the equal excitation of the TM_{01} and TE_{01} modes[2] [17]. However, in the method used by Chu and Harrington to calculate the radiation Q, an approximation was made to help facilitate the computation since they lacked the computational power of computers at the time. The approximation made by Chu and repeated by Harrington was to approximate the equivalent circuit for each mode using a second-order series RLC circuit that essentially had the same frequency behavior in the neighborhood of the operating frequency [2,18]. This approximation resulted in a significant error in the calculation of the minimum radiation Q as shown in Fig. 2.2. Later, Collin [19] and Fante [20] both published an exact theory for calculating the radiation Q. The exact equation for the Q derived by Fante is repeated below for completeness (and will be useful later).

$$Q = \text{larger of} \begin{cases} \dfrac{\sum_{n=1}^{\infty}\left[a_n^2 Q_n + b_n^2 Q'_n\right]}{\sum_{n=1}^{\infty}[a_n^2 + b_n^2]} \\ \\ \dfrac{\sum_{n=1}^{\infty}\left[a_n^2 Q'_n + b_n^2 Q_n\right]}{\sum_{n=1}^{\infty}[a_n^2 + b_n^2]} \end{cases} \tag{2.11}$$

where

$$a_n^2 \equiv \sum_{m=0}^{n} \lambda_{nm} \left|A_{nm}\right|^2$$

[2]The combination of the TM_{01} and TE_{01} modes results in the lowest Q because the TM_{01} mode stores predominately electric energy where as the TE_{01} mode stores predominately magnetic energy. Therefore, there is a partial cancellation of the average stored energy when both modes are present.

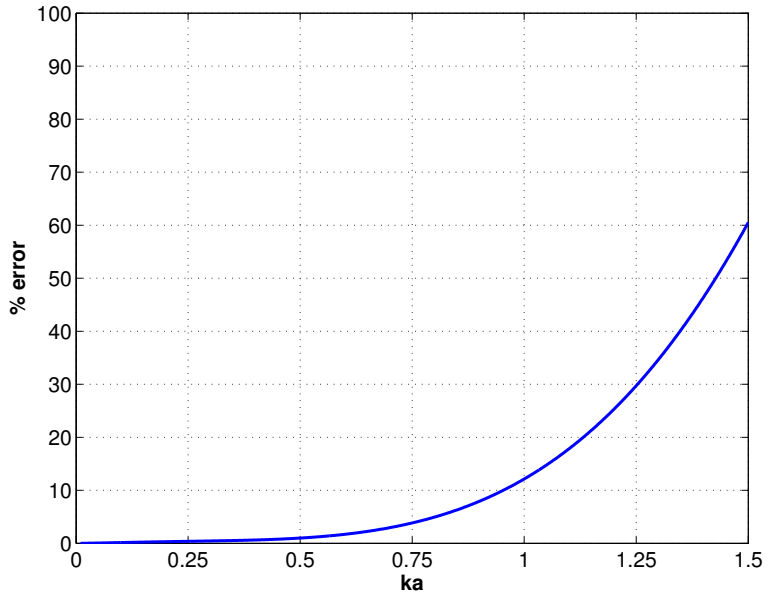

Figure 2.2: Percent error due to calculating the minimum Q based on Chu's approximate analysis and Fante's exact analysis.

$$b_n^2 \equiv \sum_{m=0}^{n} \lambda_{nm} \left| B_{nm} \right|^2$$

$$\begin{aligned} Q_n \equiv\ & ka - \left| h_n(ka) \right|^2 \left[\frac{(ka)^3}{2} + ka(n+1) \right] - \frac{(ka)^3}{2} \left| h_{n+1}(ka) \right|^2 \\ & + (ka)^2 \left(\frac{2n+3}{2} \right) \left[j_n(ka)\, j_{n+1}(ka) + y_n(ka)\, y_{n+1}(ka) \right] \end{aligned}$$

$$Q_n' \equiv ka - \frac{(ka)^3}{2} \left[\left| h_n(ka) \right|^2 - j_{n-1}(ka)\, j_{n+1}(ka) - y_{n-1}(ka)\, y_{n+1}(ka) \right]$$

$$\lambda_{nm} = n(n+1) \frac{2\pi \hat{\epsilon_m}}{2n+1} \frac{(n+m)!}{(n-m)!}$$

with

$$\hat{\epsilon_m} = \begin{cases} 2, & m = 2 \\ 1, & \text{otherwise} \end{cases} \tag{2.12}$$

The work of Chu, Harrington, Collin and Fante was later consolidated into its present form by Hansen [21] and further refined by McLean [18]. The following

equation for the minimum Q is taken from [18] and given by

$$Q_{min} = \frac{1}{N}\left(\frac{1}{(ka)^3} + \frac{N}{ka}\right). \tag{2.13}$$

where k is the free-space propagation constant ($k = 2\pi/\lambda_0$), and a is the radius of the enclosing radian sphere. Note that $N = 1$ refers to the excitation of either the TE_{01} or TM_{01} mode (linearly polarized fields) and $N = 2$ is for equal excitation of both the TE_{01} and TM_{01} modes (field can be either circularly or linearly polarized). Recently, Kwon [22] has shown that if the TE_{01} and TM_{01} modes are not excited equally the minimum Q is given by

$$Q_{min} = \frac{1}{ka} + \frac{1}{(ka)^3\,(1+\alpha^2)}. \tag{2.14}$$

where α is the strength of the TE_{01} mode relative to the TM_{01} mode ($0 \leq \alpha \leq 1$). That is, for equal excitation $\alpha = 1$ and if only one mode is excited $\alpha = 0$. This result is interesting because it implies that the excitation of both TM_{01} and TE_{01} modes, regardless of their relative strength, always results in a lower Q than the excitation of only one of the modes.

2.4 Directivity Limit Based on Antenna Q

In section 2.2, it was evident that there was no mathematical limit to the directivity of an antenna as long as the number of excited spherical modes was unbounded. To provide a means for restricting the number of modes, Chu used the concept of Q to quantify the practicality of exciting a given spherical mode. In doing so, one is faced with the question: How high must the Q be to prevent the mode from being excited? There is not a clear answer to this question because the spherical modes of free space lack a well defined cutoff. In the following, the Q is used to define a limit

for the directivity in different ways. Specifically, in section 2.4.1, the mode cutoff is defined using the mode number and antenna size, resulting in what is called the "normal gain" of an antenna [3, 23]. In section 2.4.2, a more applicable limit is obtained by maximizing the ratio of directivity and Q. Finally, in section 2.4.3, the directivity limit for a minimum Q antenna is discussed.

Before proceeding, it is important to note that none of the directivity limits discussed are truly absolute limits. It is theoretically possible to achieve a higher directivity (super directive antenna) at the expense of higher radiation Q which leads to lower radiation resistance (hence low efficiency) and narrow bandwidth. Therefore, it is likely that such super directive antennas are impractical at best and possibly impossible to realize [21, 24] which is something to be kept in mind.

2.4.1 Chu-Harrington-Taylor Normal Directivity Limit

The first attempt to define a practical limit for the directivity relied on the observation that the Q of spherical modes of order n is considered "high" for $ka < n$. Therefore, it can be assumed that modes of order $n > ka$ are not easily excitable and do not significantly contribute to the field of an antenna of radius a [2, 3]. Under this assumption, the cutoff point is taken to be $ka = n$. Recalling that the maximum directivity that can be achieved using spherical modes of order $n \leq N$ is given by equation 2.2, the "normal directivity" can now be defined as

$$D_{normal} = (ka)^2 + 2ka. \tag{2.15}$$

by substituting $N = ka$ into equation 2.2. It is noted that as ka becomes large, the normal directivity reduces to the directivity obtained by a uniformly illuminated circular aperture of radius a [3, 23]. Additionally, equation 2.15 can be obtained

without using the radiation Q to define a cutoff. Taylor [14] used the magnitude of the field components near the surface of the radian sphere. He argued that for $n > ka$, the field components of mode n would be excessively large and, therefore, could not be used effectively.

Equation 2.15 is often considered as the maximum directivity that can be achieved without incurring a "high" Q [25]. The reason for this is that as ka approaches zero, the normal directivity also approaches zero implying that high Q is unavoidable. Of course, this behavior is really the result of the assumption that modes of order $n > ka$ do not contribute significantly to the antenna field. For $ka < 1$, this is clearly not the case because even an infinitesimal dipole can achieve a directivity of 1.5. Therefore, the normal directivity limit is more useful for electrically large apertures but not electrically small apertures. The following two sections discuss directivity limits that are more applicable to electrically small antennas.

2.4.2 Maximum Directivity for a Given Antenna Q

In deriving the normal directivity and minimum Q, Chu [2] noted that both could not be achieved simultaneously. That is, the spherical mode coefficients required to maximize the directivity where not the same as those minimizing the Q, which implies that there is a fundamental limit to the product or ratio of the directivity and Q. Therefore, Chu proposed to maximize the ratio of the directivity to Q by simultaneously maximizing the directivity while minimizing Q. From [2], this ratio can be interpreted as the condition for a minimum Q antenna to achieve a certain gain or the condition for maximum directivity for an antenna with a given Q. That is, the ratio provides a fundamental link between Q and directivity, and it can be argued that

this is the most important result of Chu's work. In maximizing this ratio, Chu only considered the TM modes making his analysis only applicable to the omni-directional linearly polarized antenna. Fante [25] extended his work to include both TE and TM modes. Later, the work was extended further by Geyi [26] who maximized the ratio of directivity to Q for an omni-directional and directional antenna. Here, the term omni-directional refers to an antenna that radiates into both hemispheres whereas the term directional refers to an antenna that radiates only into one hemisphere. Since Geyi's analysis [26] is the most general, only his results are presented here in.

The ratio D/Q is maximized by an optimization process subject to certain constraints which can be found in [26]. Basically, the optimization process involves adjusting the amplitude and phase of the spherical expansion coefficients in equations 2.1 and 2.11 until the ratio is maximized. For the directional antenna, Geyi showed that the TE and TM modes must be excited equally to maximize the ratio of directivity to Q. The resulting expression is

$$\max \left.\frac{D}{Q}\right|_{dir} = 2\sum_{n=1}^{\infty}\frac{2n+1}{Q_n+Q'_n} \tag{2.16}$$

where Q_n and Q'_n are complicated functions of only ka involving spherical Bessel, Neumann and Hankel functions as defined previously (below equation 2.11). For this maximized D/Q ratio the corresponding minimized Q and maximized directivity are

$$Q_{dir}^{min} = \frac{\sum_{n=1}^{\infty}\frac{2n+1}{Q_n+Q'_n}}{2\sum_{n=1}^{\infty}\frac{2n+1}{(Q_n+Q'_n)^2}} \tag{2.17}$$

$$D_{dir}^{max} = \frac{\left[\sum_{n=1}^{\infty}\frac{2n+1}{Q_n+Q'_n}\right]^2}{\sum_{n=1}^{\infty}\frac{2n+1}{(Q_n+Q'_n)^2}}. \tag{2.18}$$

Similarly, for the omni-directional antenna, the TE and TM modes must also be excited equally to maximize the ratio of directivity to Q. The resulting ratio is given

by

$$\max \left. \frac{D}{Q} \right|_{omni} = 2 \sum_{n=1}^{\infty} \frac{2n+1 \left| P_n^1 (0) \right|^2}{n (n+1) \left[Q_n + Q'_n \right]} \tag{2.19}$$

where $P_n^1 (0)$ is the Legendre polynomial of the first kind. For the omni-directional case, the minimized Q and maximized directivity are

$$Q_{omni}^{min} = \frac{\sum_{n=1}^{\infty} \frac{2n+1 \left| P_n^1(0) \right|^2}{n(n+1)(Q_n+Q'_n)}}{2 \sum_{n=1}^{\infty} \frac{2n+1 |P_n^1(0)|^2}{n(n+1)(Q_n+Q'_n)^2}} \tag{2.20}$$

$$D_{omni}^{max} = \frac{\left[\sum_{n=1}^{\infty} \frac{2n+1 \left| P_n^1(0) \right|^2}{n(n+1)(Q_n+Q'_n)} \right]^2}{\sum_{n=1}^{\infty} \frac{2n+1 |P_n^1(0)|^2}{n(n+1)(Q_n+Q'_n)^2}}. \tag{2.21}$$

The importance of the above results is significant because they define the optimum performance that can be achieved for an antenna of given size. To illustrate this, consider a directional antenna having a Q given by equation 2.17. For this Q, the maximum directivity is given by equation 2.18. If it is desired to have a lower Q, then the ratio D/Q (equation 2.16) requires the maximum achievable directivity to be lower than equation 2.18. Similarly, if it is desired to have a higher directivity than that given by equation 2.18, the minimum Q that can be achieved must be higher than the minimized Q given by equation 2.17. Therefore, equations 2.17 and 2.18 define an optimal performance trade off between directivity and Q that can be achieved for a give antenna size.

Some important observations can be made from equations 2.16-2.21. First, it is useful to compare the minimized Q of equations 2.17 and 2.20 to the lower bound on Q which is provided in Fig. 2.3. From Fig. 2.3 it is apparent that for small ka the difference between the curves is insignificant. To better illustrate the difference between the curves, the percent difference between the Q limit and Geyi's minimized

Q is provided in Fig. 2.4. From this figure, it is evident that the minimized Q for the omni-directional case is nearly identical to the minimum Q limit for $ka < 1$. This implies that for the omni-directional case, a minimum Q antenna achieves optimal performance as defined by the ratio $D/Q|_{omni}$. For the directional case the minimized Q begins to noticeably deviate from the lower bound around $ka = 0.6$. Therefore, a minimum Q directional antenna will only achieve optimum performance when $ka < 0.6$. The reason for this is apparent upon examination of the maximized directivity.

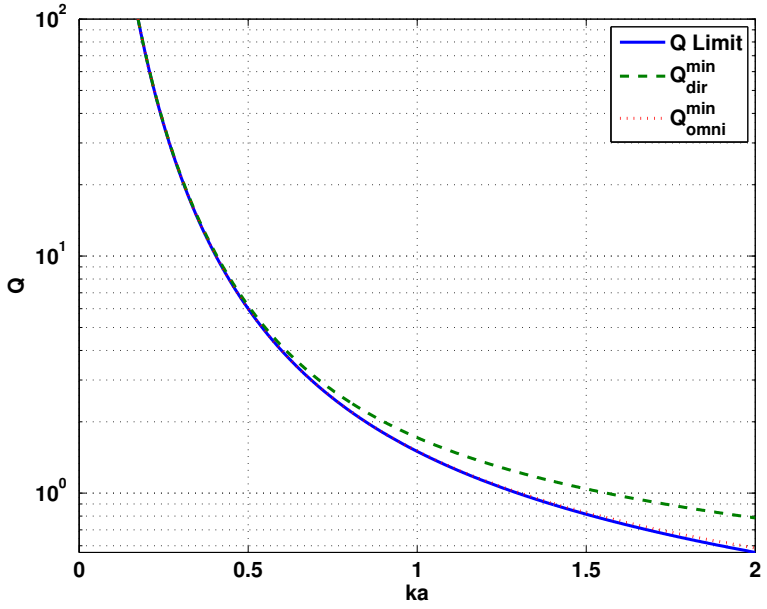

Figure 2.3: Comparison of the antenna Q limit with Geyi's minimized Q for the directional and omni-directional antenna.

A comparison of the maximized directivity and the normal directivity is shown in Fig. 2.5. Note that for the omni-directional case, the maximized directivity approaches 1.5 ($\approx 1.76dB$) as ka approaches zero which agrees with Chu's result [2]. For

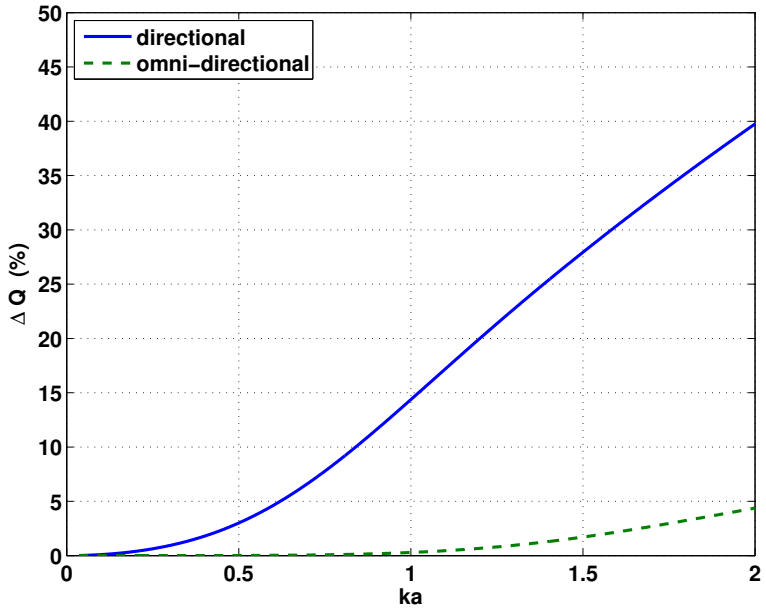

Figure 2.4: Percent difference between the antenna Q limit and Geyi's minimized Q for the directional and omni-directional antenna.

the directional case, the maximized directivity approaches 3 as ka approaches zero, agreeing with Harrington's result [17]. As ka increases, the maximized directivity begins to steadily increase from 3. However, for a directional minimum Q antenna, the maximum possible directivity is 3 (see following section for more details). Therefore, a minimum Q directional antenna cannot achieve optimal performance as defined by equation 2.16 if $ka > 0.5$ because a higher Q is required to achieve the maximized directivity D_{dir}^{max}. This result is interesting because it shows that a minimum Q antenna does not necessarily provide the best performance, as defined by the D/Q ratio for a directional antenna. However, for $ka < 1$, a minimum Q omni-directional antenna does achieve the best performance defined by the D/Q ratio.

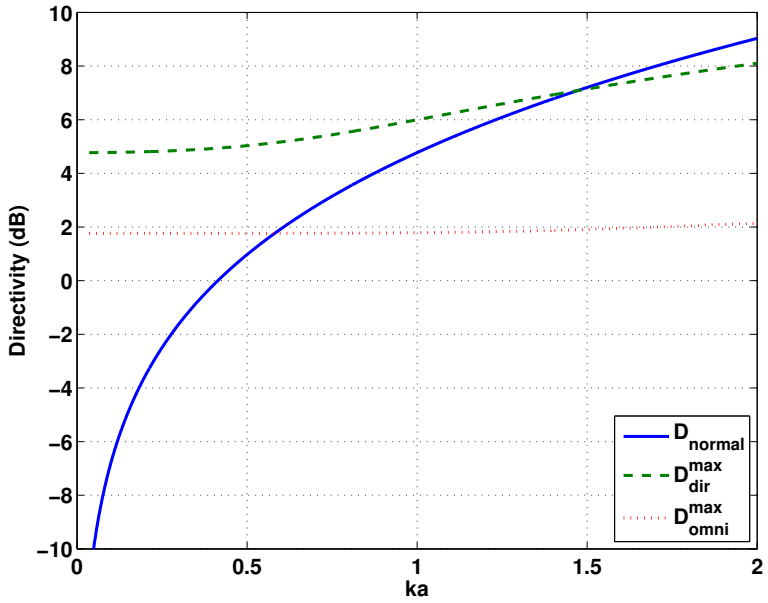

Figure 2.5: Comparison of the normal directivity limit with Geyi's maximized directivity for the directional and omni-directional antenna.

2.4.3 Minimum Q Antenna or Electrically Small

In order to achieve minimum Q only the spherical modes of order $n = 1$ can be excited because the excitation of higher order modes will only increase Q [2]. Since only the $n = 1$ modes are present there is a limit to the directivity than can be achieved. For the most part, this limit can also be applied to electrically small antennas if $ka << 1$. Chu [2] was the first to show that the maximum directivity obtained using either the TM_{01} or TE_{01} mode is 1.5 (omni-directional antenna). Harrington later showed that the maximum directivity for a directional antenna (excitation of both TM_{01} and TE_{01}) is 3 [17, 23]. It is important to note that in [22, 27] it has been stated that an only a linearly polarized antenna can achieve maximum directivity.

However, Pozar has recently shown that this assertion is incorrect [28]. That is, a circularly polarized antenna can achieve maximum directivity.

2.5 Impedance Bandwidth Limitations

In addition to limiting the directivity of an antenna, the Q also impacts the impedance bandwidth of an antenna. To illustrate what limits the impedance bandwidth of an antenna, it is necessary to discuss its impedance behavior as a function of frequency. For an antenna, the impedance rotates clockwise around a Smith chart with increasing frequency [29]. However, over a small range of frequencies it is possible for the rotation to be counter clockwise if there is sufficient loss due to radiation or dissipation. If the loss is constant over a range of frequencies, then from the Hilbert transform it follows that the magnitude and derivative of the reactance is zero. That is, the impedance stops rotating around the Smith chart, as is the case for a spiral antenna when it becomes electrically large ($ka > 1$).

When the load impedance behaves in this manner (purely real), matching it to a resistive generator is trivial and a broadband match can easily be obtained using a matching network with a purely real impedance. However, as the antenna becomes electrically small or as one moves away from a resonance the real part of the antenna impedance becomes smaller and the imaginary part begins to dominate (high Q region). In this case, it is difficult to obtain a broadband match to the resistive generator because of the large reactance. To obtain a broadband match, the reactance of the matching network $X_M(\omega)$ needs to compensate the imaginary part of the load impedance $Z_L(\omega)$. Ideally, it is desired to have $X_M(\omega) = Im\{Z_L^*(\omega)\}$ where

the $*$ denotes complex conjugation. However, such an $X_M(\omega)$ would rotate counter-clockwise around the Smith chart (X_M is a decreasing function of frequency). This of course, leads to the question: Is it possible to realize such a reactance?

To answer this question, let us first consider a typical one port passive loss-less network. Here, passive is taken to mean that the energy absorbed by the network must never be negative [30]. In addition to being passive, the matching network is also a linear and time invariant (LTI). making it a causal system [31]. For such a system, the average stored energy is given by

$$W_{AV} = \frac{1}{2}\frac{dX}{d\omega}|i|^2, \qquad \text{or} \qquad W_{AV} = \frac{1}{2}\frac{dB}{d\omega}|v|^2 \tag{2.22}$$

where B is the susceptance, X is the reactance whereas i and v refer to the current and voltage at the network terminals [30,32]. From equation 2.22, it is apparent that the average stored energy is proportional to the frequency derivative of the reactance (or susceptance). For the energy stored in the network to be positive, the frequency derivative of the reactance must also be positive. This relation is a direct result of Foster's reactance theorem which states that the reactance (or susceptance) of a loss-less passive network is an increasing function of frequency [33]. Note that Fosters Theorem is a direct consequence of causality for a reactive system as proved in [32]. Therefore, it is not possible to realize the ideal X_L with the typical loss-less passive matching network because it is a decreasing function of frequency. In fact, the bandwidth of a loss-less passive matching network is limited by its ability to approximate the ideal X_L behavior over a given frequency range. Below, the bandwidth limitations of passive networks which have a band-pass response are discussed. Section 2.5.2 then discusses two approaches that can be used to realize a reactance that is a decreasing

function of frequency. The two approaches include the active matching network and, the less practical, lossy matching network.

2.5.1 Passive Lossless Networks

The classic problem of designing a passive reactive network to match an arbitrary load to a resistive generator was initiated by Bode [34]. In Bode's analysis, he considered a two element RC or RL load and determined the maximum possible bandwidth for a given maximum tolerable reflection coefficient within the pass-band as illustrated in Fig. 2.6. It is important to note that Bode only considered the case where the matching network had an infinite number of stages. Later, Fano[3] generalized Bode's work by extending it to include arbitrary loads and an arbitrary number of stages [35]. In both Bode's and Fano's work, the response of the system is arbitrary. However, in the literature (especially in antenna theory) their work is presented for the band-pass response [36, 37]. Therefore, it is convenient to use the band-pass response to illustrate the Bode-Fano matching limit for passive lossless networks. In addition, it is also convenient to demonstrate the Bode-Fano matching limit for an RLC load because it can be used to accurately model the impedance of an electrically small antenna below its first resonance.

To begin, the fractional bandwidth for the band-pass response is defined as follows

$$B_n = \frac{\omega_{p2} - \omega_{p1}}{\sqrt{\omega_{p2}\omega_{p1}}} \tag{2.23}$$

where ω_{p2} and ω_{p1} are the high and low edge-band frequencies for which $|\Gamma| \leq |\Gamma_0|$ (see Fig. 2.6). Additionally, the center frequency of the band-pass response is defined to be

[3]Fano also showed how to synthesize Tschebyscheff (equal-ripple) matching networks for certain types of RLC loads.

$\sqrt{\omega_{p2}\omega_{p1}}$. Applying Fano's theory to an RLC load [24, 36, 38], a relation between the Q of the load (antenna), fractional bandwidth B_n and maximum tolerable reflection coefficient Γ is obtained and is given by the following set of equations:

$$QB_n = \frac{2sin\left(\frac{\pi}{2n}\right)}{sinh\,(a) - sinh\,(b)}, \tag{2.24}$$

$$\frac{tanh\,(na)}{cosh\,(a)} = \frac{tanh\,(nb)}{cosh\,(b)}, \tag{2.25}$$

$$\Gamma = \frac{cosh\,(nb)}{cosh\,(na)} \tag{2.26}$$

where n is the number of stages (tuned circuits) and the coefficients a and b are to be determined. It is important to note that $n = 1$ corresponds to the antenna or load alone.

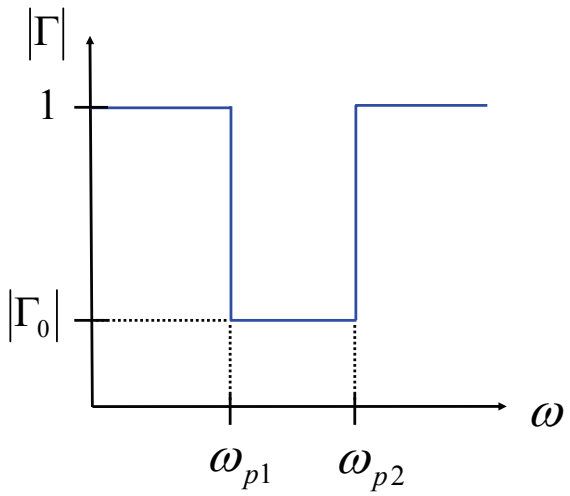

Figure 2.6: A possible band pass response for the reflection coefficient that illustrates Bode-Fano criterion.

Matthaei, Young and Jones were the first to publish solutions to Fano's equations in the form of tables for the coefficients a and b [38]. Their coefficients were dependent upon the choice of $|\Gamma_{max}|$. Later, Lopez [1, 36], using a methodology developed by Wheeler [39], provided a closed form solution in which his coefficients were not a function of $|\Gamma_{max}|$. The obtained expression is given by

$$QB_n = \frac{1}{b_n \sinh\left(\frac{-\ln(\Gamma)}{a_n}\right) - \frac{1-b_n}{a_n}\ln(\Gamma)} \tag{2.27}$$

with the (a_n, b_n) coefficients provided in table 2.1.

Number of Tuned Circuits (n)	a_n	b_n
1	1	1
2	2	1
3	2.413	0.678
4	2.628	0.474
5	2.755	0.347
6	2.838	0.264
7	2.896	0.209
8	2.937	0.160
∞	π	0

Table 2.1: Lopez's coefficients a_n and b_n [1].

From Lopez's solution, it is apparent that the fractional bandwidth is a function of Q, the complexity of the matching network (number of stages) and the maximum tolerable pass-band reflection coefficient. Since the fractional bandwidth is inversely proportional to the Q regardless of the number of matching stages, it increases with

decreasing Q. The fractional bandwidth also increases as the number of matching network stages (complexity) increases. In fact, for any given Q and Γ, maximum bandwidth is obtained by using an infinite number of stages. This is because an infinite number of stages is required to realize the ideal rectangular passband response (see Fig. 2.6). The rectangular passband response is ideal because all of the energy is contained inside the passband (no energy is wasted outside the passband) or, to put it another way, it maximizes the matching area [40]. However, the bandwidth improvement diminishes as the number of stages increase. As noted by Lopez [1], the diminishing return becomes noticeable when the number of tuning circuits is greater than two ($n = 3$ case). This can be demonstrated by considering the percent bandwidth improvement ($[(B_m/B_n) - 1] * 100, m > n$) obtained by increasing the number of stages for a given Q. A comparison of the bandwidth improvement is provided in Fig. 2.7 for the $n = 1, 2, 3$ and ∞ cases. From this figure, the increase in bandwidth obtained by using an additional stage ($m = 2, n = 1$) is significant. For instance, the -10 return loss bandwidth ($\Gamma \approx 0.3162$) increased by about 135%. However, including another stage ($m = 3, n = 2$) only improves the -10 return loss bandwidth by about 24%. Furthermore, using an infinite number of stages ($m = \infty, n = 3$) will only lead to a 33% improvement compared to the three stage case. Whether or not the improvement in bandwidth obtained by using more stages outweighs the additional complexitity of the matching network is a decision left to the designer.

The results presented so far are for edge-band type matching as opposed to the more traditional mid-band matching. Mid-band matching refers to tuning the matching network reactance to achieve a perfect or near perfect match at the center frequency (mid-band). This is the approach commonly illustrated in electromagnetic

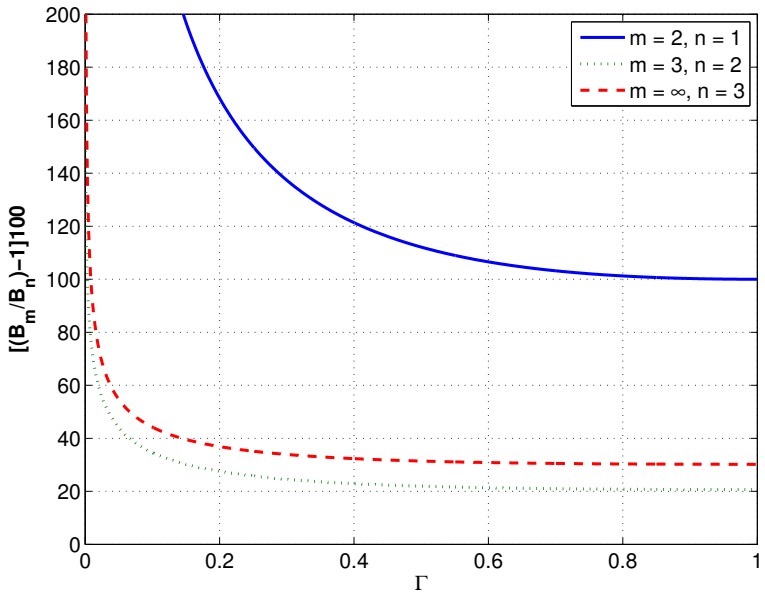

Figure 2.7: Percent bandwidth improvement for a given Q as a function of Γ.

textbooks for the single and double stub matching problems [41]. Edge-band matching sacrifices a perfect or near perfect match at mid-band by introducing some mismatch in order to achieve an overall larger bandwidth. Wheeler [39] demonstrated this for the $n = 1$ case by using simple geometrical arguments to obtain the QB_1 limit for each case. For mid-band matching, the QB limit is given by

$$QB_1 = \frac{1}{\sinh\left(-\ln\left(\Gamma\right)\right)} = \frac{2\Gamma}{1-\Gamma^2} \tag{2.28}$$

whereas for edge-band matching it is given by

$$QB_1 = \frac{2\Gamma}{\sqrt{1-\Gamma^2}}. \tag{2.29}$$

By simply taking the ratio of equations 2.28 and 2.29 it is easily demonstrated that edge-band case has a greater bandwidth. Wheeler also states, but does not prove, that the bandwidth improvement increases with increasing number of stages [39]. It

is remarked that Wheeler's result for the $n = 1$ edge-band case is in exact agreement with Fano [36]. In fact, according to Lopez [36], Wheeler derived the QB_n limit for the $n = 1$ and $n = 2$ cases in the early 1940's before Fano completed his Ph.D. thesis in 1947. While Fano's approach was more comprehensive and mathematically rigorous, one could argue that Wheeler's approach was more elegant because of its simplicity. Regardless, both made significant contributions to the field of impedance matching.

It is important to note that in the theoretical limitations of passive lossless matching networks presented here the frequency behavior of the load impedance is not explicitly included. Instead, it is implicitly included through the use of Q. Therefore, equation 2.27 can be somewhat misleading if one does not take into account that it only applies for an RLC load. That is, over the frequency range of interest, the antenna impedance must behave like an RLC circuit otherwise, the Q cannot be used in equation 2.27 to determine the fractional bandwidth.

2.5.2 Active and Lossy Networks: Non-Foster Matching

Active devices such as transistors, diodes and op-amps can be used to overcome the bandwidth limitations of passive lossless networks. This is because Foster's reactance theorem does not apply to networks that include active devices. Therefore, it is possible to create negative resistance, inductance and capacitance using active devices. This is accomplished by using positive feedback which inherently has stability issues. Circuits which exhibit this type of behavior are usually referred to as negative impedance converters (NIC). To my knowledge, a theoretical limit for the maximum possible bandwidth given a maximum tolerable reflection coefficient does not exist for

active matching networks. Therefore, the use of non-Foster matching circuits may be promising and worth further investigation. For more information on this topic, the reader is referred to [24] which contains a historical review of the work in this area.

Another way to overcome the bandwidth limitations of passive lossless networks is to make the network lossy. With sufficient loss it is possible to make the impedance of a network rotate counterclockwise around a Smith chart. Apparently, this approach has been considered in the past [42,43]. However, this approach is highly impractical because the resulting matching network would have a very low efficiency. For electrically small antennas, which naturally have low efficiency due to their low radiation resistance, using a matching network with a low efficiency is extremely impractical.

2.6 Extending Fundamental Limitations to Broadband Antennas

In the previous sections, the limitations on the directivity and impedance bandwidth as a function of Q were discussed. The relation between the directivity and Q was established in section 2.4.2 and applies in general to any type of antenna. However, the relation between Q and impedance bandwidth established in section 2.5.1 is only applicable for a band-pass response and RLC load. Therefore, it is only useful for narrow band antennas such as a dipole below resonance. For antennas that naturally have a continuous high-pass response, such as a spiral or any other frequency independent antenna, the result in section 2.5.1 is not applicable. That is, for a spiral antenna or any frequency independent antenna, there is only a lower limit f_{low} to its frequency response because of its finite size. An upper limit does not exist because turns can always be added to the center of the spiral to increase the upper

frequency limit f_{high}[4]. Therefore, the lowest operational or cut-off frequency is of utmost importance for a high-pass response.

To my knowledge, there is no previous work defining a limit for the cutoff frequency of a broadband electrically small antenna. In this section, Fano's work is adapted to the high-pass matching case, making it applicable to broadband antennas. By doing so, a limit is obtained for the case when the antenna is connected directly to the generator and for an infinite stage matching network. The resulting limit is a relationship between the cutoff frequency (cut-off size) and the maximum tolerable pass-band reflection coefficient.

2.6.1 Fano-Bode Limit for High-Pass Response

In this section, the broadband impedance matching theory of Fano [4,35] is applied to broadband antennas which have a high-pass response. The purpose is to define a theoretical limit for the cutoff frequency (cutoff size) subject to an in-band reflection coefficient. It is also of particular interest to consider the cutoff frequency when the broadband antenna is electrically small. For the derived result to be a limit, the load must represent an the ideal or optimum radiator (minimum Q antenna). Additionally, if this limit is to be valid for all broadband antennas, the load must be able to characterize the energy radiated and stored by any broadband antenna when it is electrically small. The constraint of optimum performance can be satisfied by using the equivalent circuit(s) for the TM_{01} and/or TE_{01} modes that have the lowest possible radiation Q. However, these equivalent circuits are only second order RLC

[4]Taking into account practical limitations such as fabrication tolerances, there is a practical upper frequency limit.

circuits which may or may not adequately describe a broadband antenna in general. Therefore, it is necessary to justify their use in characterizing a broadband antenna.

First of all, a second order RLC circuit has a high pass response just like a broadband antenna. However, this is relatively unimportant because the goal is to describe the broadband antenna's behavior at the lower band edge where it is electrically small and not its entire frequency response. To do this, the load must be able to represent the sub-resonance behavior of the first "resonance" of a broadband antenna. This is something that a second order RLC circuit is perfectly capable of modeling for any type of antenna. That is to say, as any antenna becomes electrically small, its radiation resistance begins to decrease and the time averaged stored energy becomes predominately inductive or capacitive depending upon the type of antenna. As this behavior is characteristic of any second order RLC circuit below the first resonance, the second order RLC circuit is suited for this analysis. However, if one is familiar with the input impedance behavior of electrically small broadband antennas, they might find it objectionable to using a second order circuit because the input impedance looks like open or short circuited transmission line (see Fig. 2.8). However, the impedance seen from the input terminals of a broadband antenna is not indicative of its true behavior. To illustrate this, it is necessary to discuss the concept of modeling the antenna impedance using a terminated transmission line.

The input impedance of any antenna can be modeled as a uniform section of transmission line terminated by a frequency dependent impedance Z_t [44]. Such a model is especially useful in describing the input impedance for broadband antennas [45]. In this model, the characteristic impedance of the transmission line is equal to the characteristic impedance of the antenna structure when it is infinite in extent. For

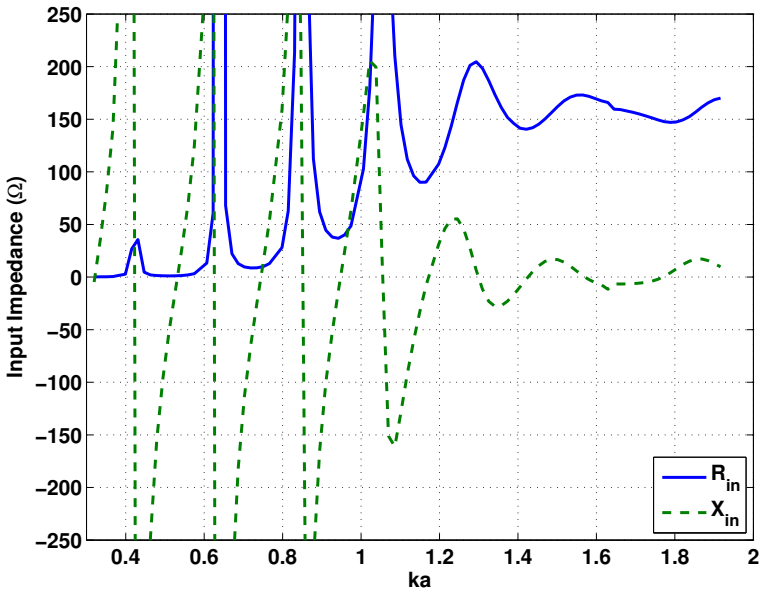

Figure 2.8: Typical spiral antenna input impedance.

some antenna structures, such as the spiral, this characteristic impedance is frequency independent. For other antennas, such as thin wire antennas, it will be a function of frequency [44]. For any antenna, the length of the transmission line is proportional to the length of conductor that forms the antenna. For example, the transmission line length could be equal to one half the total length of a bowtie antenna or the arm length for a spiral antenna. Therefore, in this model the terminating impedance represents the "end effect" caused by the truncation of the antenna structure. That is, as the wave emerges from the generator and is guided along the antenna, it will eventually reach the end of the antenna structure. Upon reaching the end, some of the energy is transfered to the region beyond the antenna (radiated) and some of it is reflected back resulting in stored energy. So, the terminating impedance represents the impedance of free space seen by the wave from the ends of the antenna.

Consequently, the real part of Z_t represents the radiation resistance and the imaginary part is related to the time averaged stored energy. Since Z_t directly represents the energy radiated and stored by the antenna in this model, its behavior when the antenna is electrically small can be described using a second order RLC circuit for reasons mentioned previously. Now the question is: The only remaining issue relates to whether the presence of the transmission line prevents Z_t from being used as the load impedance in Fano's matching theory. In this regard, it is important to note that Fano's matching theory is only dependent upon the zeros and poles of the *magnitude* of the reflection coefficient [4]. Therefore, if the transmission line does not affect the magnitude of the reflection coefficient then Z_t can be used as the load impedance. To demonstrate the impact of the transmission line, let Γ_t be the reflection coefficient, with respect to the characteristic impedance of the transmission line, looking into the load impedance Z_t. In addition, let Γ_{in} be the reflection coefficient, with respect to the characteristic impedance of the transmission line, looking into the transmission line at a distance l from the load Z_t. The magnitudes of Γ_t and Γ_{in} are equal because moving the observation point a distance l from Z_t only effects the phase of the reflection. Therefore, the presence of the transmission line is irrelevant in regards to the magnitude of the reflection coefficient[5] which justifies the use of a second order RLC circuit to characterize an electrically small broadband antenna.

Now that the load impedance has been chosen, the next step is to apply Fano's theory for the high-pass matching case. Once again, the goal is to determine the cutoff frequency ω_c for which the magnitude of the reflection coefficient is less than or equal to a specified $|\Gamma_0|$ for all frequencies greater than ω_c. In what follows, two

[5]The presence of the transmission line is not irrelevant in regards to the impedance.

cases are considered for the matching network: 1) The matching network has an infinite number of stages ($n = \infty$); 2) The load is connected directly to the resistive generator ($n = 1$). Since an infinite stage matching network only exists in theory, this case defines an absolute limit for high-pass matching. On the other hand, case 2 provides a limit that is more practical and useful. Note that it is not necessary or advised to use Fano's analysis for the simplistic case 2. In the discussion that follows, Fano's solution for the low-pass case is adapted for the high-pass case using an RLC load. It is beyond the scope of this discussion to comment on the mathematics of Fano's solution. Instead, the discussion attempts to provide a physical interpretation of the equations and Fano's method in general.

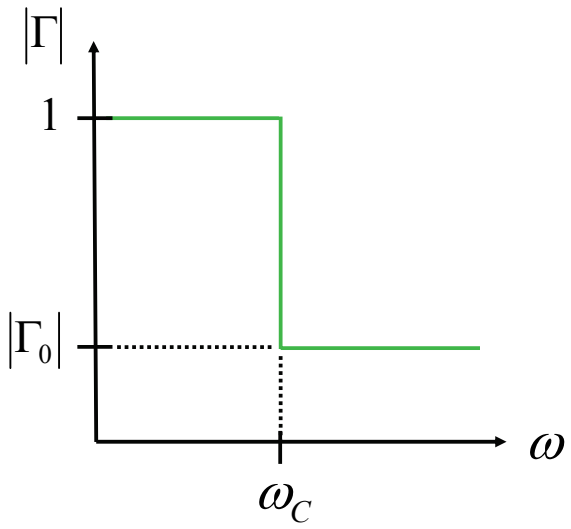

Figure 2.9: The ideal high-pass reflection coefficient response.

Consider the problem of designing an optimum lossless passive network to match an arbitrary load impedance to a resistive generator as illustrated in Fig. 2.10. Fano

solved this problem in general and developed a method for synthesizing the matching network [35]. The basic idea of Fano's approach was to tolerate a certain amount of mismatch between the load and generator such that the bandwidth (or matching area) is maximized. The characteristics of the load impedance and the complexity of the matching network determine the theoretical limitations on the tolerance of match and bandwidth. That is, the frequency response of the reflection coefficient

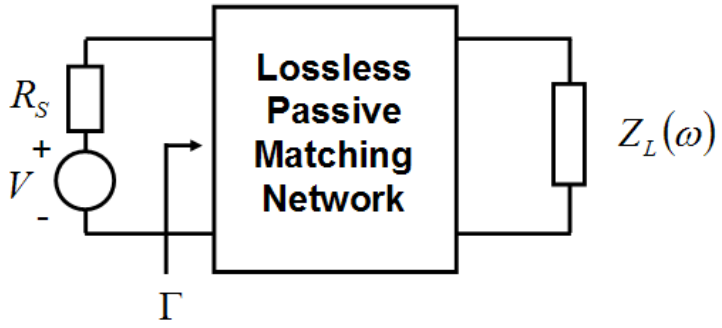

Figure 2.10: Matching network for an arbitrary load impedance [4].

for the matching network terminated with a given load impedance is limited by some conditions of physical realizability[6]. Therefore, the solution to the arbitrary matching problem must satisfy these conditions. To determine the conditions of physical realizability, Fano simplified the problem by replacing the load impedance by its Darlington equivalent[7] as shown in Fig. 2.11 and normalized the impedance making the

[6]The term "conditions of physical realizability" refers to physical conditions which force the response functions to be analytic in certain regions of the complex plane. These physical conditions can involve linearity, time invariance, causality, passivity, conservation of energy, etc..

[7]Any physically realizable impedance function can be considered as the input impedance to a reactive two-port network terminated in a pure resistance which is otherwise known as a Darlington equivalent circuit

resistances equal to unity. The resulting network consists of two reactive networks connected in cascade to form a single two-port reactive network N terminated at each port with a 1Ω resistor. By transforming the problem in this manner, the problem has

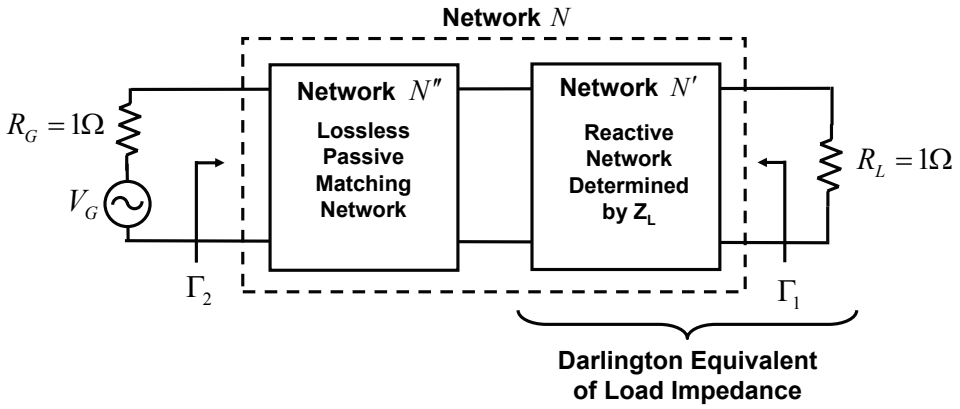

Figure 2.11: Matching network and Darlington equivalent of load impedance in cascade [4].

been simplified to finding the conditions of physical realizability for a purely reactive network N instead of the original arbitrary network [35]. The two port reactive network is defined in general as shown in Fig. 2.12. In general, the reflection coefficient (and transmission coefficient) can be written as the ratio of two real polynomials in terms of the complex frequency variable $s = \sigma + j\omega$ as follows

$$\Gamma = K\frac{(s - s_{01})(s - s_{02})\cdots(s - s_{0n})}{(s - s_{p1})(s - s_{p2})\cdots(s - s_{pn})} \tag{2.30}$$

where K is a real number. For the network shown in Fig. 2.12, the reflection and transmission coefficients are defined as follows

$$\Gamma_1 = \frac{Z_1 - 1}{Z_1 + 1} = \left[\frac{2V_1}{E_1} - 1\right]_{E_2=0} \tag{2.31}$$

$$\Gamma_2 = \frac{Z_2 - 1}{Z_2 + 1} = \left[\frac{2V_2}{E_2} - 1\right]_{E_1=0} \tag{2.32}$$

$$T^1 = \left[\frac{2V_2}{E_1}\right]_{E_2=0} \tag{2.33}$$

where Z_1 and Z_2 are the impedances measured at the terminals when the voltage sources are short circuited. Since the reactive network is non-dissipative, the reflection and transmission coefficients must satisfy the following relations

$$|\Gamma_1|^2 = |\Gamma_2|^2 = 1 - |T_1|^2 \tag{2.34}$$

and

$$|\Gamma_1| = |\Gamma_2| \leq 1; \qquad |T_1| \leq 1. \tag{2.35}$$

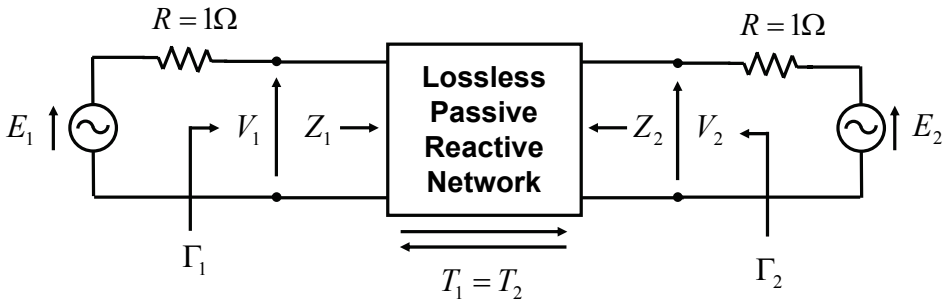

Figure 2.12: Two terminal pair reactive network [4].

For the network N to be physically realizable its transmission coefficient T and reflection coefficient Γ_1 (or Γ_2) must satisfy conditions imposed on it by the load (network N') and the matching network (network N''). For instance, the transmission zeros of network N' must also be transmission zeros of network N [35]. Therefore,

to determine the conditions on network N, Fano expressed Γ_1 and T in terms of the reflection and transmission coefficients of the individual networks N' and N'' (see Fig. 2.13):

$$\Gamma_1 = \Gamma'_1 + \Gamma''_1 \frac{(T')^2}{1 - \Gamma'_2 \Gamma''_1}. \tag{2.36}$$

$$T = \frac{T'T''}{1 - \Gamma'_2 \Gamma''_1}. \tag{2.37}$$

Using equation 2.30 and 2.36, Fano could determine the constraints on the zeros and poles of the overall network N in terms of the known zeros and poles of the individual networks N' and N''. To satisfy all of the constraints imposed by physical realizability, Fano developed a set of integral equations involving the logarithm of the magnitude of the reflection coefficient. For a high-pass response the equations involve an integral of the form

$$\int_0^\infty \omega^{-2(k+1)} ln\left(\frac{1}{|\Gamma_1|}\right) d\omega \tag{2.38}$$

for $k = 0, 1, ..., N-1$, where N is the multiplicity of the transmission zeros of $|\Gamma|$ (the number of transmission zeros associated with the load). Each integral is over the frequency spectrum of the return loss function $ln\left(1/|\Gamma|\right)$ multiplied by a weighting function $\omega^{-2(k+1)}$. Note that the function $ln\left(1/|\Gamma|\right)$ is used instead of $|\Gamma|$ for purely mathematical reasons. The integral is evaluated in the complex frequency domain ($s = \sigma + j\omega$) over the imaginary axis (real frequency) using a contour integral over the entire right-half plane. Fano performed the contour integration using Cauchy's integral formula which results in integral relations of the form

$$\int_0^\infty \omega^{-2(k+1)} ln\left(\frac{1}{|\Gamma_1|}\right) d\omega = (-1)^k \frac{\pi}{2} \left[A^0_{2k+1} - \frac{2}{2k+1} \sum_i s_{ri}^{-(2k+1)}\right] \tag{2.39}$$

The general result of the contour integration is given by the right-hand side of equation 2.39 which involves the zeros and poles of the load and matching network. The A^0_{2k+1} coefficients come from the Taylor series expansion of the return loss function $ln\,(1/\,|\Gamma|)$ and depend only on the load [35]. The A^0_{2k+1} coefficients are given by

$$A^0_{2k+1} = \frac{1}{2k+1}\left(\sum_i s_{oi}^{-(2k+1)} - \sum_i s_{pi}^{-(2k+1)}\right) \tag{2.40}$$

where s_{oi} and s_{pi} are the zeros and poles of the load respectively. The last term on the right hand side of equation 2.39 are the unknown zeros of the matching network that lie in the right half plane[8]. Note that the poles of the matching network are absent from equation 2.39 because Fano eliminated them by mapping them into the left-half plane without changing the magnitude of Γ_1 (the mapping only effects the phase of Γ_1) [4].

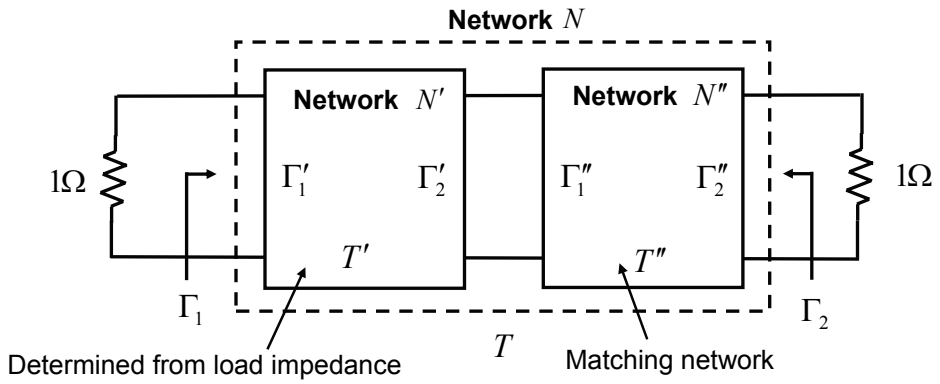

Figure 2.13: Two reactive networks in cascade [4].

[8]The real part of s_{ri} must be positive and, if complex, it must come in complex conjugate pairs [4].

It is interesting to consider the physical meaning of equation 2.39. First of all, it is important to emphasize that for the frequency response of the system to be physically realizable, it must be band limited just like any other transfer function. That is, there is a finite amount of energy that can be distributed across the frequency spectrum to form the pass-band of the frequency response. Essentially, the integral in equation 2.39 enforces this condition which becomes evident upon examining the integrand. The term $ln\left(1/\left|\Gamma\right|\right)$ in the integrand represents the arbitrary frequency response of the system. The purpose of the weighting functions is to confine the response to a certain portion of the frequency spectrum, depending on the type of response being considered. The extent to which the response is confined (its bandwidth) is determined by three conditions: 1) the specified magnitude of the reflection coefficient $|\Gamma_0|$ in the pass-band; 2) the nature or behavior of the load which is described by its zeros and poles (A coefficients); 3) the complexity or number of zeros of the matching network (s_{ri}'s). Since the behavior of the load is known, the integral relations are solved simultaneously by choosing the appropriate zeros of the matching network (s_{ri}'s) that maximize the area given by each integral. The solution takes the form of a n^{th}-order polynomial which relates the bandwidth to $|\Gamma_0|$. The theoretical limitations of matching the given load can then be found by solving the polynomial (only one of the roots is positive real). Therefore, the solution of equation 2.39 can be interpreted as defining a limit for a "matching area" [40] of the network N that is dependent upon the bandwidth and some function of $|\Gamma_0|$. For instance, the matching area of an ideal band-pass response is the product of the fractional bandwidth B and $ln\left(1/\left|\Gamma_0\right|\right)$ (see section 2.5.1). For an RLC load, the band-pass matching area is limited by the Q of the load (π/Q, see equation 2.27).

Now that equation 2.39 has been introduced, its solution for the equivalent circuit of the TM_{01} or TE_{01} mode can commence for the case where the system has the ideal high-pass response shown in Fig. 2.9 (matching network consists of an infinite number of stages). To begin, the equivalent circuits illustrated in Fig. 2.1 are first normalized to the free space impedance η to be consistent with Fano's approach. The impedance seen looking into the circuits is given by

$$Z_{TM_{01}}(\omega) = \frac{1}{Z_{TE_{01}}(\omega)} = \frac{1}{j\omega\frac{a}{c}} + \frac{j\omega\frac{a}{c}}{j\omega\frac{a}{c}+1} \tag{2.41}$$

Rewriting equation 2.41 in terms of the complex frequency $s = j\omega$, equation 2.41 becomes

$$Z_{TM_{01}}(s) = \frac{1}{Z_{TE_{01}}(s)} = \frac{s^2a^2 + sac + c^2}{s^2a^2 + sac}. \tag{2.42}$$

The reflection coefficient normalized with respect to η is then given by

$$\Gamma(s) = \frac{Z-1}{Z+1} = \pm\frac{c^2}{s^2a^2 + sac + c^2} \tag{2.43}$$

where the plus sign refers to the TM_{01} mode and the minus sign to the TE_{01}. Regardless of the mode, equation 2.43 has two poles $s = \frac{-c\pm jc}{2a}$ and no zeros. Therefore, there are two transmission zeros for this load impedance ($N = 2$). Recalling that $k = 0, 1, ..., N-1$, equation 2.39 produces two equations which are

$$\int_0^\infty \omega^{-2} ln\left(\frac{1}{|\Gamma|}\right) d\omega = \frac{\pi}{2}\left[A_1^0 - 2\sum_i s_{ri}^{-1}\right] \tag{2.44}$$

for $k = 0$ and

$$\int_0^\infty \omega^{-4} ln\left(\frac{1}{|\Gamma|}\right) d\omega = \frac{-\pi}{2}\left[A_3^0 - \frac{2}{3}\sum_i s_{ri}^{-3}\right] \tag{2.45}$$

for $k = 1$. The A_{2k+1}^0 coefficients are calculated from the poles of the RLC circuit as follows

$$A_1^0 = -\sum_{i=1}^{2} s_{pi}^{-1} = \frac{2a}{c} \tag{2.46}$$

for $k = 0$ and

$$A_3^0 = -\frac{1}{3}\sum_{i=1}^{2} s_{pi}^{-3} = -\frac{1}{6}\left(\frac{2a}{c}\right)^3 = -\frac{\left(A_1^0\right)^3}{6} \tag{2.47}$$

for $k = 1$. Since the matching network consists of an infinite number of stages, it is possible to realize the ideal high-pass response shown in Fig. 2.9. The ideal high-pass response is given by a rectangular function for which $ln\left(\frac{1}{|\Gamma|}\right) = ln\left(\frac{1}{|\Gamma_0|}\right)$ when $\omega \geq \omega_c$ and $ln\left(\frac{1}{|\Gamma|}\right) = 0$ when $\omega < \omega_c$. Assuming an ideal high-pass response, the integrals on the left hand side of equations 2.44 and 2.45 can be evaluated analytically. The results are given by the following

$$\int_{\omega_c}^{\infty} \omega^{-2} ln\left(\frac{1}{|\Gamma_0|}\right) d\omega = ln\left(\frac{1}{|\Gamma_0|}\right) \int_{\omega_c}^{\infty} \omega^{-2} d\omega = \frac{1}{\omega_c} ln\left(\frac{1}{|\Gamma_0|}\right) d\omega \tag{2.48}$$

$$\int_{\omega_c}^{\infty} \omega^{-4} ln\left(\frac{1}{|\Gamma_0|}\right) d\omega = ln\left(\frac{1}{|\Gamma_0|}\right) \int_{\omega_c}^{\infty} \omega^{-4} d\omega = \frac{1}{3\omega_c^3} ln\left(\frac{1}{|\Gamma_0|}\right) d\omega. \tag{2.49}$$

Substituting equations 2.48 and 2.49 into equations 2.44 and 2.45 respectively, the following system of equations is obtained

$$\frac{1}{\omega_c} ln\left(\frac{1}{|\Gamma_0|}\right) = \frac{\pi}{2}\left[A_1^0 - 2\sum_i \lambda_{ri}^{-1}\right] \tag{2.50}$$

$$\frac{1}{\omega_c^3} ln\left(\frac{1}{|\Gamma_0|}\right) = \frac{-\pi}{2}\left[3A_3^0 - 2\sum_i \lambda_{ri}^{-3}\right] \tag{2.51}$$

As Fano noted, to simultaneously maximize the matching area defined by each integral, the matching network must be selected so that $\sum \lambda_{ri}^{-3}$ is as large as possible while keeping $\sum \lambda_{ri}^{-1}$ as small as possible. This is accomplished by using a single real zero, $\lambda_r = \sigma_r$ [4]. Solving equation 2.50 for σ_r and substituting the result into equation 2.51 eliminates σ_r. The resulting equation is a cubic polynomial which takes the form

$$\omega_c^3 - \omega_c^2 \frac{K}{A_1^0} - \omega_c \frac{K^2}{\left(A_1^0\right)^2} + \frac{K^3 - 4K}{3\left(A_1^0\right)^3} = 0. \tag{2.52}$$

where $K = \frac{2}{\pi} ln\left(\frac{1}{|\Gamma_0|}\right)$. The cubic equation was solved using Matlab to find the roots of ω_c for a given K. It turns out, that for any given K, only one of the roots of ω_c is real. The solution is shown graphically in Fig. 2.14 as the $n = \infty$ case (dashed line). Here, ω_c has been multiplied by a/c to convert it to the more useful parameter ka. The curve in Fig. 2.14 for the $n = \infty$ case should be interpreted as follows: For a given $|\Gamma_0|$, there is a corresponding $k_c a$ which defines the smallest electrical size for which the pass-band reflection coefficient can equal $|\Gamma_0|$. To achieve this cutoff size, the frequency response must be rectangular. That is, below $k_c a$ the magnitude of the reflection coefficient must be one and for all frequencies above $k_c a$ it is exactly equal to $|\Gamma_0|$. Therefore, the curve in its entirety cannot be realized. Only a single point on the curve can be realized using the ideal rectangular high-pass response. Even though such a response can be considered impractical for a variety of reasons, this curve is still useful because it provides an absolute lower limit for the cutoff size or frequency as function of the reflection coefficient.

A more practical and useful case occurs when the load is connected directly to the generator ($n = 1$). In this case the reactive matching network doesn't exist, which allows the problem to be solved easily because the behavior of the reflection coefficient is known. Since the generator is purely resistive, the magnitude of the reflection coefficient is given by

$$|\Gamma| = \left|\frac{Z_L - R_0}{Z_L + R_0}\right|. \tag{2.53}$$

where Z_L is the impedance of the equivalent circuit for the TM_{01} or TE_{01} mode and R_0 is the generator resistance. As in the previous case ($n = \infty$), the resistances are set equal to unity by letting $R_0 = \eta_0$ and then normalizing the load impedance and R_0 by η_0. The relation between $|\Gamma_0|$ and the cutoff frequency (cutoff size) can

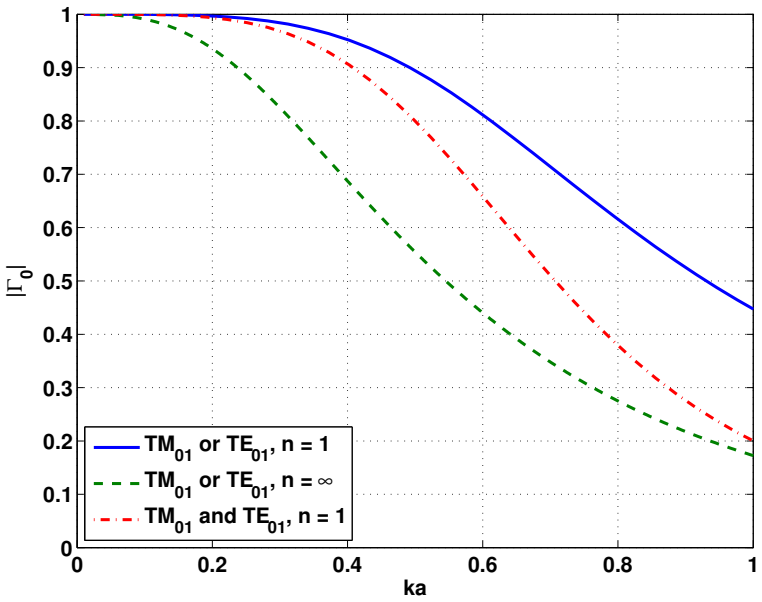

Figure 2.14: In-band reflection coefficient Γ_0 vs the cutoff size ($ka = \frac{\omega_c a}{c}$) or cutoff frequency. The cutoff size is the smallest antenna size for which $|\Gamma| \leq |\Gamma_0|$.

now be found by evaluating equation 2.53. The resulting curve is shown in Fig. 2.14 (solid line). Another useful case to consider is when the TM_{01} and TE_{01} modes are both excited equally and connected to the generator. The equivalent circuit for this case was obtained by combining the circuits in Fig. 2.1 as in [46] (see Figure 5 in [46]). From [46], the equal excitation of both modes results in a series combination of the circuits in Fig. 2.1. Therefore, the resistances are set equal to unity by letting $R_0 = 2\eta_0$ and then normalizing the load impedance and R_0 by $2\eta_0$. The resulting relation between $|\Gamma_0|$ and the cutoff frequency is shown in Fig. 2.14 (dash-dot line).

The results in Fig. 2.14 can be used in conjunction with the directivity limits from section 2.4.3 to define a limit for the realized gain. For the previous case which used the equivalent circuit for only one of the lowest order spherical modes, the

directivity is limited to 1.5 for all ka. Assuming antenna is loss-less, the realized gain is calculated for these two cases using the results from Fig. 2.14 and a directivity of 1.5. The resulting realized gain curves are shown in Fig. 2.15 in addition to a third curve. The third curve is the realized gain limit for the case where both TM_{01} and TE_{01} modes were excited equally. For this case, the maximum directivity that can be achieved is 3.

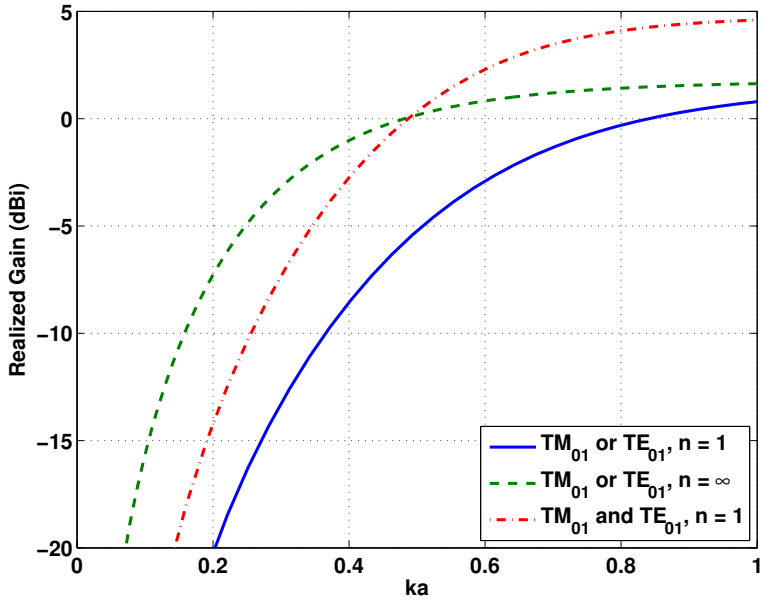

Figure 2.15: The lowest achievable cutoff frequency for a minimum Q antenna in terms of the realized gain.

In closing, some final comments about the curves shown in Fig. 2.14 and 2.15 should be made. First of all, the limits derived in this section are for a *minimum Q antenna* which is matched such that its *response is high-pass*. Therefore, these limits are not applicable if the antenna has a band-pass response. Specifically, by using a

band-pass response, it is possible to achieve a higher realized gain at a given ka than the limit shown in Fig. 2.15 because the fractional bandwidth can always be reduced to achieve a lower reflection coefficient than the high-pass response. This is the advantage of using a band-pass response instead of a high-pass response. Secondly, one should be cautious about the validity of the realized gain limit as ka approaches and exceeds unity. That is, as ka increases, higher order modes ($n \geq 2$) can be excited without significantly increasing the Q. Since the limit presented here only considers the lowest modes ($n = 1$), the limit does not apply in regions where higher order modes can be excited with minimal impact on the Q. Finally, it is reemphasized that the limits in this section are based upon a minimum Q antenna. Therefore, to approach these limits, it is necessary to minimize the antenna Q.

2.7 Summary

In this chapter, the fundamental limits on radiation Q, directivity and impedance matching of electrically small antennas were discussed. Specifically, the relation between directivity and radiation Q was reviewed in section 2.4.2. This often overlooked relation is important because it provides a lower bound on the radiation Q for a given directivity subject to the antenna size. In section 2.5.1, the relation between Q and impedance bandwidth was reviewed for electrically small antennas which have a band-pass response. This relation describes a fundamental relation between electrical size, fractional bandwidth and maximum tolerable reflection coefficient. While this relation is very useful for quantifying the limitations of narrow band antennas, it is unsuitable for electrically small UWB antennas (high-pass response). To quantify the limitations of electrically small UWB antennas, the fundamental limit on the

radiation Q was used in conjunction with the Fano-Bode matching theory in section 2.6 to establish a limit for the cut-off frequency (cut-off electrical size) subject to a maximum tolerable reflection coefficient. This relation was then combined with the directivity limitations to define a limit on the maximum achievable realized gain as a function of electrical size (cut-off size). The next chapter discusses how antenna miniaturization can be used to approach this limit by minimizing the antenna Q. In Chapters 4 and 5, antenna miniaturization techniques are applied to a spiral antenna for exploring methods to approach this limit.

CHAPTER 3

ANTENNA MINIATURIZATION

In the previous chapter, the fundamental limits on radiation Q, directivity and impedance matching of electrically small antennas were discussed. To quantify the performance limitations of electrically small UWB antennas, these fundamental limitations were used to establish a limit for the cut-off frequency (cut-off electrical size) subject to a maximum tolerable reflection coefficient. The purpose of this chapter is to discuss how this theoretical limit can be approached by miniaturizing preexisting antenna designs. The following section discusses the concept of miniaturization using a dipole antenna as an example. This example is used to illustrate the key aspect of miniaturization which is phase velocity reduction. By reducing the phase velocity, the antenna appears to be electrically larger which improves its performance. Section 3.2 discusses the basic concept of reducing the phase velocity using reactive and/or material loading whereas Section 3.3 demonstrates the performance improvement achieved by miniaturizing a dipole antenna. Following this general discussion of miniaturization, the miniaturization of broadband antennas is discussed in Section 3.4, with particular emphasis on the spiral antenna.

3.1 Importance of Electrical Size and Phase Velocity

In this section, a qualitative explanation of how miniaturization can improve the performance of an electrically small antenna is presented. The goal is to develop an intuitive understanding of antenna miniaturization. Fundamentally, antenna miniaturization can be understood by considering two important concepts which are electrical size and phase velocity. Here, electrical size is defined in terms of the free-space (vacuum) wavelength and the phase velocity is associated with the wave guided (not radiated) by the antenna structure.

To illustrate how miniaturization can improve the performance of an electrically small antenna, a dipole antenna is used to demonstrate the affect of electrical size and phase velocity on the radiated field. Instead of using the traditional time harmonic analysis, this example is analyzed from a time-domain perspective to provide a better physical understanding. The following discussion summarizes the time-domain analysis provided in [47] for a dipole antenna. Using the result of this analysis, the effect of electrical size and phase velocity can be intuitively and clearly demonstrated.

To begin, consider a dipole antenna of length $2h$ located along the z-axis as shown in Fig. 3.1. The radiated field can be viewed as a combination of the field radiated from the feed point and the two end points of the dipole at different instances in time [47,48]. To easily distinguish the radiation from these points in time, the current of the source is a Gaussian pulse given by

$$I_s(t) = I_0 e^{-(t/\tau)^2}. \tag{3.1}$$

where τ is the characteristic time of the pulse. In this discussion, τ is taken to be a fraction of the time required for the pulse, traveling at the speed of light, to travel the

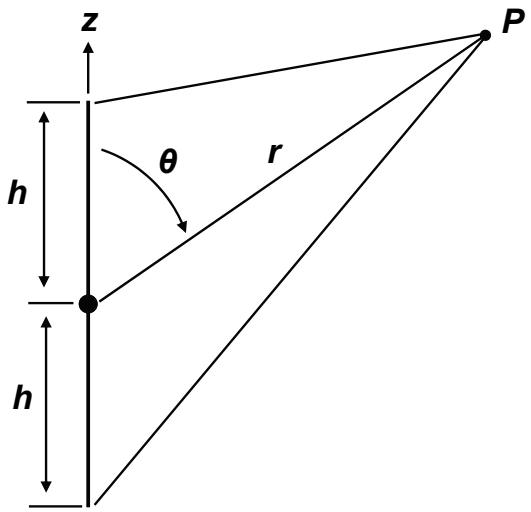

Figure 3.1: Schematic diagram of a dipole antenna and coordinate system.

length of the dipole ($\tau = 0.01h/c$). As in [47], it is initially assumed that the source produces a traveling wave of current (pulse of charge) propagating at the speed of light in the $+z$ direction. At the same time, another traveling wave of current propagates at the speed of light in the $-z$ direction. Upon reaching the end points, both waves are totally reflected at time $t = h/c$. Subsequently, the reflected traveling waves return to the source where it is assumed that they are totally absorbed at time $t = 2h/c$. In reality, the traveling waves are not totally absorbed at the source. Instead, they repeatedly travel back and forth between the feed point and end points until all of the energy is radiated. However, to simplify the discussion, only the radiation which is produced at the following instances in time is considered: 1) At time $t = 0$, when the charge is accelerated as the pulse leaves the source. 2) At time $t = h/c$, when the charge is decelerated as the pulses are reflected from the end points. 3) At time $t = 2h/c$, when the charge is decelerated as the reflected pulses are absorbed at the

feed point. It is also assumed that as the waves travel along the element they do so at a constant velocity so that no radiation is produced. For each of these instances in time, a spherical wave front centered at either $z = 0, h$ or $-h$ is created. Therefore, the far-zone radiated electric field is a superposition of the wave fronts which can be written as [47]

$$\begin{aligned}\mathbf{E}^r(\mathbf{r},t) &= \frac{\mu_0 c}{2\pi r sin\theta}\{I_s(t-r/c)+I_s(t-r/c-2h/c)\\ &\quad -I_s(t-r/c-(h/c)(1-cos\theta))\\ &\quad -I_s(t-r/c-(h/c)(1+cos\theta))\}. \end{aligned} \tag{3.2}$$

It is relatively straight forward to identify that the first term is associated with the initial radiation from the feed point. The second term is associated with the wavefront produced by the absorption of the reflected pulses at time $t = 2h/c$. The last two terms are associated with the radiation from the end points which occurs at time $t = h/c$. Since the spherical wave front associated with the end points is centered at $z = \pm h$, their contribution to the total radiated field is dependent upon the observation angle θ. With the observation point fixed at some angle θ and a distance r_P in the far-field, the arrival of the radiated waves are recorded with respect to time. To establish a baseline, consider the case where the dipole is a half-wavelength ($h = \lambda/4$) in length and the observation angle θ equals $\pi/2$. Fig. 3.2 shows the arrival of the Gaussian pulses as a function of time which has been normalized to characteristic time τ and the propagation delay from the origin to r_P has also been removed. The first pulse is from the initial radiation at the feed point and the second pulse with negative amplitude is due to radiation from the end points which arrives simultaneously because $\theta = \pi/2$. The last pulse is of course from the absorption of

the reflected pulses at the feed point. It is evident that there is little overlap between the pulses leading to predominately constructive interference and it is the reason for the pattern peak at broadside.

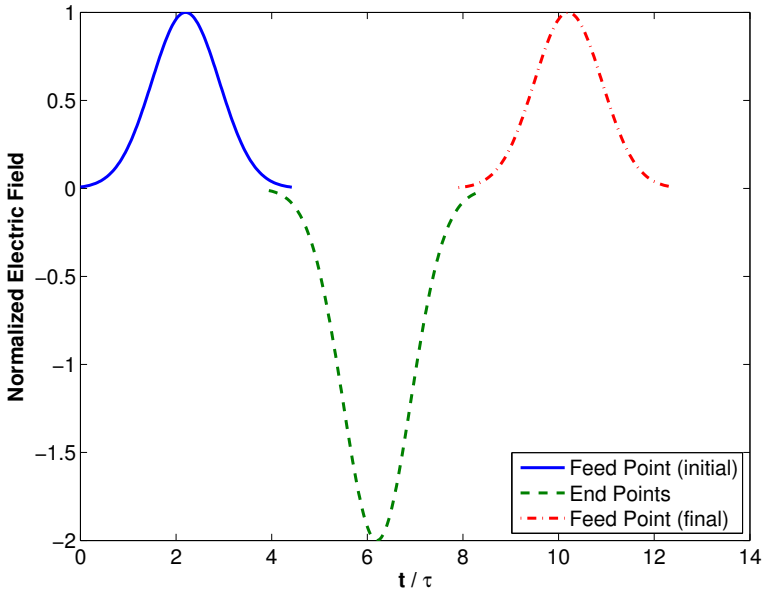

Figure 3.2: Gaussian pulse radiation from a $\lambda/2$ dipole for $\theta = \pi/2$.

Let us now consider the case where the dipole is electrically small ($h = \lambda/10$) as shown in Fig. 3.3. As expected, the arrival of the pulses overlap in time because the length h is shorter but the phase velocity v_p has remained the same. It is apparent that the shorter delay results in predominately destructive interference and becomes more destructive as the delay becomes shorter. Hence, antenna radiation begins to deteriorate with respect to the $\lambda/2$ dipole. However, if the phase velocity is reduced, the pulses can be made to interfere constructively once again. That is, if the dipole is miniaturized by a factor $m = v_p/c = 2h/\lambda$ the radiation becomes coherent and the performance improves. Therefore, the essence of antenna miniaturization is the

establishment of a coherent radiation condition or resonance when an antenna is electrically too small to achieve it otherwise. It is important to emphasize that the performance improvement achieve through miniaturization is limited by the electrical size of the antenna. This fact is demonstrated in section 3.3. Before proceeding to this demonstration, it is worthwhile to discuss how the phase velocity can be reduced.

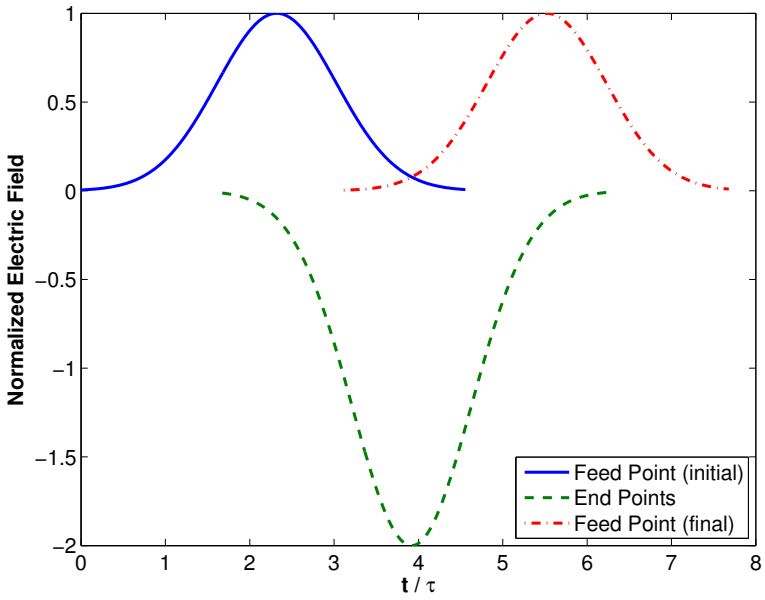

Figure 3.3: Gaussian pulse radiation from an electrically small dipole ($h = \lambda/10$) for $\theta = \pi/2$.

3.2 Antenna Miniaturization Concept

As illustrated in the previous section, the basic concept of miniaturization involves reducing the phase velocity of the wave guided by the antenna structure. To illustrate how this can be done, the analogy between an antenna and transmission line is used again (see section 2.6.1). Consider a center-fed infinite biconical antenna which is a

type of a spherically radial waveguide guiding a purely spherical wave [3]. This is analogous to an infinitely uniform transmission line acting like a guide for a traveling plane wave [45]. It is well known that the phase velocity v_p and characteristic impedance Z_0 seen by the guided wave are given by

$$v_p = \frac{1}{\sqrt{LC}} = \frac{1}{\sqrt{\mu\epsilon}}, \qquad Z_0 = G\sqrt{\frac{L}{C}} = G\sqrt{\frac{\mu}{\epsilon}} \tag{3.3}$$

where L is the series inductance per unit length, C is the shunt capacitance per unit length and G is a geometrical factor. Using the analogy between antenna and transmission line, these same equations apply to an antenna[9]. Therefore, the phase velocity can be controlled using the series inductance and shunt capacitance per unit length. For the biconical antenna, this means controlling the self-inductance of the cone and the capacitance between the two cone halves. Below, some techniques are discussed for modifying the inductance and capacitance of the antenna structure.

Techniques that can be used to modify the inductance and capacitance of an antenna structure involve either material or reactive loading. Material loading refers to the application of materials which have $\epsilon_r > 1$ and/or $\mu_r > 1$. This approach is the most generic making it applicable to any antenna design. However, the material density can make this approach prohibitive for applications that require lightweight antenna designs. Additionally, material losses can play a significant role in their applicability. Thus, frequency dependent loss for currently available magnetic or magneto-dielectric materials prevents their use above VHF. On the other hand, reactive loading refers to any method which enhances the self-inductance and/or shunt-capacitance within the antenna structure. A classic example of inductive loading is

[9]In general, the characteristic impedance of an antenna is frequency dependent unless the geometry naturally scales with frequency (constant geometrical factor).

the meandering of the conductor forming the antenna [11, 49]. Not only is this approach lightweight but it is also applicable for any frequency range. However, for some antennas, it can be difficult, if not impossible, to implement capacitive and/or inductive loading.

3.3 Performance Enhancement caused by Antenna Miniaturization

Before proceeding with the examination and implementation of miniaturization techniques, it is important to assess the improvements that can be achieved through miniaturization. To begin, consider a wire dipole and loop antenna both of which fit inside a sphere of radius a. That is, they both have a maximum linear dimension equal to $2a$. Under these constraints, the dipole will have its first resonance at $ka \approx \pi/2$ and the loop will have an antiresonance [10] at $ka \approx 1/2$ and its first resonance at $ka \approx 1$. These values are approximate because they also depend on the wire radius as well. The dipole and loop can be miniaturized by increasing the self inductance of the wire segments that form them. This is readily accomplished using NEC [50] which allows the user to assign a distributed or lumped impedance (parallel or series circuit) to each wire segment. In this case, each segment was assigned the same distributed inductance L (uniform loading). In doing so, the resonant frequency is shifted to a lower frequency as the self-inductance is increased. The ratio of the resonant frequency for the unloaded case ($L = 0$) to the loaded case ($L > 0$) is defined here in as the miniaturization factor m ($m = f_u^{res}/f_l^{res}$). Fig. 3.4 shows the miniaturization factor obtained for a given inductance per unit length and it is

[10] Antiresonance is defined by the condition where the reactance is zero and its derivative is negative (parallel RLC circuit). Similarly, a resonance occurs when the reactance is zero and the derivative is positive (series RLC circuit).

remarked that the relation between m and L for the loop and dipole antennas is identical. In fact, in the discussion that follows, the results are nearly identical for the dipole and loop. Therefore, to avoid being redundant, most of the subsequent results are shown only for the dipole antenna.

The following two sections discuss the impact antenna miniaturization has on the radiation efficiency and Q. These sections illustrate the importance of phase velocity in improving antenna performance. Section 3.3.3 then illustrates how the electrical size in terms of the free space wavelength limits the improvement that can be obtained by miniaturization.

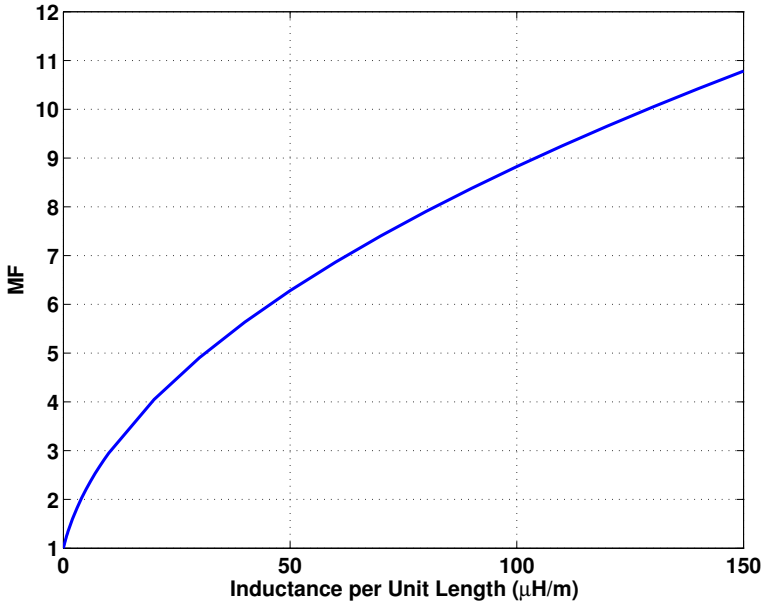

Figure 3.4: Miniaturization factor as a function of the inductance per unit length for a dipole or loop antenna.

3.3.1 Radiation Resistance

The radiation resistance is an important antenna parameter, especially in transmitting systems, because it plays a significant role in determining the fraction of the accepted power that is radiated and dissipated. Therefore, it is of interest to examine how antenna miniaturization affects radiation resistance. The radiation resistance is typically referred to current maximum[11]. The radiation resistance of a unloaded dipole is plotted in Fig. 3.5 in addition to several cases where the dipole has been miniaturized by a factor of m (the reactance is shown in Fig. 3.6). As seen, the radiation resistance for the unloaded dipole decreases with decreasing ka as expected. However, if the behavior of the radiation resistance is observed at a fixed ka, it can have larger values depending upon the miniaturization factor m. This is demonstrated in Fig. 3.7 which shows the radiation resistance at $ka = 0.5$ as a function of m. As the resonant frequency of the miniaturized dipole approaches $ka = 0.5$ (as m increases), the radiation resistance increases and eventually peaks. As m continues to increase, the radiation resistance begins to decrease because the resonant frequency has moved past $ka = 0.5$. This behavior illustrates the importance of phase velocity. By choosing the appropriate miniaturization factor, the phase velocity can be reduced making the dipole resonate. Therefore, even though the dipole is physically small, the dipole current distribution can be made sinusoidal as shown in Fig. 3.8 (red dash-dot line). When the dipole is resonant, radiation from the feed point and ends interferes constructively allowing maximum energy transfer into propagating spherical wave modes. In terms of antenna parameters, this manifests itself as a larger radiation resistance.

[11]The radiation resistance relative to current maximum is: $R_m(\omega_0) = R_{in}(\omega_0)\left(\frac{I_{in}(\omega_0)}{I_m(\omega_0)}\right)^2$ where I_m is the maximum current, I_{in} is the current the terminals and R_{in} is the resistance seen looking into the terminals.

Assuming the ohmic-loss remains constant, the increased radiation resistance leads to a higher radiation efficiency and more power radiated.

In comparison, the unloaded dipole has a triangular current distribution (solid line in Fig. 3.8) and the radiation from the feed point and ends interferes primarily destructively. By complex conjugate matching the unloaded dipole using a lumped load at the input terminals, the power radiated increases since the power accepted by the antenna increases (current amplitude increases). However, the radiation resistance remains unchanged as well as the radiation efficiency because the antenna is still non-resonant. That is, complex conjugate matching does not effect the phase velocity and cannot make the antenna resonate[12] (the resonance exists between the lumped load and the antenna). Therefore, in this regard, miniaturizing an antenna is more beneficial than the complex conjugate matching of a non-resonant antenna. In the following section, the impact of antenna miniaturization on the radiation Q and impedance bandwidth is examined.

3.3.2 Antenna Q and Bandwidth

After observing how antenna miniaturization affects radiation resistance, one should also expect it to also affect the Q. The impact of antenna miniaturization on the Q is demonstrated in Fig. 3.9 where the antenna Q was calculated from the antenna impedance using the following expression [51][13].

$$Q\left(\omega_0\right) \approx \frac{\omega_0}{2R\left(\omega_0\right)} \sqrt{\left[R'\left(\omega_0\right)\right]^2 + \left[X'\left(\omega_0\right) + \frac{\left|X\left(\omega_0\right)\right|}{\omega_0}\right]^2}. \tag{3.4}$$

[12]Note that when the electrical size becomes very small (i.e. for HF antennas, $ka << 0.1$), the tunning circuit and antenna are, for all practical purposes, indistinguishable from one another. Therefore, miniaturization and tunning are basically one in the same

[13]The derivatives in equation 3.4 where evaluated numerically using the five point rule with a step size $h = 10kHz$

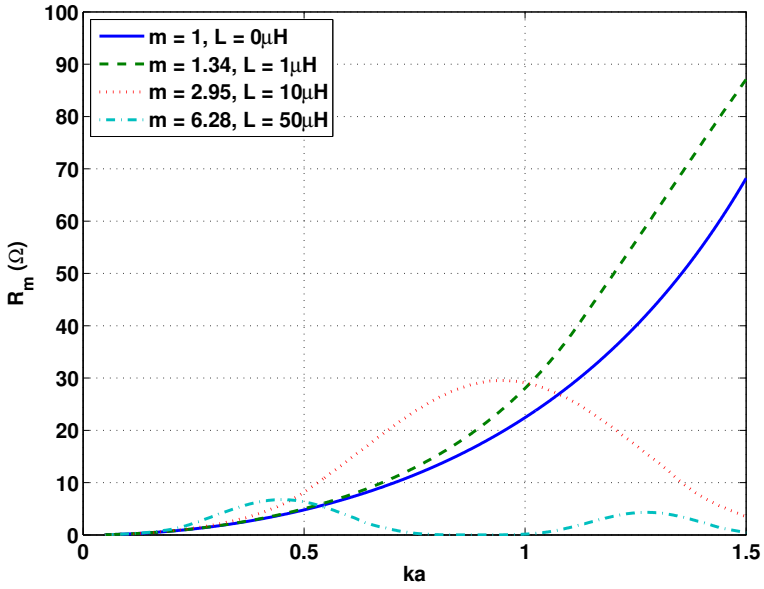

Figure 3.5: Comparison of the dipole radiation resistance for different miniaturization factors.

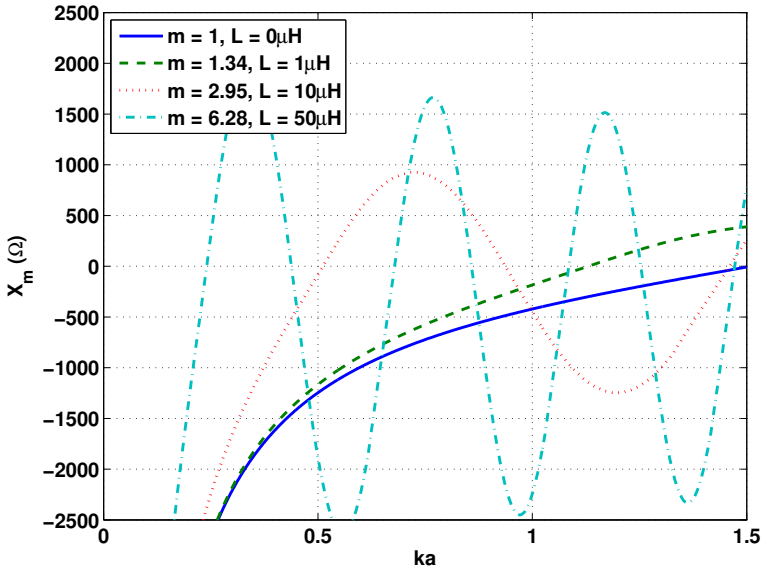

Figure 3.6: Comparison of the dipole reactance referred to current maximum for different miniaturization factors.

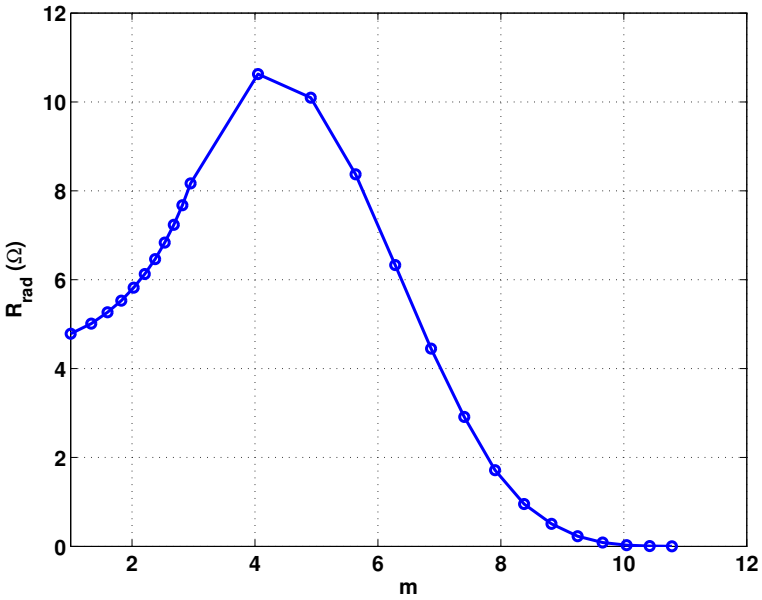

Figure 3.7: Dipole radiation resistance at $ka = 0.5$ as a function of the miniaturization factor m.

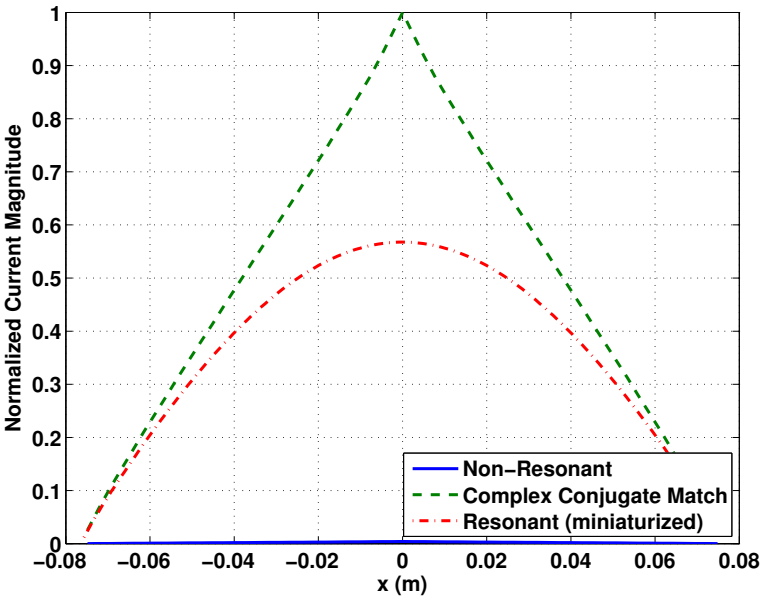

Figure 3.8: Comparison of the current distribution at $ka \approx 0.5$ for a 6 inch long unloaded dipole below resonance and real impedance match, below resonance and complex conjugate matching and a resonant dipole via miniaturization (real impedance match).

In [51], it was shown that this expression was in close agreement with the exact Q calculated from the fields. To observe the impact of miniaturization on the Q, the Q of the dipole is observed at a fixed ka. In Fig. 3.9, the Q is plotted as a function of the miniaturization factor for various values of ka. For each ka, the dipole Q has been normalized using the Q of the unloaded dipole ($m = 1$ case). This normalization was done only to make all of the curves viewable on the same plot. From Fig. 3.9 it is evident that the Q decreases as m increases until a minimum is reached. The value of m for which the minimum Q occurs corresponds the miniaturization factor required to make the dipole resonate at a given ka. This can be better depicted by re-plotting the results using the effective electrical size $k_m a$. That is, the miniaturization factor (x-axis) is multiplied by ka and the Q is re-plotted in Fig. 3.10 as a function of mka ($k_m a = mka$). Recalling that the unloaded dipole resonates at $ka = \pi/2$, it is evident that the minimum normalized Q occurs at $k_m a = \pi/2$, implying an effective propagation constant k_m. This plot also demonstrates the importance of using phase velocity to establish resonance or a coherent radiation condition at a given ka. More importantly, this result shows that the optimal miniaturization factor with respect to Q is simply the miniaturization factor required to make the dipole resonate at a given ka.

Since the loaded has a lower Q compared to the unloaded dipole for a given ka, it will also have a larger impedance bandwidth. To demonstrate this, equation 2.27 is used to determine the fractional bandwidth assuming an infinite stage matching network ($a = \pi, b = 0$) and a reflection coefficient, $\Gamma = 10^{-0.5}$ (-10 dB return loss bandwidth). The fractional bandwidth was then computed for the unloaded and loaded dipole as a function of ka. For each ka, the loaded dipole has been miniaturized using

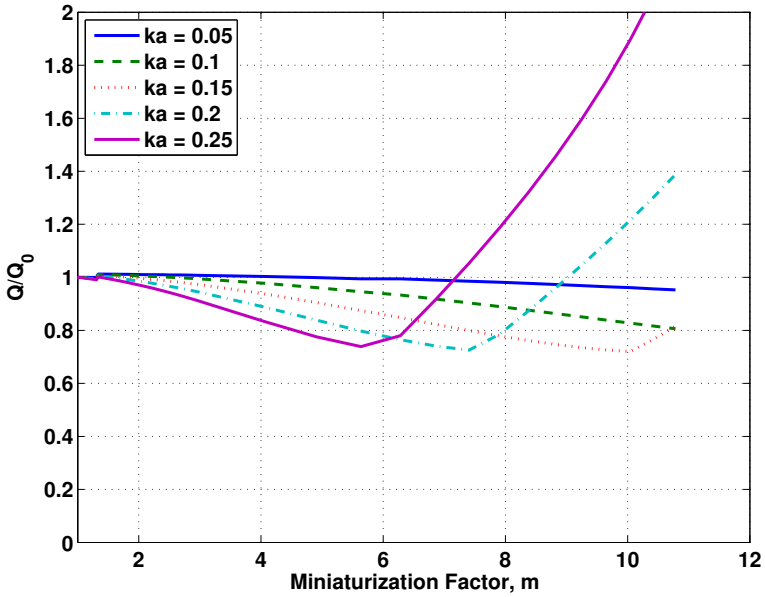

Figure 3.9: The normalized dipole Q (at a fixed ka) as a function of the miniaturization factor m.

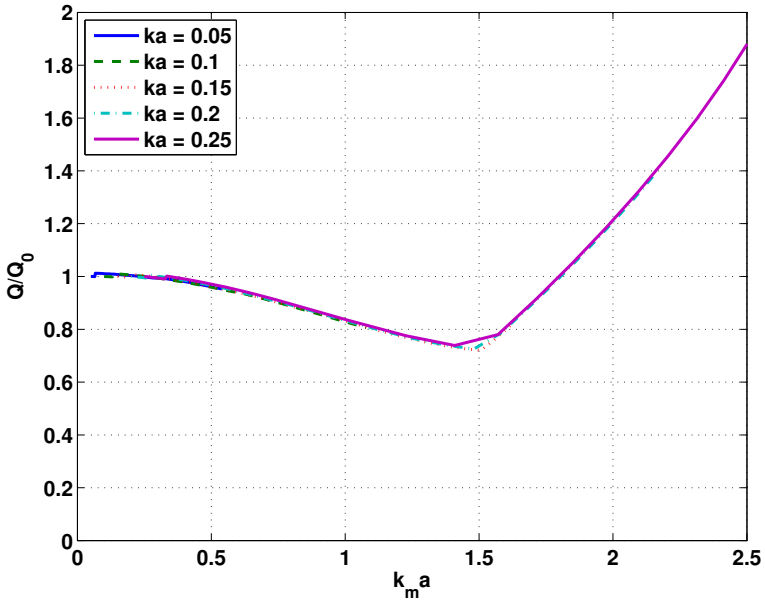

Figure 3.10: Dipole Q as a function of $k_m a$.

the appropriate m such that it is resonant. A comparison of the fractional bandwidth is shown in Fig. 3.11. It is evident that miniaturization improves bandwidth because the miniaturized dipole has a lower Q. To better illustrate this, the percentage bandwidth improvement obtained from miniaturization is shown in Fig. 3.12. As seen, up to 40% improvement is possible if the dipole is resonant (miniaturized) at a given ka. For the loop antenna, the percentage bandwidth improvement is provided in Fig. 3.13. While its percentage improvement is not as large as the dipole, the two miniaturized antennas have nearly the same fractional bandwidth for $ka < 0.5$.

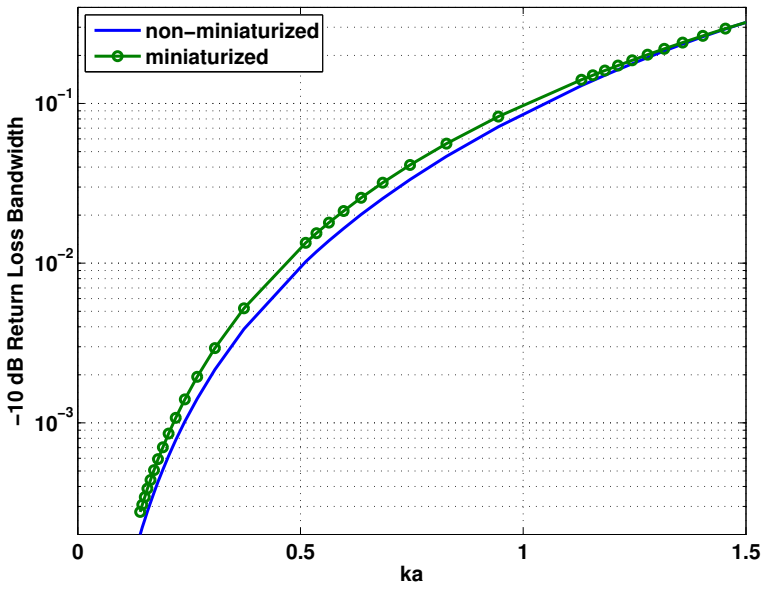

Figure 3.11: Fractional bandwidth (based on -10 dB return loss) improvement for a miniaturized dipole (resonant at each ka) using an infinite stage matching network.

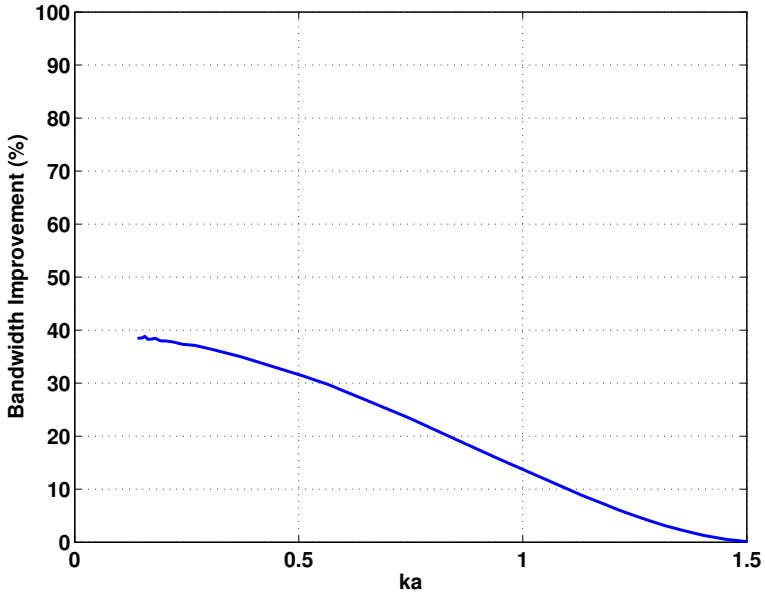

Figure 3.12: Percent improvement in the -10 dB return loss fractional bandwidth for a miniaturized dipole using an infinite stage matching network.

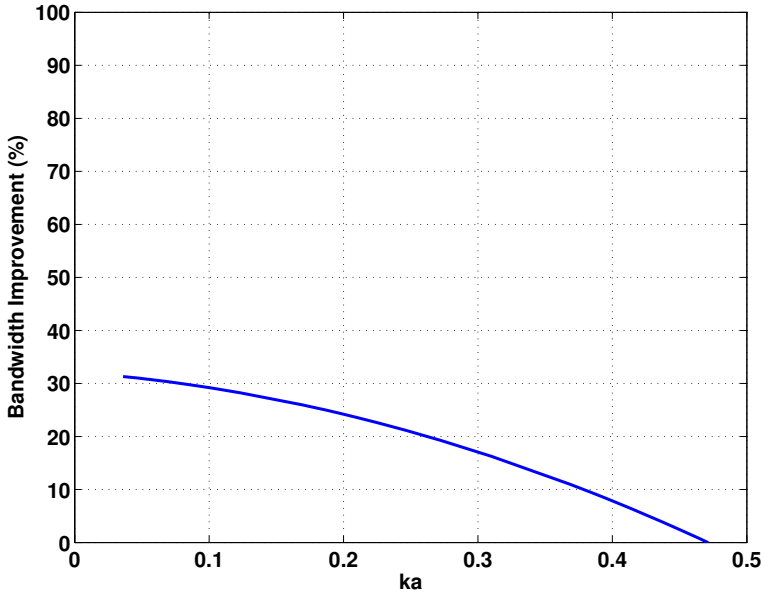

Figure 3.13: Percent improvement in the -10 dB return loss fractional bandwidth for a miniaturized loop using an infinite stage matching network.

3.3.3 Electrical Size

The two preceding sections have shown improvements that can be achieved using antenna miniaturization. However, the improvement is limited by the electrical size of the antenna. That is, an electrically small dipole ($ka << \pi/2$) can be made to resonate via miniaturization ($k_m a = \pi/2$) but its performance will never be as good as an electrically large resonant dipole ($ka = \pi/2$). This is best illustrated by examining what happens to the dipole impedance as it is miniaturized.

From Figures 3.5 and 3.6, it is apparent that the dipole's impedance curves are shifted in frequency as it is miniaturized. Furthermore, the impedance curves are also scaled as the dipole is miniaturized. The resulting impedance curves for the miniaturized appear to be shifted and scaled versions of the unloaded dipole impedance. This shifting and scaling indicates that there this a relation between the dipole's impedance before and after miniaturization. To determine this relationship, the real and imaginary parts of the impedance are considered separately. It is also assumed that the scaling functions that relate the dipole's resistance and reactance before and after miniaturization are frequency dependent. Therefore, in general, the relation between the dipole's resistance before and after miniaturization can be stated as follows

$$R\left(\frac{\omega}{m}\right) = s_R\left(\omega\right) R_0\left(\omega\right). \tag{3.5}$$

where R_0 denotes the resistance before miniaturization, R is the resistance after miniaturization and s_R is the unknown scaling function. Similarly, the relation between the dipole's reactance before and after miniaturization is given by

$$X\left(\frac{\omega}{m}\right) = s_X\left(\omega\right) X_0\left(\omega\right). \tag{3.6}$$

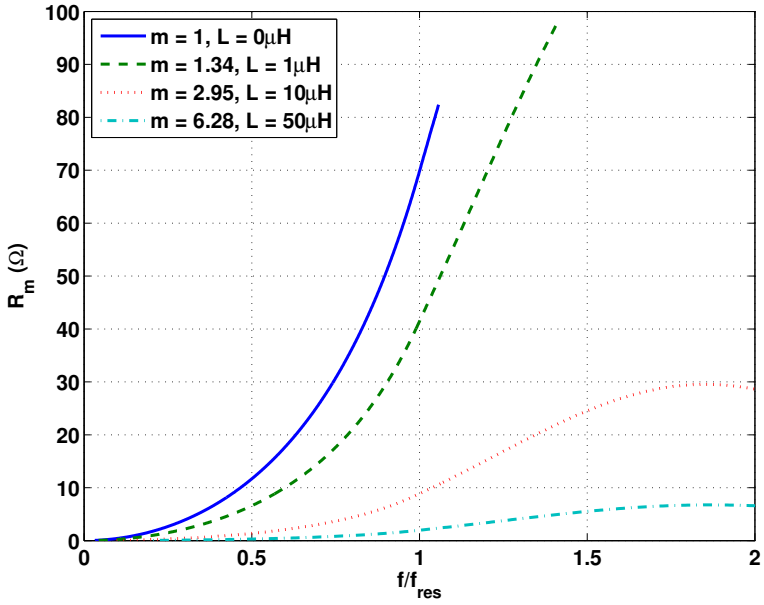

Figure 3.14: Comparison of the dipole radiation resistance for different miniaturization factors as a function of the normalized frequency.

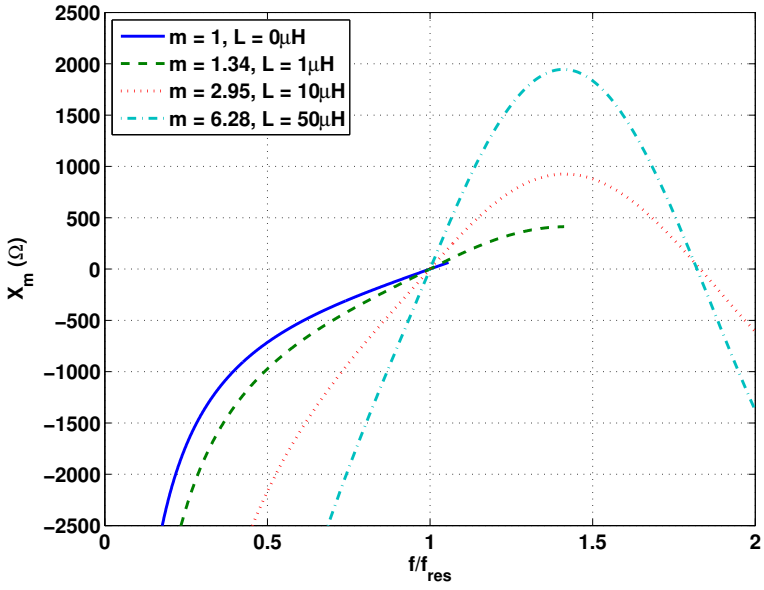

Figure 3.15: Comparison of the dipole reactance referred to current maximum for different miniaturization factors as a function of the normalized frequency.

To determine the scaling functions s_R and s_X, the impedance curves of Fig. 3.5 and 3.6 are re-plotted in Fig. 3.14 and 3.15 respectively, as a function of the normalized frequency $\frac{f}{f_{res}}$ where f_{res} denotes the resonate frequency of the dipole in each case. By dividing the curve for the unloaded case ($m = 1$) by one of the curves for the loaded case ($m \neq 1$), it can be shown that the scaling functions are almost constant functions of frequency (see Figures 3.16 and 3.17). More specifically, the dipole resistance after miniaturization by a factor of m has been scaled by a factor of $1/m^2$ (see Fig. 3.16). Also, as shown in Fig. 3.17, the reactance increases by a factor of m after miniaturization. Therefore, the relation for the dipole resistance and reactance before and after miniaturization is

$$R\left(\frac{\omega}{m}\right) \cong \frac{1}{m^2} R_0\left(\omega\right) \tag{3.7}$$

$$X\left(\frac{\omega}{m}\right) \cong m X_0\left(\omega\right). \tag{3.8}$$

In essence, these expressions demonstrate that, for a fixed physical size, the radiation resistance and associated reactance (relative to current maximum) are not maintained as the resonant frequency is shifted to lower frequencies. This is a result of the antenna becoming electrically smaller which, in turn, results in a larger radiation Q. From equations 2.8and 3.4, a larger Q implies that less energy is radiated (a smaller radiation resistance) and more energy is stored (larger magnitude and derivative of the reactance) which can be inferred from equations 3.7 and 3.8. Therefore, these equations further illustrate the importance of electrical size (with respect to the free space wavelength) in limiting the performance of an antenna.

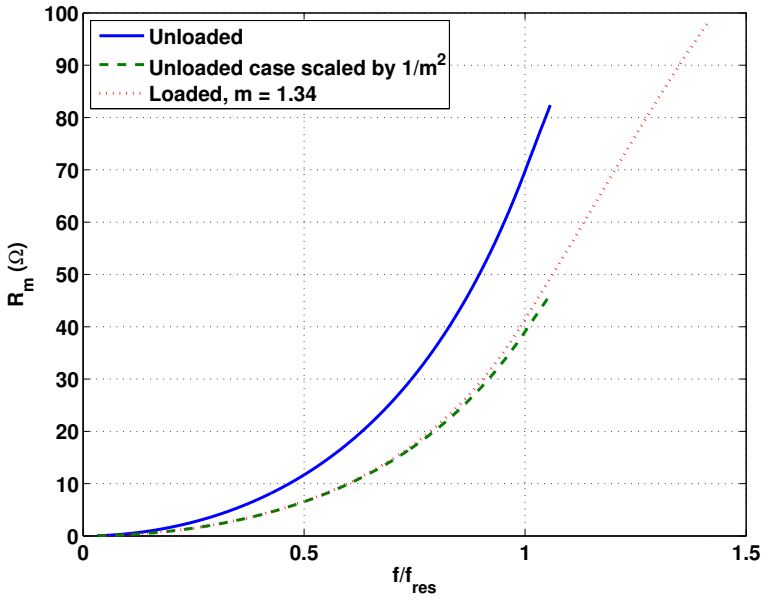

Figure 3.16: Scaling of the dipole resistance due to miniaturization (resistance is with respect to current maximum).

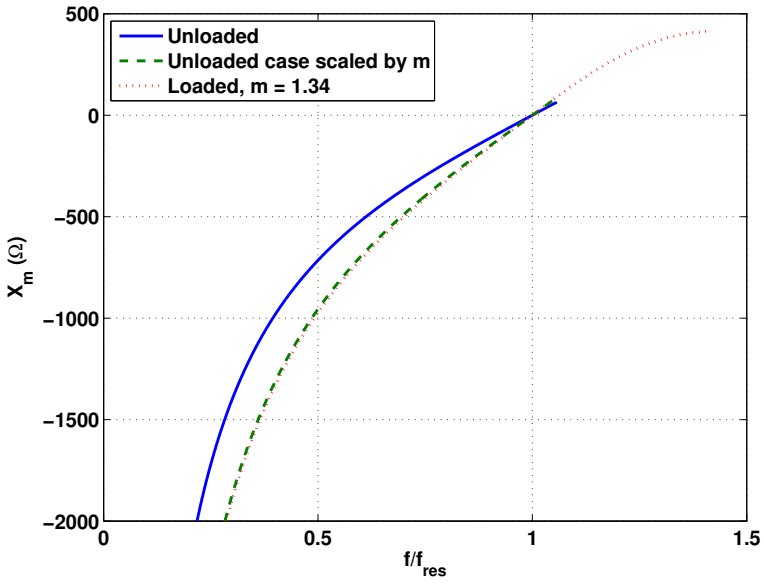

Figure 3.17: Scaling of the dipole reactance due to miniaturization (reactance is with respect to current maximum).

3.4 Approach to Broadband Antenna Miniaturization

Until now, antenna miniaturization was discussed and illustrated from the point of view of narrow band antennas. This allowed important concepts to be easily demonstrated using simplistic antennas. The purpose of this section is to discuss the miniaturization of broadband antennas in general. The goal is to develop a methodology for miniaturizing a broadband antenna such that the best overall performance is achieved. As a first step, section 3.4.1 discusses the possibility of defining an optimal miniaturization factor for a wire spiral antenna. Section 3.4.2 then examines how the loading profile impacts the performance of a spiral antenna. Motivated partly by the result in section 3.4.2, section 3.4.3 discusses the benefit of equal inductive and capacitive loading for broadband antennas.

3.4.1 Optimum Miniaturization Factor

It was previously shown for a dipole and a loop that, in regards to the Q, the optimal miniaturization factor is the one required to make the antenna resonate at a desired frequency. That is, the optimal miniaturization factor is equal to the resonant frequency of the unloaded antenna divided by the desired resonant frequency $\left(m_{opt} = \frac{f_{res}}{f} = \frac{\pi/2}{ka}\right)$. Intuitively, this should apply to any antenna including the spiral antenna. For the spiral antenna, radiation band theory [52, 53] says that the first radiation band will be formed at $ka = 1$ ($D = \lambda/\pi$). This implies that optimal miniaturization factor m for a spiral would be $m = 1/ka$. To verify this, the same analysis procedure used in section 3.3 for the dipole and loop was repeated for a 6 inch diameter wire log spiral shown in Fig.3.18.

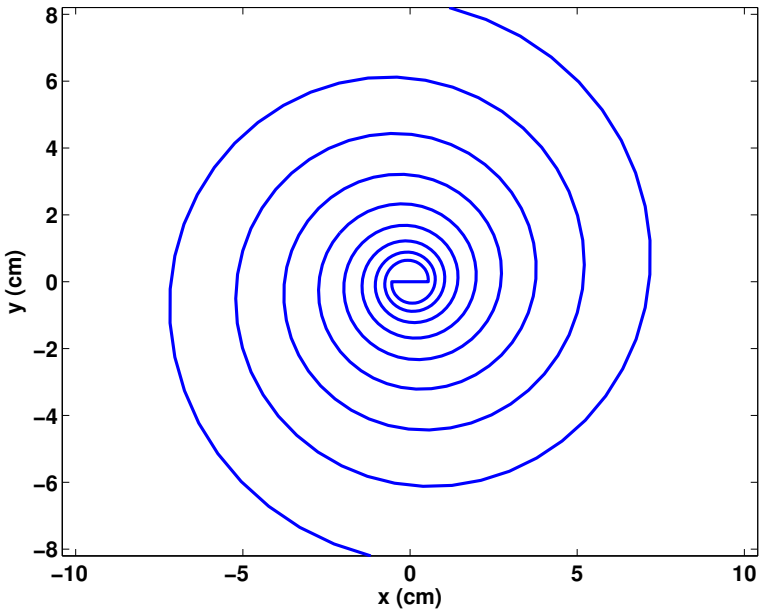

Figure 3.18: A 6 inch diameter wire log spiral with an expansion ratio $\tau = 0.525$ (growth rate $a \approx 0.1$) and angle $\delta = \pi/2$.

For each m, the Q of the spiral was calculated for a range of ka using equation equation 3.4. To determine the optimal m for a given ka, the spiral Q is plotted as a function of m for fixed values of ka (see Fig. 3.19). In Fig. 3.19, the spiral Q was normalized to the theoretical limit at each ka so that all of the curves can be displayed on the same plot. It is apparent that for each ka a minimum is obtained for a different m as expected. The value of m for which the minimum occurs can be found by re-plotting the results using the effective electrical size $k_m a$ ($k_m = mk$) and this is shown in Fig. 3.20. It is apparent that the minimum occurs at $k_m a \approx 0.5\pi$, implying an optimal miniaturization factor of $m_{opt} \approx 0.5\pi/ka$. Note that this is the same m_{opt} obtained for the dipole antenna but it is larger than the predicted $m = 1/ka$ from radiation band theory. This is not unexpected as the performance of an unloaded ($m = 1$) spiral is not optimal at $ka = 1$. That is, the frequency

independent performance of the spiral does not begin exactly at $ka = 1$. To achieve frequency independent behavior, the current must decay sufficiently before it reaches the point where the spiral structure is truncated. For the spiral, the growth rate or expansion ratio determines how rapidly the current decays through the radiation band and beyond. Hence, depending upon the growth rate, the frequency independent behavior occurs when the radiation bands are located a sufficient distance from the truncation. Typically, the frequency independent performance is observed to begin for $1 < ka \leq \pi/2$. Therefore, the optimal miniaturization factor m_{opt} for a spiral will most likely depend to some extent on the growth rate. Nevertheless, the optimal miniaturization factor obtained using a growth rate $a = 0.1$ is still useful as long as it is used as a guideline for determining the maximum miniaturization factor. That is, the result provides a useful starting point in the design process for defining the maximum miniaturization factor that needs to be achieved. It is importance to emphasize that the optimal miniaturization factor, as defined here, is based on minimizing the spiral Q at a given ka. If it is defined in terms of maximizing the realized gain at a given ka then m_{opt} could be different depending upon how the antenna is matched.

3.4.2 Importance of Tapered Loading Profile

In designing a miniaturized broadband antenna it is important to consider the manner in which the antenna is miniaturized. For instance, consider the miniaturization of a spiral antenna by a factor m. This miniaturization factor could be achieved by uniformly loading the spiral such that the phase velocity is reduced by a factor m everywhere along the spiral. On the other hand, the same miniaturization factor could be achieved by gradually decreasing the phase velocity along the spiral using

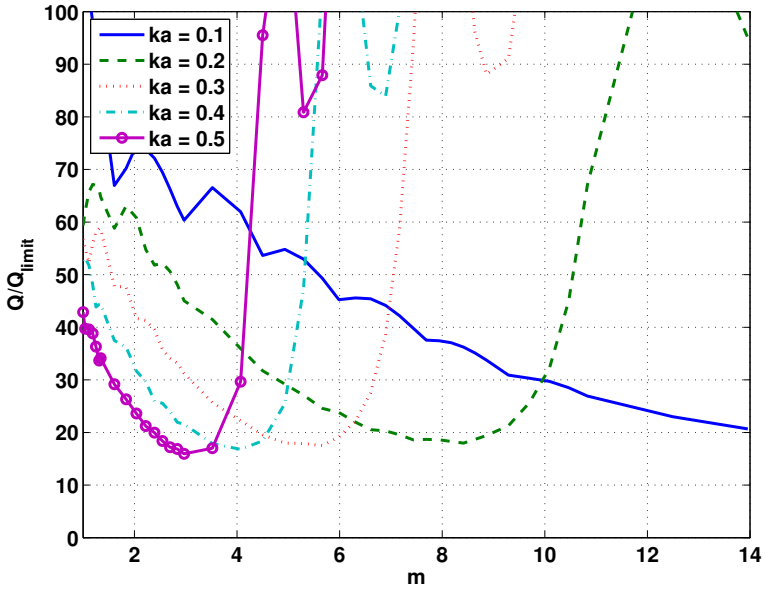

Figure 3.19: Behavior of the spiral antenna Q as a function of the miniaturization factor m for fixed values of ka.

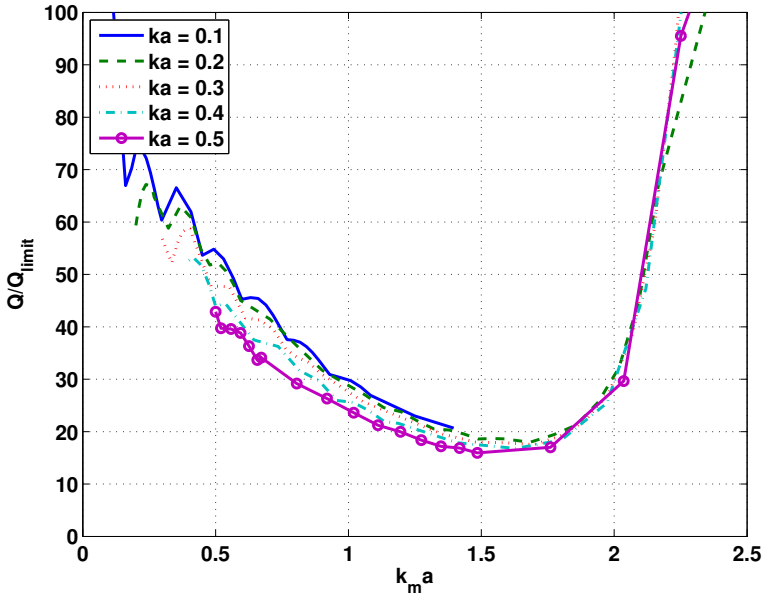

Figure 3.20: Behavior of the spiral antenna Q as a function of the effective electrical size $k_m a$ for fixed values of ka.

a tapered loading profile. This leads to the question: How does the loading profile impact the performance of a broadband antenna? To answer this question, let us consider the uniform loading of the 6 inch diameter spiral antenna shown in Fig. 3.21.

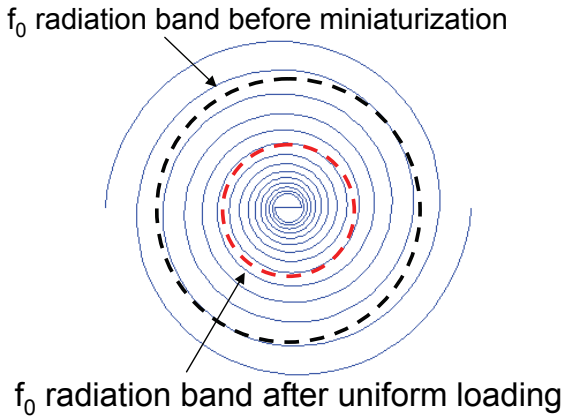

Figure 3.21: Spiral antenna miniaturization using material loading.

For a frequency f_0 there is a radiation band whose location is shown in Fig. 3.21 before the spiral is miniaturized. It is obvious that the spiral is electrically large enough to naturally establish a radiation band at f_0. Therefore, its performance at f_0 is sufficient and needs no further improvement. When the spiral is miniaturized by a factor m using a uniform loading profile, the location of the radiation band associated with f_0 shifts inward. In doing so, the size of the radiation band is also reduced by a factor of m. Therefore, the spiral now radiates from an electrically smaller aperture at the frequency f_0. As a result, the antenna Q increases and the directivity decreases. Therefore, while uniform loading can improve performance below some ka where the spiral was once too small to form a radiation band, it will concurrently deteriorate

performance at those frequencies where the spiral could already form a radiation band.

This is demonstrated by uniformly loading the spiral in Fig. 3.21 using an inductance per unit length of $5\mu H$ ($m = 2.21$). As evident from Fig. 3.22, the Q of the loaded spiral is lower than the unloaded spiral below approximately 600 MHz. Above 600 MHz, the loaded spiral Q is significantly higher because the radiation band has become electrically smaller. The effect of the electrically smaller aperture on the directivity is shown in Fig. 3.23 for the uniformly loaded and unloaded spiral. It is apparent that the directivity for the uniformly loaded spiral is several dB lower that the unloaded spiral. Also, the directivity for the uniformly loaded spiral exhibits an oscillatory behavior. The oscillations could be a result of the growth rate being too large for the given miniaturization factor or pattern distortion caused by radiation from higher order modes. Note that the oscillations can be reduced to a certain extent by decreasing the growth rate a, as shown in Fig. 3.24. However, on average the overall directivity will be lower than the unloaded spiral because of the smaller effective aperture. Also, it is noted that decreasing the growth rate has almost no impact on the antenna Q as shown in Fig. 3.25.

The obvious solution to the problem illustrated by uniform loading is to only load the low frequency portion of the spiral aperture or to use a tapered loading profile. In doing so, there will be minimal size reduction of the high frequency radiation bands. Note that it is impossible to miniaturize a broadband antenna without effecting some of the higher frequency components. To demonstrate the improvement obtained by tapering, the inductive loading was exponentially tapered along the length of the spiral arm starting with an inductance of $0.001\mu H$ and increasing to $5\mu H$. The effect

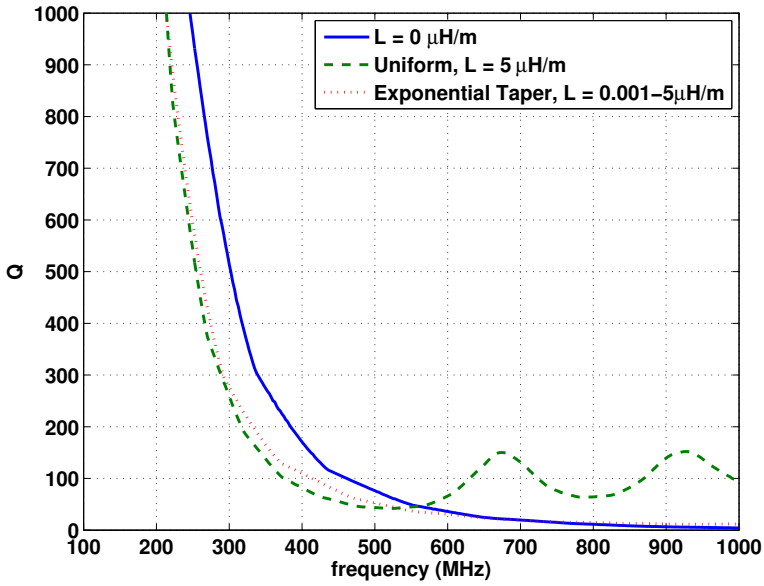

Figure 3.22: Comparison of the radiation Q for a spiral antenna having uniform and exponential inductive loading profile.

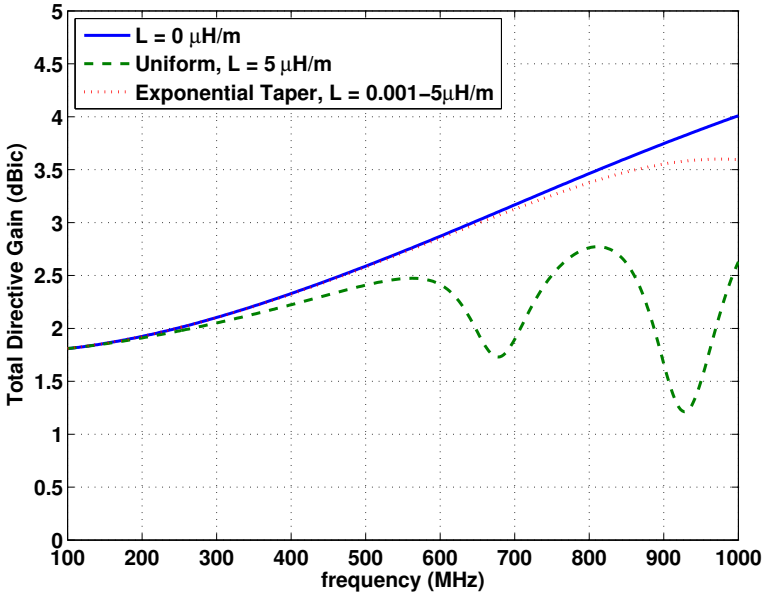

Figure 3.23: Comparison of the directive gain for a spiral antenna having a uniform and exponential inductive loading profile.

on the spiral Q and directivity are shown in Fig. 3.22 and Fig. 3.23 respectively. It is clear from Fig. 3.22 that the Q for the tapered loading is almost identical to the unloaded spiral at high frequencies as desired. Similarly, the directivity for the tapered loading is almost identical to the unloaded spiral. Note that the issue of choosing or determining the optimal loading profile is address later in section 5.3.

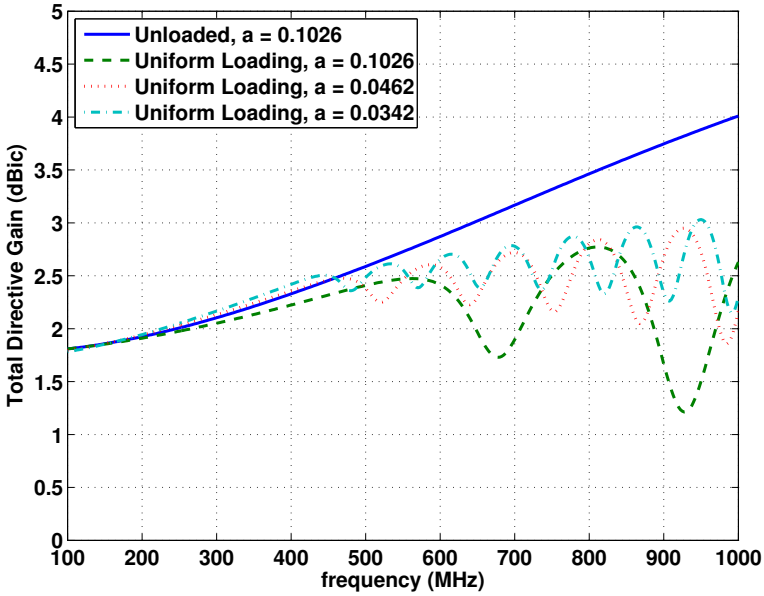

Figure 3.24: Comparison of the directive gain of a uniformly loaded spiral antenna for different growth rates.

3.4.3 Importance of Equal LC Loading

Even though a tapered loading profile alleviates many high frequency issues, it can cause additional issues if the loading is purely inductive or capacitive. Similar to a tapered transmission line matching section, a tapered loading profile introduces impedance discontinuities along the length of the spiral arm that, in turn, cause

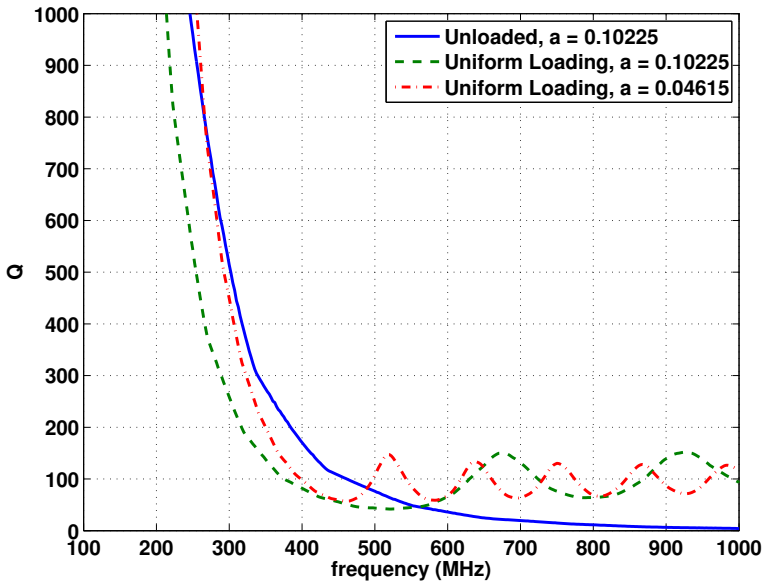

Figure 3.25: Comparison of the radiation Q of a uniformly loaded spiral antenna for different growth rates.

reflections. The magnitude of these reflections depends upon how large the impedance discontinuity is from one section to the next. As long as the impedance difference is small, the reflections due to the incremental change in impedance will also be small and will have minimal impact on the antenna input impedance. However, in theory, it is possible to eliminate any reflections that may occur from such loading if both inductive and capacitive loading are used simultaneously. That is, concurrent use of inductive and capacitive loading makes it possible to maintain the same impedance throughout the entire spiral structure as implied by equation 3.3.

The ability to maintain the impedance using both inductive (magnetic) and capacitive (dielectric material) loading can be demonstrated by analyzing a spiral antenna that is embedded in a fictitious material which has an arbitrary relative permeability and permittivity. Figure 3.26 shows a 6 inch diameter log-spiral embedded in a

1 cm thick disk of loss-less material. The spiral is a self-complementary structure consisting of seven turns and has a growth rate of $a = 0.06$. This antenna was simulated using Ansoft's HFSS for a disk with material properties of ($\epsilon_r = 4$, $\mu_r = 1$) and ($\epsilon_r = 2$, $\mu_r = 2$). The relative permeability and permittivity of the second material was chosen such that reduction in phase velocity was the same in both cases (same miniaturization factor). The resulting input impedance curves are shown in Figure 3.27. It is evident that the spiral loaded with only dielectric material has a much lower impedance than the spiral in free space. On the other hand, when the spiral is loaded with a material having equal ϵ_r and μ_r, the impedance is nearly identical to the free standing spiral. This clearly demonstrates the benefit of equal inductive and capacitive loading in regards to maintaining the original antenna impedance.

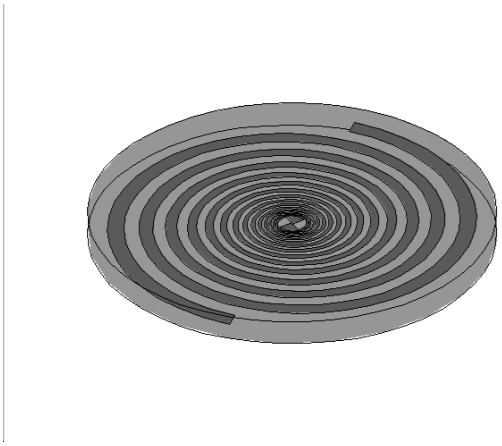

Figure 3.26: A 6 inch diameter log-spiral (self-complementary) embedded in the middle of a 1 cm thick disk of magneto-dielectric material.

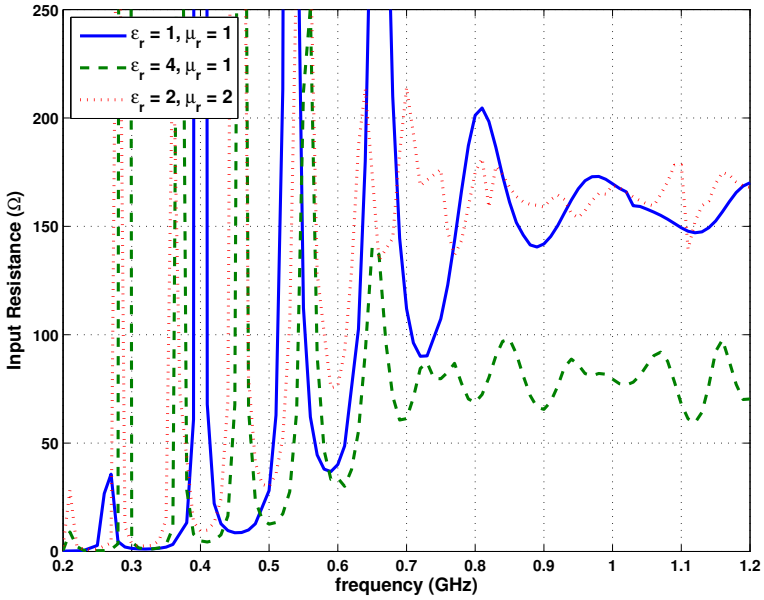

Figure 3.27: Input resistance for the spiral in Fig. 3.26 using different combinations of ϵ_r and μ_r.

3.5 Summary

In this chapter antenna miniaturization was discussed in general. Specifically, section 3.1 used a dipole antenna to illustrate the importance of phase velocity and electrical size in regards to radiation. The basic concept of controlling the phase velocity via antenna miniaturization was discussed in section 3.2. By controlling the phase velocity, it was possible to achieve resonance or to establish coherent radiation from an electrically small antenna. In doing so, the radiation Q, radiation resistance and impedance bandwidth could be enhanced to a certain degree as discussed in section 3.3. The last section discussed the proper application of miniaturization techniques to a broadband antenna. In doing so, a methodology was outlined for miniaturizing a broadband antenna, particularly a spiral antenna. Specifically, in

section 3.4.1, a guideline was established for determining the maximum miniaturization factor ($m_{opt} \approx 0.5\pi/ka$) needed to achieve optimal performance at a given ka with respect to the antenna Q. That is, the optimal miniaturization factor m_{opt} is based on minimizing the Q of a wire spiral at a given ka. Once again, it is emphasized that this result is only accurate when applied to a wire spiral antenna and it may not apply in general to any arbitrary spiral antenna. Nonetheless, the result is very useful for providing a starting point in the design process. Section 3.4.2 demonstrated the importance of tapering the loading profile to minimize any negative effects at higher frequencies. To eliminate possible issues introduced by tapering the loading profile, section 3.4.3 discussed the use of equal inductive and capacitive loading.

Using this knowledge, the following two chapters discuss the miniaturization of a spiral antenna using two different approaches which are material and reactive loading. Specifically, chapter 4 discusses broadband antenna miniaturization using material loading. Here, only dielectric material loading is considered because the currently available magnetic materials are too lossy over the frequency range of interest. Chapter 5 discusses the integration and implementation of reactive (inductive) loading for a spiral antenna. Only inductive loading is considered because of inherent difficulties in implementing capacitive loading for the spiral antenna.

CHAPTER 4

BROADBAND ANTENNA MINIATURIZATION USING MATERIAL LOADING

4.1 Introduction

Material loading is the most widely applicable approach for antenna miniaturization because any antenna can be easily miniaturized by immersing it in a high-contrast material. Therefore, the antenna does not need to be altered in any way as compared to reactive loading which usually requires structural modifications. The applicability of material loading is only limited by practical considerations (cost, size, weight, etc.) and the amount of loss which depends upon the material type (dielectric, ferrite, magneto-dielectric, etc.). The main practical issue is maintaining a low weight while maximizing the amount of miniaturization. Ideally, the entire volume occupied by the antenna (radian sphere) needs to be loaded to maximize the amount of miniaturization. However, such an approach is impractical because of the inherent increase in weight and large profile. Therefore, an inherent trade-off exists between material volume and achievable miniaturization.

The applicability of material loading also depends significantly upon the losses associated with the material. For this reason, the loss of currently available magnetic

or magneto-dielectric materials prevents their use above VHF frequencies. Also, it is noted that the real part of the permeability for magnetic materials which have cubic anisotropy is bounded by Snoek's limit [54, 55]. That is, there is a limit to the maximum relative permeability that can be achieved at a given frequency. According to Snoek's limit [54,55], the relative permeability is bounded by the following expression

$$\mu_r = \frac{1}{\omega}\frac{2\gamma M_s}{3} \tag{4.1}$$

where ω is the frequency, γ is the gyromagnetic ratio and M_s is the saturation magnetization. In practice, the majority of available magnetic materials only exhibit large relative permeabilities ($\mu_r > 20$) at frequencies less than 100 MHz. Therefore, the miniaturization that can be achieved using magnetic materials alone is limited by the frequency range of interest. However, the main issue with currently available magnetic materials is the loss. For this reason, the application of magnetic materials for the purpose of antenna miniaturization is limited to frequencies less than 200 MHz.

Unlike magnetic materials, the applicability of dielectric materials is not limited by loss or the relative permittivity that can be achieved. Currently available dielectric materials are low-loss (loss tangent, $tan\delta < 0.001$) and have a wide range of dielectric constants ($1 < \epsilon_r < 150$). The available dielectric materials are usually high-temperature ceramics, low-temperature cold fired ceramics or epoxy bonded ceramics. In addition, there are even dielectric materials made from plastic stock which exhibit low-loss ($tan\delta < 0.002$). All of these materials are readily available from a variety of companies such as Trans-Tech, Emerson and Cuming, picoFarad, and Dielectric Laboratories. Therefore, currently available dielectric materials are well suited for antenna miniaturization.

The idea of miniaturizing an antenna using dielectric loading has existed for quite some time and it has been employed frequently for narrow band. The dielectric materials used in these applications usually consisted of a low dielectric constant ($\epsilon_r < 10$) and a homogeneous layer due to fabrication limitations. Within the last ten years, there has been a renewed interest in the use of dielectric materials because of the interest in the design of novel materials for antenna applications (meta-materials) and the availability of low-loss (loss tangent, $tan\delta < 0.001$) and high-contrast dielectrics. In this Chapter, material loading of the spiral antenna is examined using only dielectric materials because of the previously mentioned issues with magnetic materials. The purpose is to demonstrate the use of dielectric materials and to determine how much the spiral can be miniaturized. The remainder of this chapter is organized as follows. In section 4.2, the theory of operation is briefly reviewed for the spiral antenna. The spiral antenna is then loaded using finite high-contrast dielectric layers (substrates and superstrates). The effect of the dielectric layer thickness, width and permittivity on the miniaturization of the spiral antenna is discussed. To facilitate dielectric loading, a previously developed design [49, 56, 57] is used as a baseline. In section 4.4, some of the issues that arise as a result of the high-contrast material loading are discussed and addressed.

4.2 Spiral Antenna: Theory of Operation

Regardless of the aperture shape of the spiral (circular or square) or its type (equiangular or archimedean), the theory of operation applies to all as long as they are tightly wound (expansion ratio, $\tau > 0.25$) [8]. The operation of the spiral antenna is based on "radiation band" theory which states that the spiral predominately radiates

from annular bands whose circumference is an integer multiple of a wavelength [52,53]. For a circular spiral the radiation bands occur when the diameter $D = n\lambda/\pi$ whereas for a square spiral they occur when the width $W = n\lambda/4$ [52]. Radiation occurs from these regions because the current flowing in adjacent arms is predominately in phase leading to coherent/constructive radiation in the far-field. Outside these regions the current is not in phase and, therefore, the radiated field interferes destructively. To illustrate the radiation band theory consider the two arm archimedean spiral shown in Fig 4.1 at some frequency f_0. Here, the two arms have been excited 180° out of phase with respect to the other and the phase progresses along the spiral arm in accordance with the free-space phase velocity. If the frequency is sufficiently large such that $\lambda_0 > \pi D$, the difference in phase between the current in adjacent arms will be small in an annular band whose circumference is λ_0. In Fig 4.1, the phase at selected points is shown on the spiral. It is evident that in the radiation band the phase difference is about 7° whereas outside the band the phase difference is significantly larger. Note that the phase difference in the radiation band is dependent upon the growth rate and decreases with decreasing growth rate (increasing expansion ratio, τ). As the operational frequency varies, the physical size of the radiation band varies accordingly. Therefore, the lowest operating frequency is determined by the spiral diameter or outer circumference. Similarly, the highest operating frequency is determined by the detail of the center region and can be increased by the addition of more turns.

Typically, the two arm spiral is excited so that the current on each arm is 180° out of phase with respect to the other at the feed point. For such an excitation the spiral can only radiate from regions where the circumference is an odd integer multiple of

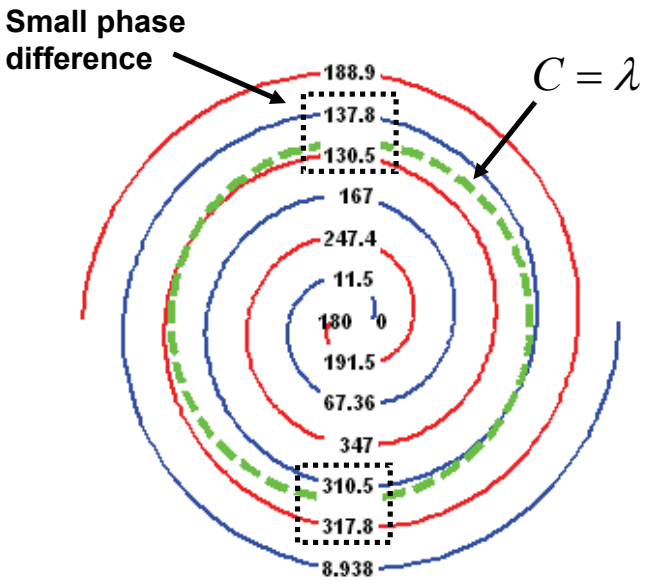

Figure 4.1: Phase of current flowing on a two-arm archimedean spiral antenna illustrating the concept of radiation band theory.

a wavelength (first mode). Specifically, radiation from the 1λ-circumference region will produce an omni-directional radiation pattern with the maximum at boresight. Only the first mode has a maximum at boresight and it is the most commonly used mode. However, if a two arm spiral is excited such that the currents on each arm are in phase, the coherent condition occurs when the circumference is an even integer multiple of a wavelength (second mode). The corresponding radiation pattern has a null at boresight and a maximum at an elevation angle of 38° from boresight (which can be predicted from array theory). All other radiation modes excited using spirals having more than two arms are similar to the second mode and are not discussed here. For further discussion of the radiation properties of these modes the reader is referred to [8, 58].

4.3 Spiral Antenna Miniaturization using High-Contrast Dielectrics

From radiation band theory, it is apparent that the location and size of the radiation band is dependent upon the phase velocity of the spiral structure. By manipulating the phase velocity the location and size of the radiation band can be controlled. That is, for a spiral with a phase velocity different than free-space, the circumference of the annular radiation band is equal to the guided or effective wavelength $\lambda_e = \lambda_0/\sqrt{\mu_e \epsilon_e}$ where λ_0 is the free-space wavelength, μ_e is the effective permeability and ϵ_e is the effective permeability. Clearly, by using high-contrast material or reactive loading, the effective wavelength can be made smaller than the free-space wavelength thereby miniaturizing the spiral. If the spiral were loaded with an infinite half-space or full-space, the effective dielectric constant is as follows

$$\epsilon_e = \begin{cases} \frac{\epsilon_r+1}{2} & \text{for infinite half-space} \\ \epsilon_r & \text{for infinite full-space} \end{cases} \tag{4.2}$$

This leads to a maximum achievable miniaturization (MAM) for single-side or double-side loading cases. In practice, the loading material has finite dimensions which actually define the overall size of the antenna. In this case, only a fraction of MAM is obtainable and the amount depends upon the thickness, width, shape of the material. In the remainder of this section, the miniaturization of a spiral antenna using dielectric materials is considered. The purpose is to observe how close one can come to achieving the MAM using a given dielectric constant. Before proceeding with this discussion, it is necessary to discuss the quantification of the miniaturization factor for a broadband antenna.

4.3.1 Quantifying Miniaturization for a Broadband Antenna

In light of the above discussion, a logical way to define the miniaturization factor is to use the ratio of the free-space wavelength to the effective wavelength ($m = \lambda_0/\lambda_e$). Since the resonant frequency of an antenna is dependent upon the effective wavelength (or phase velocity), defining the miniaturization factor in this way is equivalent to defining it using a ratio of the resonant frequencies for an unloaded and loaded antenna as in Chapter 3. However, for a broadband antenna (high pass response), defining the miniaturization factor based upon wavelength reduction is not the same as defining it using a ratio of the cutoff frequencies for an unloaded and loaded antenna $\left(m = f_c^{unloaded}/f_c^{loaded}\right)$. That is, reducing the wavelength or phase velocity by a factor of ten will not reduce the cutoff frequency by a factor of ten because there are physical limitations on the cutoff frequency (see section 2.6.1) that cannot be overcome[14]. Therefore, there are two miniaturization factors that can be defined for a broadband antenna. The miniaturization factor can be defined based upon phase velocity reduction and based on the shifting of the cutoff frequency. In evaluating the performance improvement due to miniaturization, the latter definition is more useful and will be used unless otherwise noted.

In order to calculate the miniaturization factor using the cutoff frequency, an antenna parameter must be chosen to define the cutoff frequency. Here on, the cutoff frequency is defined using a specific realized gain point. The realized gain is used because it incorporates three of the most important antenna parameters which are the directivity, radiation efficiency and the mismatch efficiency. The choice of the realized

[14]There are no such limitations for the resonant frequency (center frequency) of a band-pass response. That is, it is possible to shift the resonance to any frequency.

gain point can be chosen based upon a communication system requirement but, in general, the choice is subjective. It is important to note that the miniaturization factor can vary depending upon the matching condition. Throughout the remainder of this thesis, the mismatch efficiency is always calculated with respect to an arbitrary generator that has a purely real and constant impedance ($Z_0 = R_0$). The impedance Z_0 is determined by minimizing the reflection coefficient over a given frequency range as follows

$$min\left(\int_{f_1}^{f_2} |\Gamma|^2 \, df\right). \tag{4.3}$$

This is accomplished by using the Matlab function "*fminbnd*" which finds the minimum of a single-variable function over a fixed interval using golden section search and parabolic interpolation. In addition to varying with the matching condition, the miniaturization factor may vary based on the selected realized gain point. This is demonstrated in Fig. 4.2 for a spiral loaded by a dielectric layer of thickness t. Each curve in Fig. 4.2 was generated by calculating the miniaturization factor as a function of the dielectric layer thickness using different realized gain points. It is evident that the miniaturization factor is not the same for all realized gain points. However, for a realized gain less than -5 dBi, the miniaturization factor is relatively similar. Taking this into consideration, the -15 dBi realized gain point is used throughout the remainder of this thesis to define the miniaturization factor.

4.3.2 Impact of Dielectric Layer Dimensions

To begin the examination of the impact of dielectric loading, only one side of a planar spiral is loaded with dielectric material. Simulations (finite element-boundary integral code) are used to examine the effect of dielectric loading by varying the

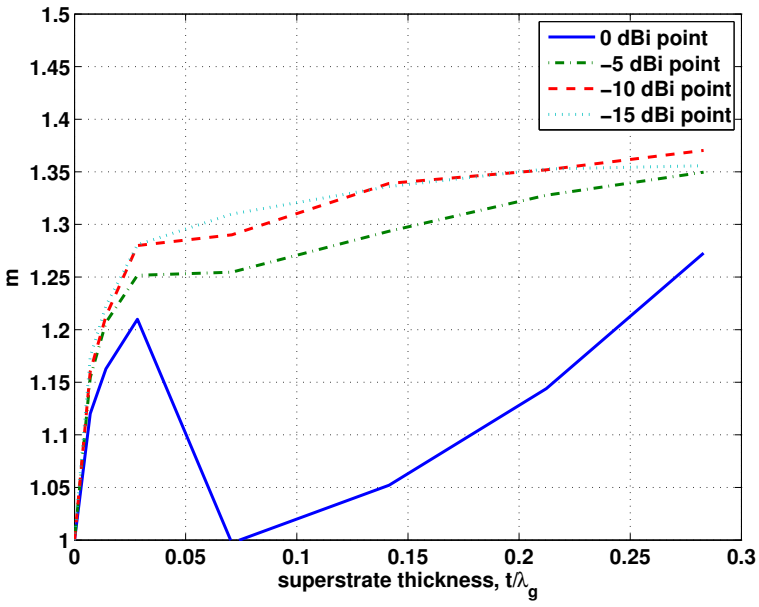

Figure 4.2: Dependence of the miniaturization factor on the realized gain point for a dielectric loaded spiral.

thickness t, dielectric constant ϵ_r and width L of the dielectric layer. The spiral used throughout is an archimedean square spiral with a constant growth rate as shown in Fig 4.3 ($w = 0.0762cm$, $S = 0.2286cm$ and $L = 5.3cm$).

The impact of the dielectric layer thickness on the miniaturization factor was considered first for the case where the dielectric layer width is equal to the spiral diameter. The thickness of the dielectric layer was varied for two cases where the dielectric constant was 9 and 16 respectively. The results are shown in Fig. 4.4 where the horizontal dashed lines represent the half-space loading MAM for a dielectric constant of 9 and 16. To make these results applicable for an arbitrary spiral size, the thickness has been normalized to the guided wavelength which is defined as $\lambda_g = \lambda_0/\sqrt{\epsilon_r}$ where λ_0 is four times the spiral diameter. Initially, it is observed that

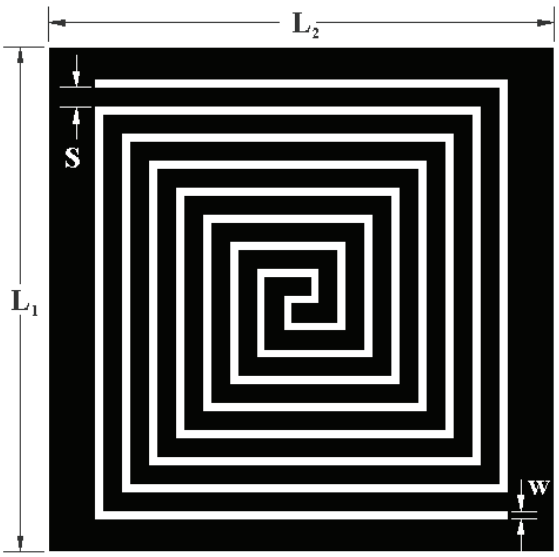

Figure 4.3: A two arm square Archimedean "slot" type spiral and geometrical parameters.

($t < 0.02\lambda_g$) the miniaturization factor m increases rapidly with increasing thickness for both cases. However, the rate at which m increases diminishes significantly as the thickness increases ($t > 0.1\lambda_g$) and begins to saturate before the MAM is reached in each case. Since the MAM can only be achieved by loading the entire half-space, it was expected that saturation would occur once the dielectric layer became sufficiently thick. From these results, it is apparent that there is a diminishing increase in m once the thickness is about $0.1\lambda_g$. Therefore, a thickness of at least $0.1\lambda_g$ should be used to take full advantage of the miniaturization provided by a given dielectric constant. Obviously, a thicker layer is better in terms of miniaturization if the additional weight and larger profile can be tolerated.

Before proceeding to the case where both sides of the spiral are loaded, it is interesting to observe the impact that the dielectric layer width has on the miniaturization

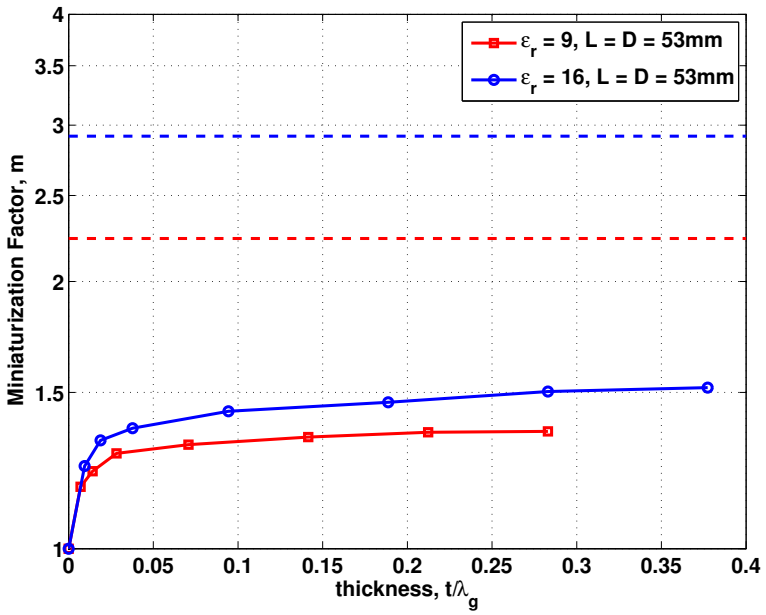

Figure 4.4: Miniaturization factor as a function of the dielectric layer thickness in guided wavelengths λ_g.

factor. Figure 4.5 shows the results obtained by increasing the width of the dielectric layer for a thickness of $0.212\lambda_g$ and a fixed spiral diameter of 53mm. Here, the width of the dielectric layer has been normalized to the spiral diameter. From this figure it is evident that m increases as the width of the dielectric layer exceeds the spiral diameter. Therefore, the width of the dielectric layer has a profound affect on the miniaturization factor. This implies that the results obtained in Fig. 4.4 would be significantly different if the analysis were carried out using a dielectric layer that was infinite in extent. Also, it is important to note that if an antenna design is limited by a maximum dimension d_{max} where $d_{max} > D$, better performance is obtained by increasing the antenna diameter rather than using a smaller diameter antenna and increasing the width of the dielectric layer. That is, increasing m by making the

width of the dielectric layer larger than the antenna ($L/D > 1$) does not result in better performance compared to making both of them larger ($L/D = 1$).

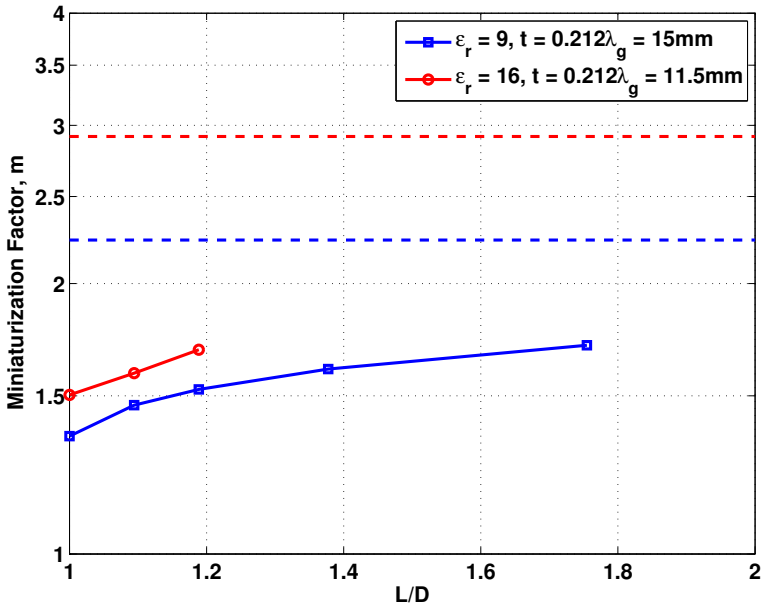

Figure 4.5: Impact of superstrate width on miniaturization.

Now that the loading of one side of the spiral has been considered, it is of interest to examine the possible benefits of loading both sides. Since the MAM increases when both sides of the antenna are loaded, double-sided loading should result in larger m for a given dielectric constant compared to loading a single side. Of course, which approach results in the larger m will depend upon the total thickness of the dielectric material. Therefore, if the total thickness is limited to t, can a larger m be achieved by loading only one side with a dielectric layer of thickness t or by loading both sides with a dielectric layer of thickness $0.5t$? To answer this question both sides of the spiral antenna were loaded using dielectric layers of thickness $0.5t$ and width

$L = D$. The results were then compared to those obtained from loading only a single side with a thickness t. Fig. 4.6 shows the m as a function of the total thickness for single-sided loading and double-sided loading using a dielectric constant of 9. It is observed that for the same total thickness a larger or equivalent m is achieved when both sides of the antenna are loaded. Therefore, it can be concluded that loading both sides of the antenna will always produce the same or more miniaturization for the same total thickness which is an important result. The only potential drawback of loading both sides is that the antenna will radiate equally in both directions. By loading only one side, it is possible to make the antenna radiate more to the side with the dielectric loading[15] [59]. Therefore, loading one side aids in making the antenna uni-directional which is usually required in most applications. However, to achieve sufficient uni-directional radiation, the dielectric layer must be electrically thick [59, 60]. Therefore, the excitation of surface waves or lateral waves becomes an important issue. The excitation of these waves results in pattern distortion and, in general, negatively effects the overall antenna performance. Even if the surface waves can be utilized in a beneficial way, the thickness of the dielectric layer is prohibitive for use in low-profile antenna applications.

4.3.3 Impact of Dielectric Constant

Having already established how the width and thickness of the dielectric layer affect miniaturization, it is time to consider how much miniaturization can be achieved by increasing the dielectric constant. As in the previous section, simulations were used study the effect of the dielectric constant. For each dielectric constant considered, the thickness of the layer was chosen to be $0.1\lambda_g$ and the width was equal to the spiral

[15]For magnetic material loading, the antenna will radiate more to the opposite side

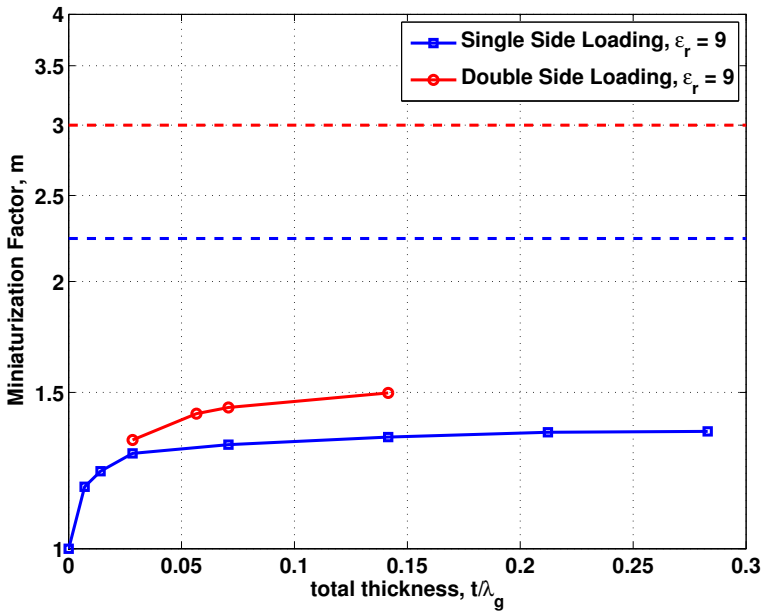

Figure 4.6: Comparison of the miniaturization factor for single-sided and double-sided loading with the same overall antenna thickness.

diameter. The miniaturization factor was then obtained for dielectric constants of 1, 4, 9, 16, 25 and 30. To predict the miniaturization for larger dielectric constants, the simulation results where extended by curve fitting. This approach was used because of the excessive amount of time required to simulate the spiral loaded with higher-contrast layers ($\epsilon_r > 30$).

Figure 4.7 shows the behavior of m as a function of ϵ_r. The solid curve is for the infinite half-space loading case and the other two curves are for the loading of a single side and both sides respectively. Note that for both loading cases the total thickness t of the dielectric layer is $0.1\lambda_g$. From Fig. 4.7 it is evident that the rate at which m increases with increasing ϵ_r begins to diminish for $\epsilon_r > 50$. Also, if only a single side is loaded, it takes an $\epsilon_r = 100$ to achieve a size reduction of a factor of two. However,

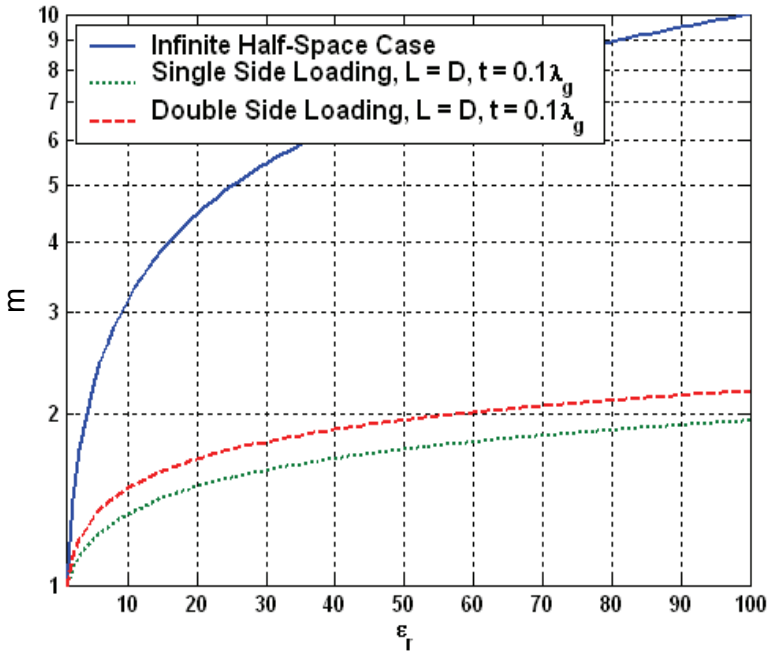

Figure 4.7: Achievable miniaturization for a spiral antenna as a function of dielectric constant (thickness = $0.1\lambda_g$).

a m of two can be achieved using an $\epsilon_r = 60$ if both sides are loaded. In fact, loading both sides usually results in a $7 - 8\%$ increase in m. From these results, it appears that the largest m one can achieve using dielectric loading is around 2.1. Of course, a larger m is possible using thicker dielectric layers but the inevitable weight increase and larger profile is not worth the small increase in m.

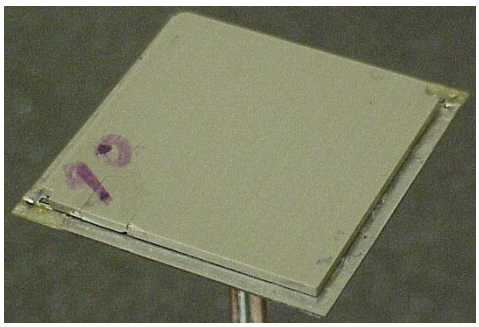

Figure 4.8: Two inch spiral loaded with high-contrast superstrate.

To verify these results, a two inch diameter spiral was loaded with $0.1\lambda_g$ thick dielectric superstrates having ϵ_r =9, 16, 30 and 85 respectively. The superstrates with ϵ_r =9, 16 and 30 are epoxy bonded ceramics ($tan\delta < 0.002$) obtained from Emerson & Cuming Microwave. The ceramic superstrate with $\epsilon_r = 85$ was obtained from picoFarad and was made from rare earth titanate ($tan\delta < 0.001$). The spiral loaded with the $\epsilon_r = 85$ superstrate is shown in Fig. 4.8. The spiral used for the experimental verification has a slot width $w = 0.0762cm$ (30 mils), conductor width $S = 0.2286cm$, aperture dimensions of $5.715x5.715cm$ (2.25"x2.25") and it was printed on a 0.06096cm (24 mils) thick FR4 substrate (ϵ = 4.25-j0.0595). The measured circularly polarized gain is shown in Figure 4.9 and it is evident that the

dielectric loading shifts the realized gain curve to lower frequencies as the dielectric constant increases. Note that, in all cases, the realized gain was measured with respect to an 100Ω source impedance.

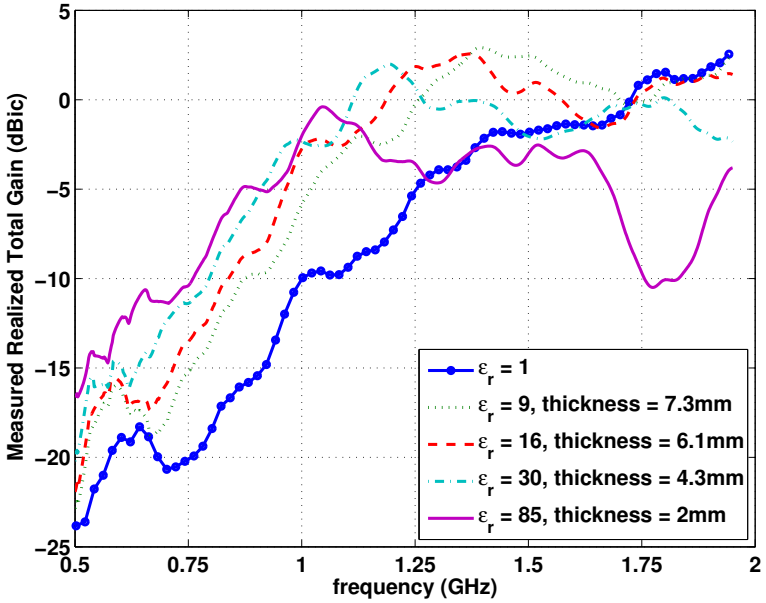

Figure 4.9: Measured boresight gain (realized) for the dielectric loaded 2 spiral.

The measured miniaturization factor (square markers) is shown in Fig. 4.10 in addition to the curve fitted simulation results. Since no attempt was made to improve the matching for each measured case, the measured miniaturization factor was obtained from the realized gain with respect to 100Ω. The simulations results shown in Fig. 4.10 were recalculated with respect to 100Ω and, therefore, are not the same as the results shown in Fig. 4.7. It is apparent from Fig. 4.10 that the agreement between measurement and simulation is very good and validates the simulation results. Also, it is noted that if the impedance were adjusted for each measured case

the resulting m would be larger. For instance, the measurement for the $\epsilon_r = 85$ case resulted in a m of 1.7 whereas the simulation result with optimal matching resulted in a m of about 1.9.

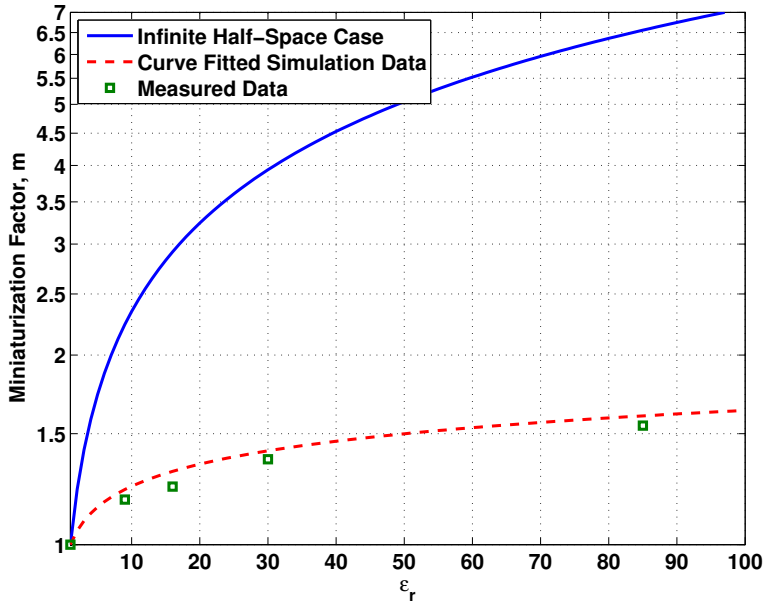

Figure 4.10: Experimental verification of the achievable miniaturization as a function of dielectric constant for single-sided loading (thickness = $0.1\lambda_g$).

4.4 Dielectric Loading Issues

In the previous section, very high-contrast materials ($\epsilon_r = 100$) were needed to achieve large miniaturization factors (around 2). The use of high-contrast materials can have unwanted effects on the antenna performance. The fluctuations in the realized gain shown previously in Fig. 4.9 are an example of this. Furthermore, these effects can become worse the more the antenna is miniaturized. These unwanted effects can occur for two reasons. First of all, the gain fluctuations can be caused

by uniform loading as discussed previously in section 3.4. Secondly, the excitation of surface waves and dielectric resonance modes can produce the observed fluctuations. The excitation of surface waves and resonant modes is dependent upon the electrical thickness of the dielectric layer. As the electrical thickness approaches $0.25\lambda_g$, a significant amount of energy can be lost to the excitation of surface waves. For the frequency range shown in Fig. 4.9, the thickness of dielectric layer in each case is less than $0.15\lambda_g$. Therefore, the observed gain fluctuations are most likely caused by the uniform loading since the dielectric layers are quite thin.

As discussed previously in section 3.4, the effects caused by uniform loading can be addressed by tapering the dielectric loading (either the dielectric constant or thickness) and, to some extent, by reducing the spiral growth rate. Tapering can also be used to minimize the reduction of the antenna input impedance which is caused by dielectric loading (see section 3.4.3). The following section demonstrates this using a simple linear tapering of the dielectric constant. The issue of exciting surface waves and dielectric resonance modes can also be addressed by tapering. This is discussed in section 4.4.2.

4.4.1 Impedance Reduction

A consequence of dielectric loading is a reduction in the input resistance of the antenna. As shown in Figure 4.11, increasing the thickness of the dielectric slab leads to further reduction in the input resistance. In fact, the input resistance asymptotically approaches a value which is equal to the unloaded value divided by the square root of the effective dielectric constant. From this observation it should be expected that loading both sides of the antenna will result in even more reduction because of

the larger effective dielectric constant. From Figure 4.11 it is evident that this does in fact occur when both sides are loaded ($\epsilon_r = 9$). The reduction in the input resistance

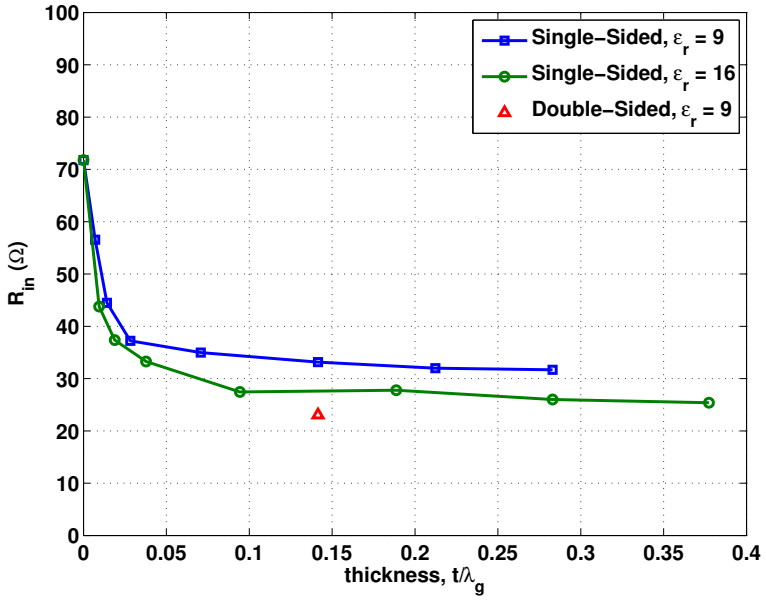

Figure 4.11: Impact of superstrate thickness on input resistance reduction for single-sided loading.

is a problem because it will reduce the mismatch efficiency unless the impedance of the balun or the geometry of the spiral is adjusted accordingly. When the antenna is loaded with a low-contrast material, such adjustments can easily be made. However, when high-contrast material is used, it is far more challenging to match the antenna impedance to the system impedance. Instead of adjusting the impedance of the balun or spiral geometry, the loading can be tapered to minimize impact on the input impedance. This has the additional benefit of eliminating issues associated with uniform loading and the excitation of surface waves.

The dielectric loading can be tapered by using either the dielectric constant or the thickness while the other parameter is fixed. The concept of tapering the loading is to load the low frequency components to achieve the desired miniaturization while minimizing the amount of loading at the higher frequencies where it is not needed. Since the spiral radiates from different regions (radiation bands) depending upon the frequency, the electrical thickness of the dielectric loading should be about $0.1\lambda_g$ at the edge of the spiral aperture (low frequency region) and, ideally, gradually reduce to zero at the center of the spiral (high frequency region). An example of this type of dielectric tapering is shown in Fig. 4.12. In this case, the dielectric constant of the slab has been varied linearly starting with a dielectric constant of 3 at its center and ending with a dielectric constant of 9 in the outer region.

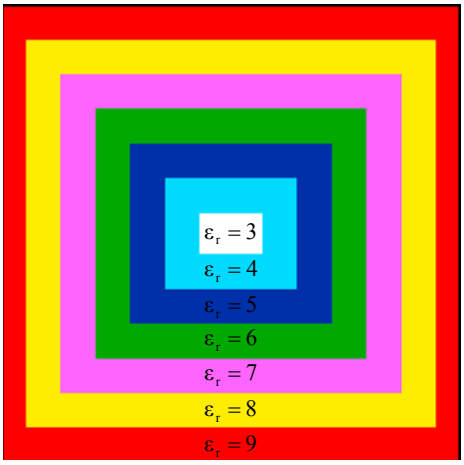

Figure 4.12: Top view of a dielectric slab which has a linear tapering of its dielectric constant.

To illustrate the effect of tapering the dielectric material, the same square spiral was simulated using a uniform dielectric layer with $\epsilon_r = 9$ and the tapered dielectric layer shown in Figure 4.12. For the uniform layer, the input resistance was reduced from 72Ω to 33Ω. However, the tapered dielectric layer was able to limit the reduction to 53Ω which is a significant improvement. With further adjustment of the dielectric constant of each region, it should be possible to maintain the free-space impedance of the antenna. Of course, tapering the dielectric loading is only useful if the same miniaturization can be achieved as in the uniform case. As shown in Fig. 4.13, the realized gain curves for the uniform loading and the tapered loading are almost identical assuming that both are equally well matched. Therefore, it is possible to achieve the same miniaturization using a tapered loading.

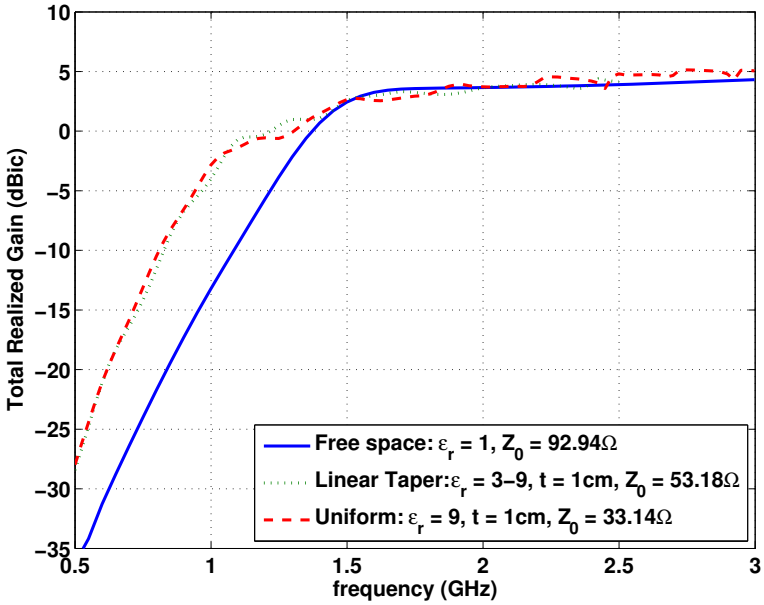

Figure 4.13: Effect of dielectric tapering on the realized gain.

The only issue with tapering the dielectric loading is fabricating it. For instance, the graded dielectric in Fig. 4.12 can be fabricated using a combination of different ceramics or by using polymer-ceramics. Each approach has its advantages and disadvantages. The advantage of using pure ceramic materials is that high-contrast materials ($\epsilon_r = 100$) are readily available and a wide range of dielectric constants are available using different ceramics. The problem with using ceramics is in the process of combining different ceramics to form a graded dielectric layer. The general procedure of creating a ceramic object via sintering of powder is as follows:

- Mixing water, binder, deflocculant, and unfired ceramic powder to form a slurry.
- Putting the dried slurry into a mold and pressing it to form a green body (an unsintered ceramic item).
- Heating the green body at low temperature to burn off the binder.
- Sintering at a high temperature to fuse the ceramic particles together.

Since different ceramics have different thermal expansion coefficients, only ceramics with similar thermal expansion coefficients can be used to make a graded dielectric layer. If the difference between the thermal expansion coefficients of two ceramics was too great, the ceramics after sintering would cool at different rates which, in turn, would create internal stresses that could fracture the ceramic. Therefore, the number of ceramics that can be combined to form a graded dielectric is limited which, in turn, limits the tapering profile.

This issue can be overcome by using a polymer-ceramic. A polymer-ceramic is made by mixing ceramic powder with a polymer base such as silicone in the proper

proportion to obtain the desired dielectric constant (the mixture is "hardened" using a curing agent). Since polymer-ceramics with different dielectric constants contain the same components just in different proportions, they can easily be combined to form a graded dielectric layer. The problem with using polymer-ceramics is that the dielectric constant is limited to about 30 because the polymer based can only contain so much ceramic powder before it becomes saturated. Therefore, the amount of miniaturization that can be achieved is limited.

From a fabrication point of view, the best option is to taper the dielectric loading by varying the thickness of the dielectric. Using this approach, a single high-contrast ceramic can be used which eliminates the need to combine multiple ceramic materials. The proper thickness profile can be obtained by machining the ceramic, preferably in its green body form. If the dielectric constant of the ceramic is greater than 30, this must be done before the ceramic is sintered. Regardless of how the dielectric loading is tapered, fabrication is difficult and a challenging process.

4.4.2 Surface Wave and Resonant Mode Issues

Any reactive boundary or surface tends to guide a wave along that boundary [3]. For instance, a dielectric coated conductor can support guided modes with the lowest mode TM_0 capable of propagating at all frequencies [3]. Which modes can be excited and how much energy can be coupled into them depends upon the electrical thickness of the dielectric layer. For a dielectric coated ground plane, the cutoff frequencies of the modes are given by the following expression

$$f_c = \frac{nc}{4t\sqrt{\epsilon_r \mu_r - 1}}. \tag{4.4}$$

where t is the thickness of the layer, n is the mode number and c is the speed of light in vacuum.

The situation is very similar for an antenna coated with a dielectric or high-contrast material [61]. In this case, the antenna acts as a source of surface waves in the material and the amount of energy lost to the excitation of surface wave depends mainly on the electrical thickness of the material. As the thickness becomes comparable or greater than a quarter wavelength $\left(t \geq \lambda_0 / \left(4\sqrt{\epsilon_r}\right)\right)$, a significant amount of energy is lost to surface waves [61] causing undesired pattern and polarization distortion due to radiation from the truncated dielectric. Since the dielectric body is finite, surface waves can also excite resonant modes which can transform a broadband antenna into a narrow band dielectric resonator antenna (DRA). The frequency for which a resonant mode can exist is determined by the dielectric constant and the geometry of the dielectric body. However, the resonant mode strength is determined by how much energy is contained in the surface wave. Therefore, by suppressing surface waves, dielectric or material resonances can also be suppressed. As mentioned previously, this can be accomplished by tapering the electrical thickness of the material and making sure that the maximum thickness is less than $0.25\lambda_g$.

4.5 Summary

The miniaturization of a spiral antenna using high-contrast materials was examined in this chapter. Only dielectric materials were considered because of the dissipative nature of currently available magnetic materials. Using a previously developed design [49,56,57] as a baseline, the spiral antenna was loaded with finite high-contrast

dielectric layers (substrates and superstrates). The effect of the dielectric layer thickness, width and permittivity on the miniaturization of the spiral antenna was then examined using simulations and measurements. It was shown in section 4.3.2 that, for a given dielectric constant, miniaturization increased with increasing thickness (see Fig. 4.4) and that the point of diminishing return was reached for a thickness around $0.1\lambda_g$ where $\lambda_g = 4D/\sqrt{\epsilon_r}$. Furthermore, for a given thickness, more miniaturization (about 7-8%) could be achieved by loading both sides of the spiral instead of one (see Fig. 4.6). It was also observed that increasing the width of the dielectric layer resulted in more miniaturization. However, it was noted that increasing the spiral diameter and dielectric width concurrently leads to better performance than only increasing the width of the dielectric layer. In section 4.3.3, the maximum amount of miniaturization that could be achieved using dielectric loading was considered by increasing the permittivity of the dielectric layer. Using simulations, it was estimated that a dielectric constant of 100 would result in a miniaturization factor of 2.1 (see Fig. 4.7) which is close to the theoretical limit of three. As with all miniaturization techniques, material loading has its drawbacks. The most notable being the high density of the materials which significantly increase the antenna weight. This is a primary concern for airborne applications which have a limited payload such as small aircraft like unmanned aerial vehicles (UAV). This fact is one of the reasons for exploring the technique of reactive loading in the following chapter.

CHAPTER 5

BROADBAND ANTENNA MINIATURIZATION VIA INDUCTIVE LOADING

5.1 Introduction

Whether an antenna is miniaturized using materials or reactive loading, each approach has its own associated challenges and performance trade-offs. One of the challenges in using dielectric or magnetic materials is maintaining a reasonable antenna weight while achieving the desired miniaturization. This becomes difficult when large miniaturization factors are desired because of the density of high contrast materials and the volume of material needed for miniaturization. As an alternative, reactive loading can be used to achieve similar miniaturization factors while adding a minimal amount of weight to the antenna. Furthermore, with reactive loading, it is possible to inductively load an antenna without using lossy magnetic materials. Here, reactive loading refers to the enhancement of the capacitance and/or inductance of the antenna without resorting to dielectric or magnetic materials. A common example of capacitive loading is the top loaded monopole [9] and the normal mode helix and the meander line antenna are two common examples of inductive loading [10, 11]. The main issue with reactive loading is its implementation and integration into the

antenna. For some antennas, it can be difficult if not impossible to implement capacitive and/or inductive loading. For the spiral antenna, capacitive loading is difficult to realize without using dielectric materials. However, the spiral is well suited for inductive loading.

In this chapter, the inductive loading of the spiral antenna is presented. As in the previous chapter, the goal is to see how much the spiral can be miniaturized without sacrificing its performance at higher frequencies. The following section discusses various ways to inductively load the spiral antenna. It is found that a novel volumetric approach results in greater miniaturization than the more traditional two dimensional approaches such as planar meandering. The volumetric approach involves coiling the spiral arm such that it resembles a helix (see Figure 5.4). The design of coiled structure is the focus of section 5.3. In this section, the main topics of discussion are the selection of the optimal taper profile and length. In section 5.4 and 5.5, the inductive loading approach is validated through the design, fabrication and measurement of a 6" (UHF operation) and 18" (VHF and UHF operation) diameter spiral antennas.

5.2 Implementation of Inductive Loading for the Spiral Antenna

For the spiral antenna, increasing the self-inductance of the spiral arm via inductive loading can be achieved in a variety of ways. One option is to use small surface mount chip inductors to increase the inductance per unit length of the spiral arms [62]. This technique works in theory if the chip inductors are low-loss and the spacing between them is small with respect to the effective guided wavelength. Nevertheless, in practice, the internal resistance of each chip and soldering introduces significant ohmic loss which makes this approach unattractive. Another option is to modify the

spiral arms using either a zigzag, sinuous or meander-line modulation. The following section will discuss the commonly used technique of planar or two-dimensional (2D) meandering and its limitations. Subsequently, section 5.2.2 presents a novel volumetric approach that inductively loads the spiral arms by coiling each arm such that it resembles a helical waveguide. It is shown that this approach can provide a significant improvement over meandering.

5.2.1 2-D Inductive Loading: Planar Meandering

A common way to implement inductive loading is through the use of meandering. Fig. 5.1 shows this approach applied to a 6 inch diameter log-spiral antenna. Here, the wire spiral arm has been meandered using a constant spacing or pitch of 120 mils but variable width. The width is varied linearly from 22 to 275 mils to create a smooth transition from the untreated (non-meandered) portion to the inductively loaded section of the spiral arm. The width is bounded by the log-spiral curves which define the edges of the spiral arm as illustrated in Fig. 5.2. The equations for the curves are as follows

$$r = r_0 e^{a\phi} \qquad \text{and} \qquad r = r_0 e^{a(\phi+\delta)} \tag{5.1}$$

where r_0 is the initial radius, a is the growth rate ($\tau = e^{-2\pi|a|}$) and the angle δ controls the width of the arm ($\delta = \pi/2$ is self-complementary structure). Note that all of the spirals in this section have the following parameters: $r_0 = 0.5cm$, $a = 0.602$ ($\tau = 0.685$) and $\delta = 0.5\pi$.

Increasing the inductance of the spiral arm in this manner is quite effective in miniaturizing the spiral as shown in Fig. 5.3. Here, the total realized gain of the meandered spiral (pitch = 60 mils) is compared to a traditional wire spiral of the

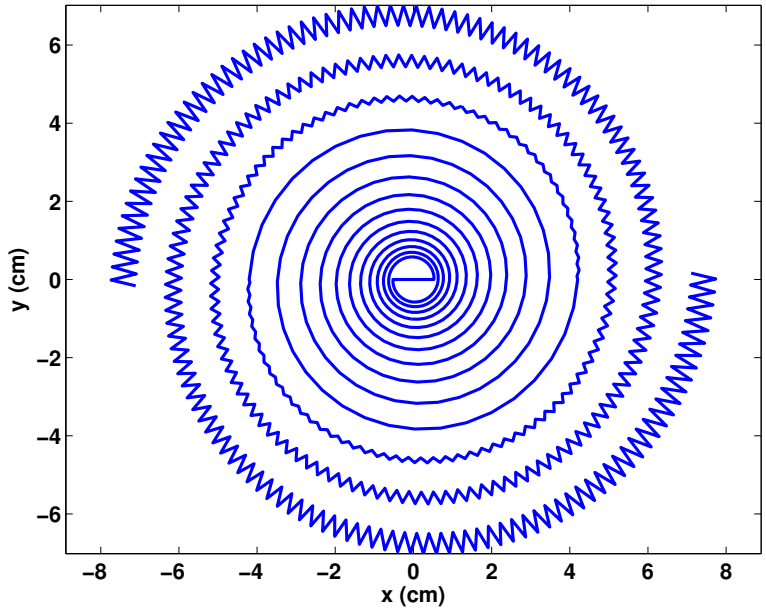

Figure 5.1: Inductive loading of a 6 inch diameter spiral antenna using planar meandering (zig-zag).

same size. Note that the planar meandered spiral achieves a miniaturization factor of about 1.5 (based on -15 dBi point). The results were obtained using the numerical electromagnetic code (NEC-2) [50] which is based on the method of moments. While implementing inductive loading in this manner is simple and easy to fabricate, its ability to miniaturize the spiral is limited. To demonstrate this, the pitch of the meandered spiral is reduce by half in an attempt to further increase the self-inductance of the spiral arm and further miniaturize it. However, from Fig. 5.3 it is apparent that decreasing the pitch by a factor of 2 had a negligible affect on the realized gain.

The limitation of meandering can be readily illustrated by considering a 2-D meandered dipole that occupies a fixed area. For a wire dipole, meandering is used to reduce its resonant frequency by increasing the self-inductance of the wire [10, 63].

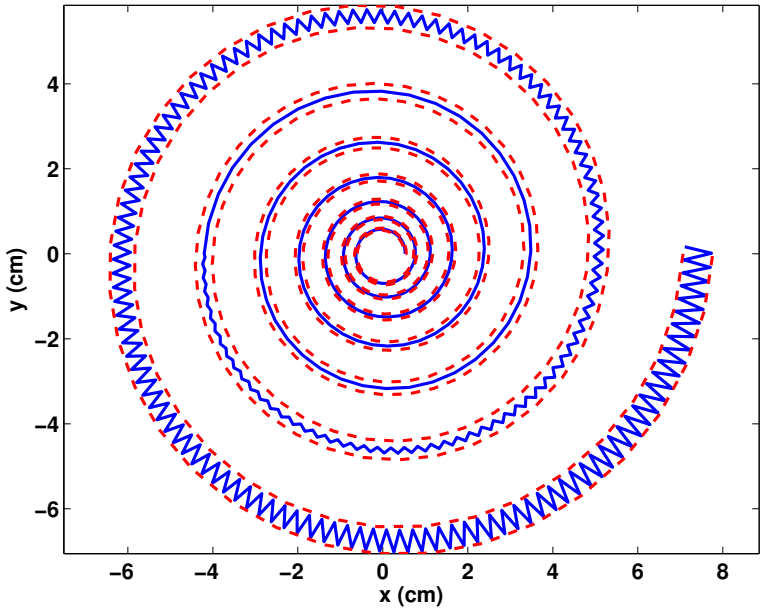

Figure 5.2: Illustration of planar meandered spiral (single arm) with log-spiral bounding curves.

The self-inductance of the wire can be increased arbitrarily by increasing the number of meander sections (smaller pitch). However, as more meander sections are used, the self-capacitance of the wire also begins to increase and counteract the increase in the self-inductance [10]. As the self-capacitance increases, the reduction in the resonant frequency begins to diminish and, when the self-capacitance becomes large enough, the resonant frequency will begin to increase. Therefore, for a fixed area, the resonant frequency can only be reduced to a certain extent using meandering and it is important to note that this is independent of the meander shape (rectangular, zig-zag, etc.). Since planar meandering can not even achieve as much miniaturization as dielectric loading, another approach for implementing inductive loading is needed if one desires to miniaturize the antenna further via inductive loading. In the following

section, it is shown that the volumetric approach can be used to further miniaturize the spiral.

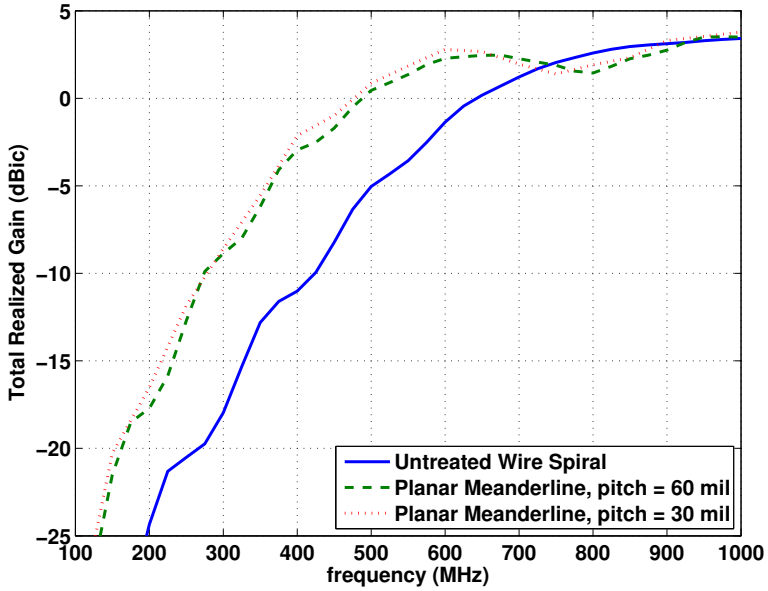

Figure 5.3: Demonstration of the limitations of planar meandering for use in miniaturizing a spiral antenna.

5.2.2 3-D Inductive Loading: Coiling

The concept of volumetric inductive loading is to use a volume of space instead of a 2D surface to implement the inductive loading. By exploiting all three dimensions, it should be possible to achieve a larger inductance than using planar meandering. For the spiral, this approach involves coiling the spiral arm such that it resembles a helix as shown in Figure 5.4. The coil for this spiral has a rectangular cross section which allows control of the inductance using the pitch (separation between turns), width and thickness of the coil as depicted in Figure 5.4. These parameters can be

related to the inductance of the coil using the equivalent inductance per unit-length of a lossless helical waveguide, derived previously in [64] for a circular helical waveguide. From [64], the inductance per unit length is given by

$$L_e = \frac{\mu_0}{2\pi}\left(\frac{2\pi a}{p}\right)^2 I_1(\gamma a)\, K_1(\gamma a) \quad \text{henrys/meter} \tag{5.2}$$

where a is the coil radius, p is the pitch, I is the modified Bessel function of the first kind and K is the modified Bessel function of the second kind. The variable γ is determined from the following dispersion equation

$$\gamma^2 = k^2\left(\frac{2\pi a}{p}\right)^2 \frac{I_1(\gamma a)\, K_1(\gamma a)}{I_0(\gamma a)\, K_0(\gamma a)} \tag{5.3}$$

where k is the free space propagation constant. From equation 5.2, it is clear that the inductance per unit length is linearly proportional to the cross sectional area and inversely proportional to the pitch squared. This equation provides an important physical insight into how the coil inductance can be controlled by modifying its geometry which is discussed in later sections.

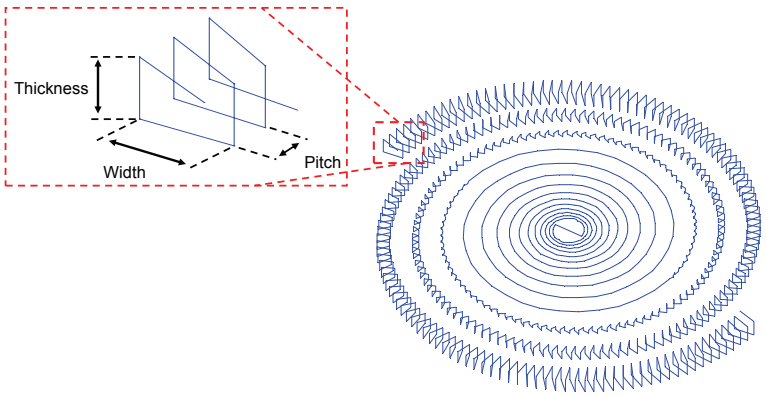

Figure 5.4: A 6 inch spiral antenna with coiled arms.

To demonstrate the advantage of the volumetric approach, the spiral arm is coiled using the same points which define the previous meandered spiral (pitch=60mils). That is, the coil pitch is a constant 60 mils and the width varies linearly from 22 to 275 mils. The thickness of the coil was chosen to be a constant 250 mils. Figure 5.5 shows a comparison of the realized gain between the meandered spiral and the coiled spiral. For each case, the impedance used to calculate the realized gain is different and was chosen to minimize the mismatch loss. It is clear from Figure 5.5 that the volumetric design has significantly higher gain below 300 MHz than the 2D meandered spiral. In fact, the -15 dBi gain point was shifted from 320 MHz (untreated wire spiral) to 147 MHz which corresponds to a miniaturization factor of 2.18. This clearly demonstrates the potential of the volumetric loading approach for miniaturizing the spiral.

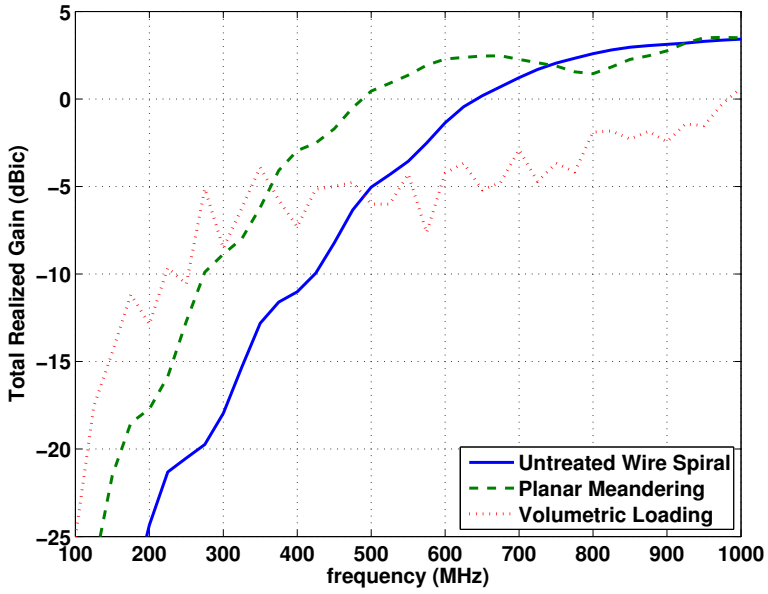

Figure 5.5: Comparison of the miniaturization potential for planar meandering and volumetric coiling.

One issue with the coiled spiral shown in Fig. 5.5 is the lower realized gain at higher frequencies. For this case, the lower gain is a result of a poor design. That is, the initial inductance of the coil is too large and the taper profile is not optimal. By improving the coil design better performance can be achieved as shown in Fig. 5.6. Here, the previous coil design (constant thickness) is compared to an improved coil design referred to as the conical coil design. The conical coil design has the same coil pitch and width as the previous design but its thickness has been linearly tapered from 20 to 250 mils. The tapering of the thickness leads to a more gradual transition from the unloaded region to the loaded region (coiled section). Consequently, the realized gain has improved significantly at the higher frequencies. Therefore, proper design of the coil structure is important for achieving the best overall performance. The following section discusses the optimization of the coil design in regards to the taper profile and taper length.

5.3 3-D Inductive Loading Taper Design

Just like a transmission line, increasing the self inductance (series) of the spiral arm not only decreases the phase velocity but also increases the characteristic impedance. Therefore, the impedance seen by the wave propagating along the coiled spiral arm can be significantly larger than the impedance seen propagating along an uncoiled section of the spiral arm. Consequently, it is necessary to taper the inductive loading to avoid any substantial impedance discontinuities which might occur and negatively affect the input impedance. Large impedance discontinuities can be avoided as long as the change in impedance from one section of the spiral arm to the next is small. Based on the theory of small reflections, reflections caused by an

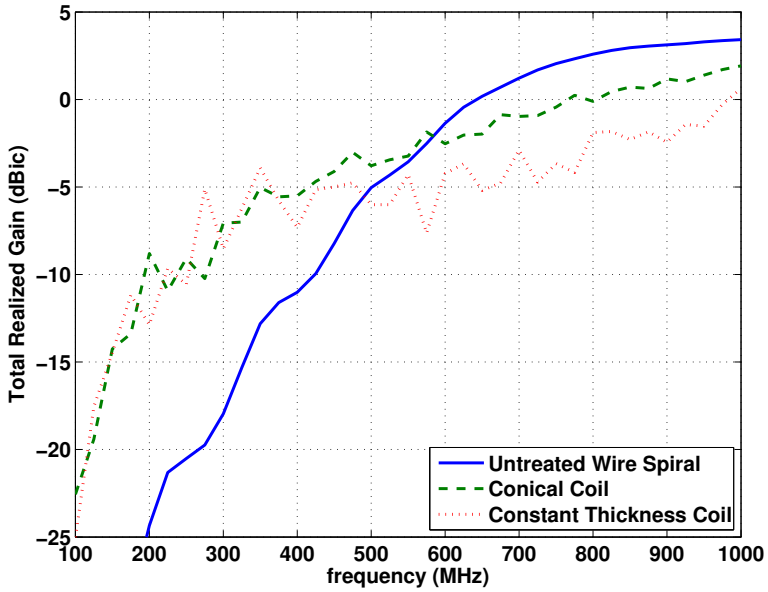

Figure 5.6: Comparison of the miniaturization potential for planar meandering and volumetric coiling.

incremental change in impedance will also be small implying minimal impact on the antenna input impedance.

In theory, it is possible to suppress reflections that may occur from the inductive loading using capacitive (dielectric) loading to counter the impedance increase. That is, by using both inductive and capacitive loading, it is possible to maintain the same impedance throughout the entire spiral structure as discussed previously in section 3.4.3. Therefore, the tapering of the inductive loading is not as crucial. A way to achieve this is to embed the coiled section of the spiral arm in a dielectric material which has an graded dielectric constant. Ideally, the dielectric constant would be graded along the length of the coil to match the spatial variation in the inductance and it would vary with frequency to match the frequency variation. Obviously, engineering

such a dielectric substrate would be very challenging from both a theoretical and practical point of view. While such a substrate has its benefits, it unnecessarily complicates the overall design. Therefore, the inclusion of dielectric material for the prototype discussed in this chapter is mainly for structural support only (see section 5.4.2).

Designing the coil structure for loading the spiral antenna is, in many aspects, similar to designing a continuously tapered transmission line matching section. Both involve the design of a taper profile which provides a gradual transition from an initial impedance Z_0 to a final impedance Z_L over a given length L. For the ideal tapered transmission line problem, the transmission line is loss-less and the impedance is only a function of position [37]. This is not the case for the coiled structure. First of all, the coil inductance is frequency dependent (see equation 5.2) in addition to be being a function of position. Secondly, radiation from the spiral introduces loss into the problem that is both position dependent and frequency dependent. As a result, designing the taper for the inductive loading of the spiral is a more complicated problem. Therefore, design guidelines for tapered transmission lines are used only as a starting point in designing the taper.

The remainder of this section discusses the design of the taper profile. The goal is to establish some general guidelines for selecting the taper shape and taper length. These guidelines can then be used as a starting point in the antenna design process. The following section discusses the selection of the optimal taper profile using a Genetic algorithm. It is found that an exponential profile provides the best overall performance for the spiral. Using the exponential profile, section 5.3.2 examines the

impact of the taper length. From these results it is observed that the taper should be around one λ_0 in length ($\lambda_0 = \pi D$).

5.3.1 Optimal Taper Profile

In this section, a formal optimization using a genetic algorithm is used to determine the optimal inductive loading profile with respect to the realized gain. The goal is to determine the taper profile that maximizes the realized gain over the frequency spectrum where $ka < 1$. In other words, the goal is to miniaturize the spiral as much as possible without sacrificing its realized gain at higher frequencies (close to $ka = 1$).

The first step in conducting a formal optimization is to determine what variables to optimize. A logical choice would be to use the parameters that define the geometry of the coil (thickness, width and pitch) since they are directly related to the inductance of the coil. However, there are multiple parameter combinations that can produce the same inductance. Therefore, there cannot be a unique solution if the actual coil geometry is optimized. In addition, optimizing the physical coil geometry would require a significant amount of simulation time due to the number of wires needed to model the coil. This makes a formal optimization of the coil geometry highly impractical. As an alternative, the optimization does not need to take into account the actual physical geometry of the coil since only the inductance at each point on the spiral arm is of interest. Using a Method of Moments simulation tool such as the NEC, it is possible to assign a distributed series inductance to each wire segment that forms the spiral arm. Therefore, the optimal inductive profile can be determined by optimizing the inductance of each segment that forms a typical wire spiral (see Fig. 5.7). The main advantage of this approach is that a unique solution is possible

and it significantly reduces simulation time making formal optimization both possible and practical.

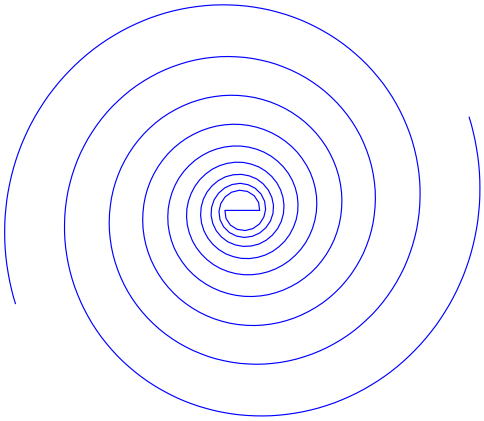

Figure 5.7: 6 inch diameter log-spiral used in the GA optimization of the optimal taper profile ($\delta = \pi/2$, growth rate = 0.0923 or $\tau = 0.56$).

One potential problem with this approach is that the number of variables to be optimized is equal to the number of wire segments that form the spiral arm. Since a typical spiral arm requires at least several hundred segments, the number of variables can be over whelming making the optimization time consuming. This problem can be solved by using a function to present the inductance along the length of the spiral arm. That is, an N^{th} order polynomial could be used to represent the inductance distribution along the spiral arm. The inductance for each wire segment can then be found by sampling this function at the appropriate location. Using this approach, only N+1 variables are needed (one for each coefficient) instead of hundreds. Therefore, a polynomial was used to represent the inductance profile along the spiral arm. The order of the polynomial was determined based upon how accurately it could represent

the basic tapering profiles such as linear, exponential, triangular and Klopfenstein (infinite stage Chebychev). A Matlab program was written to compute the before mentioned tapering profiles for a given taper length (spiral arm length), starting and ending value which were allowed to vary from 0 μ H/m to 100 μ H/m. These taper profiles were then curve fitted using different order polynomials. It was found that at least a 5^{th} order polynomial was needed to accurately represent all of the tapering profiles. It is noted that all of the following optimization results were obtained using a 6^{th} order polynomial.

Since the goal of this optimization is to find the inductive loading profile that maximizes the realized gain over a specific frequency range, the objective function was defined as follows

$$g = max\left(\int_{f_1}^{f_2} G_{realized} df\right) = max\left(\int_{f_1}^{f_2} \left(eD\left(1-|\Gamma|^2\right)\right) df\right) \tag{5.4}$$

where e is the antenna efficiency (assumed to be 1), D is the directivity and $1-|\Gamma|^2$ is the mismatch efficiency. The mismatch efficiency is given by

$$1-|\Gamma|^2 = 1-\left|\frac{Z_A - Z_0^*}{Z_A + Z_0}\right|^2 \tag{5.5}$$

where Z_0 is the impedance of the matching network and Z_A is the antenna input impedance. From equation 5.4 it appears that maximizing the realized gain involves simultaneously maximizing the directivity and mismatch efficiency. However, since the antenna is electrically small over the region of interest, the directivity does not vary significantly. Therefore, the mismatch efficiency is the most important quantity.

In order to maximize the mismatch efficiency, the impedance of the matching network needs to be chosen such that the following expression is maximized

$$max\left(\int_{f_1}^{f_2} \left(\left(1-|\Gamma|^2\right)\right) df\right) \tag{5.6}$$

To find the Z_0 that maximizes 5.6, it is restricted to being purely real and constant. Imposing this restriction on Z_0, the Matlab function "fminbnd" was used to find Z_0 over a fixed interval ($Z_1 < Z_0 < Z_2$). This function is able to find the minimum (or maximum) of single-variable function on fixed interval using golden section search and parabolic interpolation [65, 66].

At this point, it is important to comment on the similarities between this optimization problem and Fano's solution to the impedance matching problem discussed in chapter 2. Recall that Fano developed a method for determining the optimal matching network that maximized the "matching area" for a given load impedance and maximum tolerable pass-band reflection coefficient. That is, he determined the matching network that could achieve the maximum tolerable pass-band reflection coefficient over the largest frequency range. He did this by maximizing a particular function of the reflection coefficient over a frequency interval that depended upon the desired frequency response (low-pass, high-pass or band-pass). This is very similar to the optimization problem at hand in that the objective is to determine the loading profile that maximizes the mismatch efficiency, which is a function of the reflection coefficient, over a given frequency range. Consequently, the inductive loading profile is analogous to the external matching network in Fano's problem and the unloaded spiral input impedance is analogous to the load impedance. However, the load impedance in Fano's problem is actually the input impedance of the inductively loaded spiral. Furthermore, the reactive matching network does not exist because, in the optimization, Z_0 is restricted to being purely real and constant. Therefore, Fano's method is directly applicable unless the input impedance of the inductively loaded spiral can be decomposed into a component based on the inductive loading

and a component based on the unloaded spiral input impedance. It is not known whether such a decomposition is physically possible.

Before proceeding with the optimization, the parameters used to setup the Matlab genetic algorithm are discussed. The first step in setting up the GA is to define the various input parameters such as population type, population size, number of generations, etc. For the optimization, the polynomial coefficients or genes were encoded using real variables not binary. In addition, the population size was 20, 100 generations were used, stall generations was set to 50 (stall time was disable) and the crossover fraction was determined on a case by case basis in order to obtain the best fitness value. To initialize the GA, half of the initial population was specified using uniform, linear, triangular, exponential and Klopfenstein taper profiles (2 of each). The other half was created using the Matlab function gacreationuniform. This function creates a random population with a uniform distribution using an initial range provided by the user. Note that the initial range does not constrain the overall optimization process although it can effect the diversity of the initial population [67]. It only places constraints on the initial population and it is only used one time to generate members for the initial population. It is remarked that the only constraint placed on the population members is that the polynomial created by them cannot produce negative values for the inductance at any point along the length of the spiral arm. After the initial population is defined they are scored based on the fitness function discussed in the previous section. The parents for the next generation are then selected after the fitness scores were scaled to a range suitable for the selection function. Rank scaling was used to scale the raw scores based on the rank of each individual instead of its score which removes the spreading effect of the raw scores [67]. Parents are then

selected using a stochastic uniform selection which helps keep the diversity of the population large, preventing premature convergence on poor solutions [67]. The next generation was formed using two elite children (individuals in the current generation with the best fitness values) and a combination of crossover children (combining genes of a pair of parents) and mutation children (random changes or mutation of single parent). The number of crossover and mutation children depends on the crossover fraction which was determined on a case by case basis in order to obtain the best fitness value. Crossover children were obtained by creating a random binary vector that was used to randomly select genes from the parents (scattered crossover). Mutation children were obtained by adding a random number chosen from a Gaussian distribution, to each entry of the parent vector.

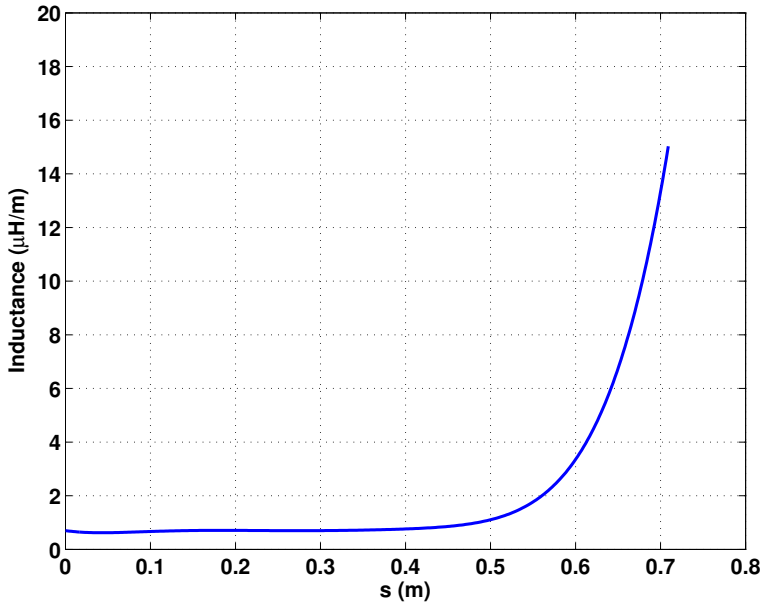

Figure 5.8: Inductive profile obtained by maximizing realized gain from 100 to 1200 MHz.

To begin the optimization of the taper profile, consider the 6" diameter spiral shown in Fig. 5.7 (growth rate = 0.0923, $\delta = \pi/2$). The entire spiral was inductively loaded by assigning each wire segment an distributed series inductance. The inductance of each segment was then determined by maximizing the realized gain from 100 to 1200 MHz using the GA. The profile of the inductance obtained from the optimization is shown in Fig. 5.8 where the inductance is plotted as a function of the distance s from the beginning of the arm. It is apparent that the inductive loading is almost a constant 0.6 $\mu H/m$ for $s < 0.5m$ which corresponds to frequencies greater than 900 MHz. For $s > 0.5m$, the inductance increases almost exponentially to load the low frequency region. To demonstrate this, the section of the inductive profile for $s > 0.5m$ was curve fitted using a triangular, Klopfenstein and exponential profile (see Fig. 5.9) [37]. It is evident from Fig. 5.9 that the optimal taper profile closely resembles an exponential taper in this region.

The realized gain curve produced by this loading profile is shown in Fig. 5.10. It is evident that the realized gain has been improved at low frequency without any significant deterioration at higher frequencies. However, the improvement at lower frequencies is not as impressive as what was previously shown for the coiled spiral. This can be attributed to the fact that the inductance of the coil is frequency dependent (see equation 5.2) whereas in the optimization the inductance is constant with respect to frequency. For the coiled spiral, the inductance of the coil actually increases as the frequency decreases. This occurs because, as the frequency decreases, the electrical spacing between the turns becomes smaller which results in less flux leakage. Naturally, this leads to a larger inductance and, in turn, more miniaturization. Because of this, the actual inductance values obtained from the GA optimization are

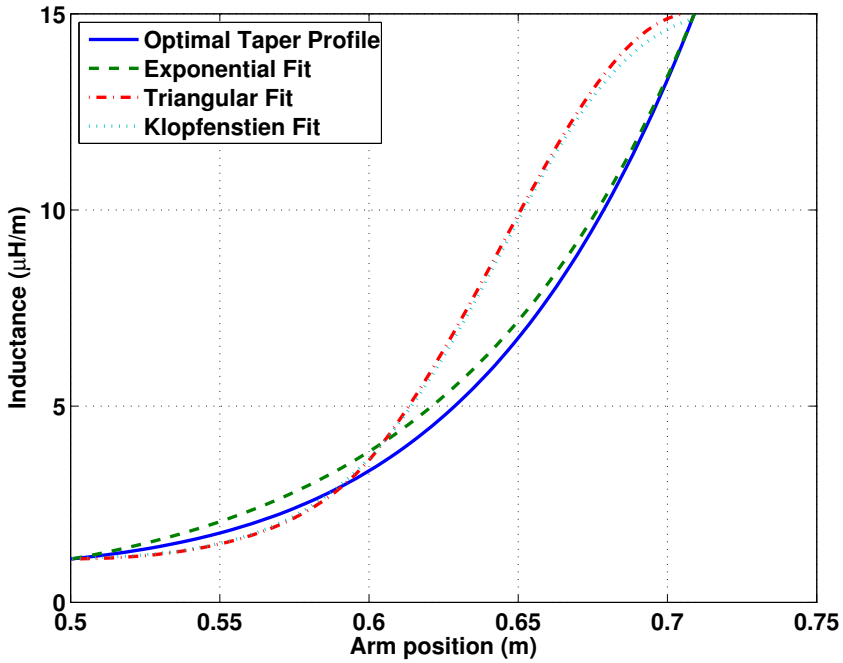

Figure 5.9: Comparison of optimal taper profile to an exponential, triangular and Klopfenstein taper.

not necessarily optimal but the shape of the taper profile is. Therefore, the taper profile obtained by the GA optimization should be used as a guideline for designing the coiled spiral.

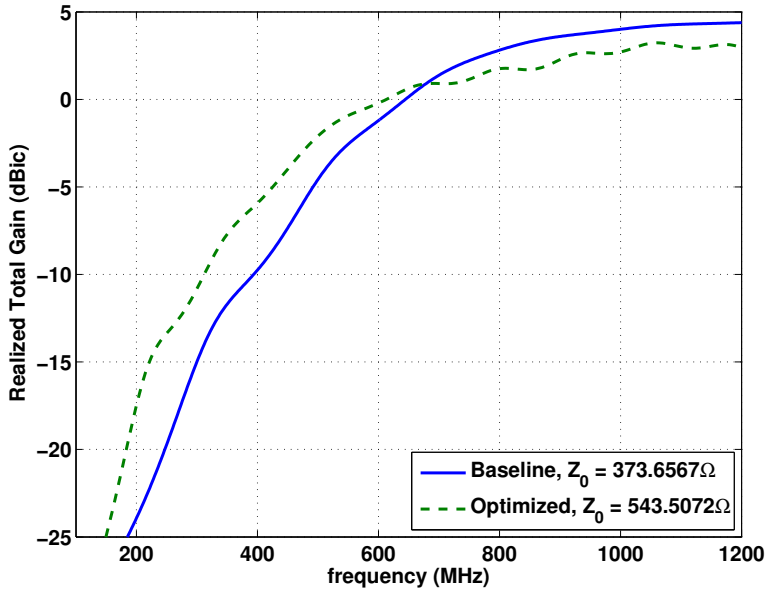

Figure 5.10: Impact of maximizing realized gain from 100 to 1200 MHz on high frequency gain.

5.3.2 Optimal Taper Length

In the previous section, the entire spiral was inductively loaded to find the optimal taper profile (see Fig. 5.8) which was exponential in shape over the outer portion of the spiral. Over the remainder of the spiral the taper profile was a constant 0.6 $\mu H/m$ which, from Fig. 3.4, corresponds to a reduction in phase velocity by only a factor of 1.15. Therefore, the inductive loading in this region (high frequency region) is insignificant implying that the entire spiral does not need to be loaded. Thus, the

purpose of this section is to establish a guideline that can be used to determine the minimum taper length.

From Fig. 5.8, it is evident that the majority of the loading occurs over the outer section of the spiral arm. The length of this region measured from the end of the arm is denoted by the variable L_{taper}. In general, L_{taper} can be defined in terms of three parameters as follows

$$L_{taper} = \int_{\phi_{start}}^{\phi_{max}} r_0 e^{a\phi} d\phi = \frac{r_0}{a}\left(e^{a\phi_{max}} - e^{a\phi_{start}}\right) = \frac{1}{a}\left(r_{max} - r_{start}\right). \tag{5.7}$$

where a is the growth rate, r_{max} is the maximum radius and r_{start} is the radius where the loading begins. Note that r_{start} also determines which frequency components will be inductively loaded. That is, all frequency components whose radiation bands have a radius larger than r_{start} will be inductively loaded. Since the size of the spiral is fixed, the taper length can only be varied in one of two ways. First, for a fixed growth rate, the taper length can be varied by adjusting its starting position r_{start}. To make the taper longer, r_{start} needs to be made smaller which, in turn, leads to the loading of more high frequency components. From the discussion in section 3.4.2, loading the high frequency components has a negative affect on the performance and should be avoided as much as possible. Therefore, this needs to be taken into consideration if the taper length is adjusted in this manner. The second way to adjust the taper length for a fixed r_{start} is by varying the growth rate. In this case, the taper length can be increased by decreasing the growth rate without loading additional high frequency components. However, if the growth rate is too small there will not be sufficient space to coil the spiral arm.

Both approaches for adjusting the taper length are considered in determining the minimum taper length. In all cases, a 6" diameter spiral was inductively loaded using

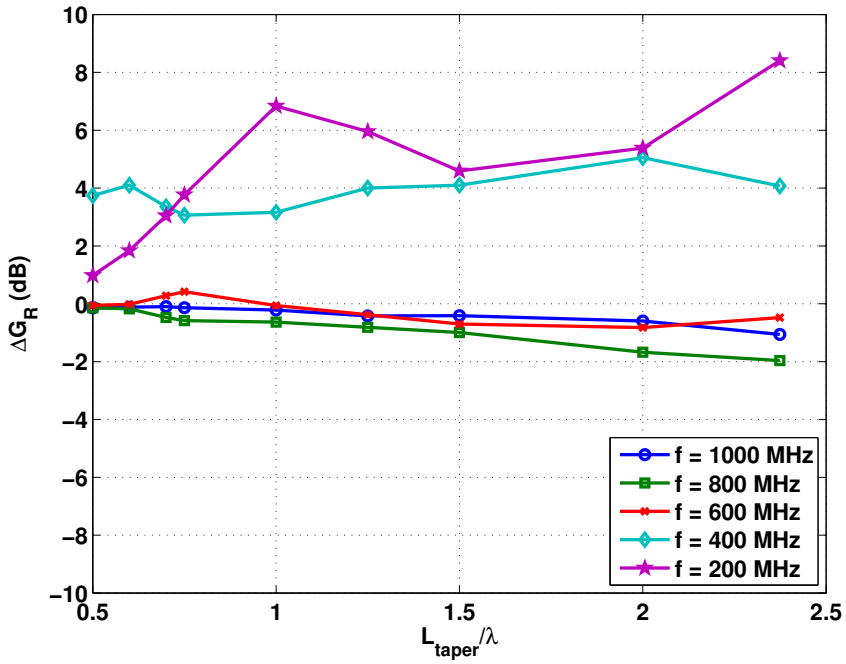

Figure 5.11: Impact of taper length on the realized gain at specific frequency points (taper length is varied by changing the starting radius).

an exponential taper ($0.001\mu H/m$ to $35\mu H/m$) by assigning the proper wire segments a corresponding distributed series inductance as before. The starting value for the taper was chosen to be as small as possible to minimize the impedance discontinuity at the junction of the unloaded and loaded region. The ending inductance was chosen based on the calculation (see equations 5.2 and 5.3) of the maximum inductance achieved by the conical coil design at 150 MHz (frequency of -15 dBi gain point). Also, in each case the taper length was normalized to a reference wavelength λ_0 which is defined as $\lambda_0 = 2\pi r_{max}$. To evaluate the effectiveness of each taper length, the difference in the realized gain ΔG_R between the unloaded and loaded spiral was calculated at five distinct frequency points which are 200, 400, 600, 800 and 1000 MHz. The realized gain difference was then plotted as a function of the taper length in wavelengths.

To begin, the taper length was varied by adjusting r_{start} for a fixed growth rate $a = 0.0595$. The radius r_{start} was varied from 2.44 inches ($f_{start} = 770MHz$) to 0.2 inches ($f_{start} = 9.5GHz$) to obtain taper lengths ranging from $0.5\lambda_0$ to $2.38\lambda_0$. The variation in the realized gain is shown in Fig. 5.12 as a function of the taper length where each curve is for a different frequency point. From these results two trends emerge. In general, for the low frequency points (f = 200 & 400 MHz), the longer the taper the more the gain improves. However, for the higher frequencies the realized gain decreases as much as 2 dB as the taper length increases. The best compromise between the two trends occurs when the taper length is in the range of 1 to 1.5 wavelengths. Therefore, from these results, the taper length should be at least one wavelength but no more than 1.5 wavelengths to achieve the best overall performance.

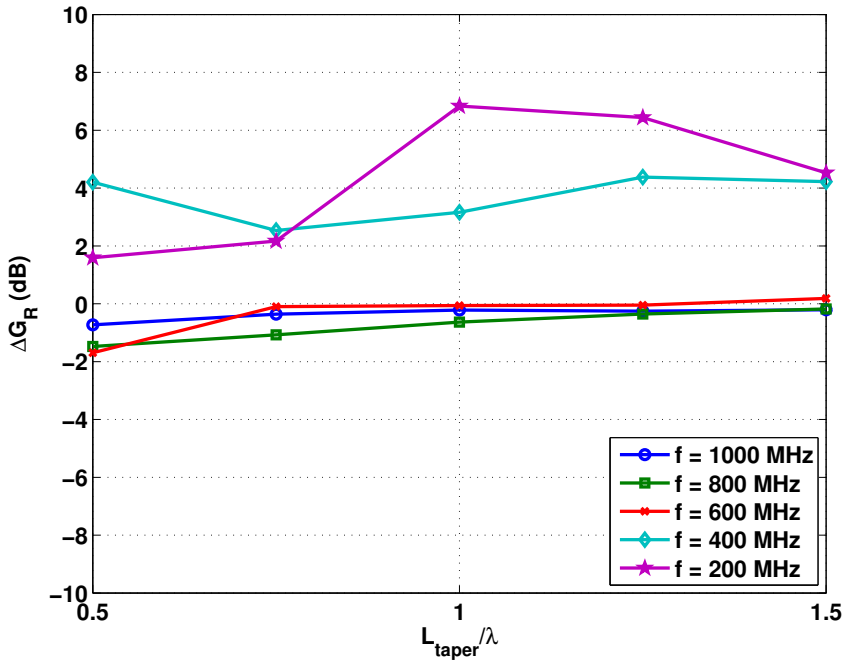

Figure 5.12: Impact of taper length on the realized gain at specific frequency points (taper length is varied by changing the growth rate).

For the other approach, the taper length was adjusted by varying the growth rate from 0.03967 to 0.11899 with a fixed r_{start} of 1.8785in ($f_{start} = 1GHz$). The results are shown in Fig. 5.11 and the trend for the low frequency components is the same as before. However, for the higher frequencies the gain does not decrease as the taper length increases because r_{start} is fixed. Therefore, the taper length can be as large as desired as long as the growth rate does not become so small that there is not sufficient space to coil the spiral arm. For instance, a taper length of $1.5\lambda_0$ corresponds to a growth rate of 0.03967 which produces the spiral shown in Fig. 5.13. Obviously, the space between adjacent arms in the outer portion is rather limited which makes coiling the spiral arm problematic. Therefore, as a guideline, the growth rate should be greater than 0.04 to provide adequate space for coiling the arm. Consequently, this restricts the maximum length of the taper unless r_{start} is changed. In regards to the minimum taper length, it should be about $1\lambda_0$ to achieve the best overall performance which agrees with the previous result (see Fig. 5.11).

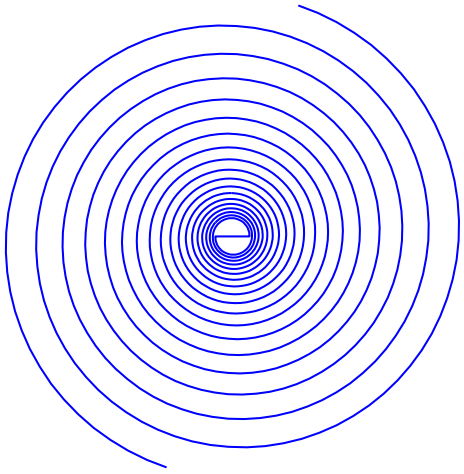

Figure 5.13: A 6" diameter circular log-spiral with a growth rate of 0.03967 ($\delta = 0.5\pi$).

To summarize, the minimum taper length should be about $1\lambda_0$ where $\lambda_0 = 2\pi r_{max}$. The growth rate should be greater than 0.04 to provide enough space to coil the spiral arm. Based on these constraints, r_{start} should be chosen to minimize the loading of the high frequency components. In the following sections, these guidelines are used to design a 6" diameter spiral for UHF operation and a 18" diameter spiral for VHF and UHF operation.

5.4 6" Spiral Design for UHF Operation

In this section, the guideline established in the previous section are used to design a 6" diameter spiral that covers the entire UHF band and as much of the VHF band as possible. The first step in designing the spiral was deciding which of the geometrical coil parameters to use in implementing the exponential taper profile. This decision is important because the choice of parameters dictates the method of fabrication which, in turn, limits the coil design for practical reasons. For instance, standard printed circuit board (PCB) fabrication techniques can readily be used to fabricate the antenna if the coil thickness is constant[16]. If PCB fabrication is used, only the pitch and width can be varied to taper the coil inductance. However, this is not a limitation because numerous taper profiles can be realized using only the pitch and width. The main limitation of PCB fabrication is the antenna diameter is limited to about 19 inches and the thickness to about 0.35 inches. These limitations can be overcome using wire forming techniques. In theory, wire forming techniques can be used to fabricate a coiled spiral design of any size and any taper profile.

[16]Technically, it is possible using multiple layers to fabricate a design with a variable coil thickness using standard PCB techniques. However, to do so, many fabrication issues would have to be overcome.

However, in practice the type of taper profiles that can be realized are limited to linear variations in the pitch, width and thickness. That is, creating an exponential taper by exponentially varying the pitch is difficult using wire forming techniques.

In light of these facts, the 6" diameter spiral was design with PCB fabrication in mind. However, for the 18" diameter spiral presented in section 5.5 wire forming techniques were used to construct the coil for a variety of reasons discussed in section 5.5. In the remainder of this section the design and fabrication of the 6" diameter spiral is discussed. The following section discusses the selection and optimization of the coil parameters to achieve the best overall performance in terms of the realized gain. The analysis is carried out using simulations (NEC) to evaluate the performance of the antenna in free space. The design is then validated in section 5.4.2 which discusses fabrication and measurement results.

5.4.1 Selection and Optimization of Coil Parameters

In designing an inductively loaded spiral there are many parameters that need to be selected and optimized. These parameters can be divided into two categories which relate to the spiral geometry and the coil geometry or taper. Below, the specified parameters are for the final optimized design. The selection of these parameters is supported by various simulation results which are discussed in this section. It is important to keep in mind that the parameters were chosen to achieve as much miniaturization as possible with minimal impact on the high frequency performance. The parameters were also selected based on manufacturability.

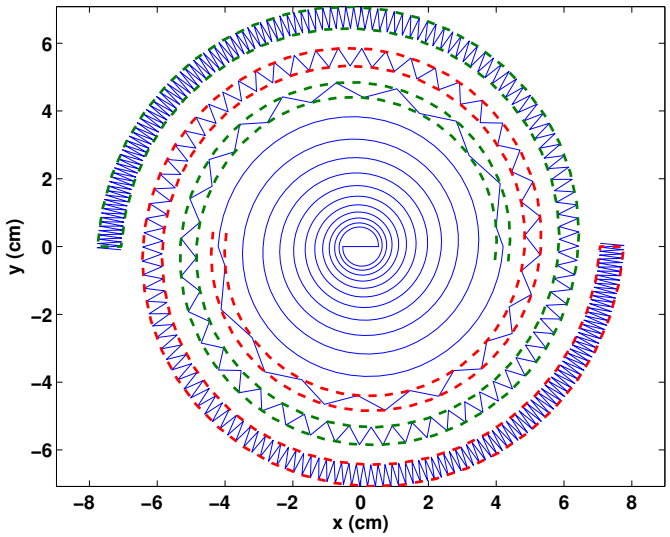

Figure 5.14: Top view of the 6" diameter miniaturized spiral illustrating the pitch taper design.

To start, the spiral geometry parameters were chosen to be the same as those used in section 5.2 which are $r_0 = 0.5cm$, $a = 0.0602$ ($\tau = 0.685$) and $\delta = 0.5\pi$. The parameters associated with the coil geometry were then determined using the guidelines specified in the previous section. First of all, the taper length was chosen to be $1.05\lambda_0$ which conveniently corresponds to the last 1.5 turns of the spiral. Consequently, the starting radius for the inductive loading was 1.5654 inches which implies a starting frequency of 1200 MHz. Since PCB fabrication was used, the coil thickness t is a constant 0.25 inches. Therefore, the taper profile was controlled using the width and pitch. From equation 5.2, it is observed that the inductance is inversely proportional to the pitch squared and approximately proportional to the width. Thus, the inductance is predominately determined by the pitch. To obtain an exponential taper

profile, the pitch was varied exponentially according to the following expression:

$$p(s) = p_i e^{\alpha s} = p_i e^{s\left(\frac{1}{L_{taper}} ln\left(\frac{p_e}{p_i}\right)\right)}. \tag{5.8}$$

where s is the distance from the beginning of the taper ($0 \leq s \leq L_{taper}$), p_i is the initial pitch and p_e is the ending pitch. For the final design, the ending pitch p_e is 45 mils and the initial pitch p_i is twenty times larger than p_e. To simplify the creation of the coil, the coil width varies in accordance with the curves (see equation 5.1) that define the edges of the spiral arm (see Fig. 5.14). It can be shown that the width of the coil at a distance s from the beginning of the coil is given by the following

$$w(s) = (as + r_{start}) \left|1 - e^{a\delta}\right| sin\psi. \tag{5.9}$$

where $\psi = tan^{-1}(1/a)$. Therefore, the width is a linear function of s. The linear variation of the width has a minor impact on the taper shape as demonstrated in Fig. 5.15 where the coil inductance is compared with an exponential curve. Note that the coil inductance has been calculated at a frequency of 150 MHz using equation 5.2 and 5.3 and an effective radius[17] $a = \sqrt{wt/\pi}$. From Fig. 5.15, there is no observable difference between inductance of the tapered coil and the exponential curve. In fact, there is less than a 2% difference between the two curves.

Since the taper length and profile have already been optimized, the two remaining parameters that need to be optimized are the maximum (ending) inductance and the minimum (initial) inductance of the taper. The maximum inductance depends on three variables which are p_e, t and δ (controls the width) whereas the minimum inductance depends on p_i, t and δ. To begin the optimization of these variables, the

[17]The effective radius is based on a circle with the same area as the cross-sectional area of the rectangular coil

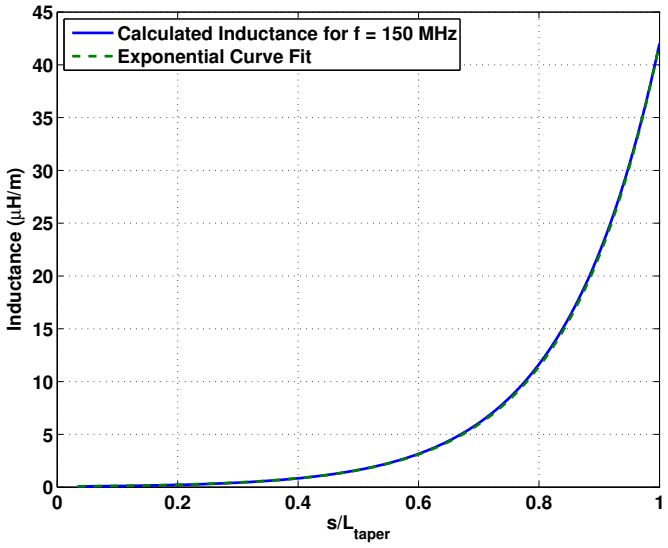

Figure 5.15: Comparison between the calculated inductance of the exponential pitch taper design and an exponential curve.

effect of varying p_e was considered first for the case where $t = 0.25$ in, $\delta = 0.5\pi$ and $p_i = 0.9$ in. A comparison of the realized gain is shown in Fig. 5.16 for the cases where p_e equals 60, 45 and 30 mils. For each case, the realized gain was calculated using an impedance Z_0 which provides the best overall mismatch efficiency (see equation 5.6). The impedance used for calculating the realized gain was 330Ω for the unloaded spiral, 320Ω for $p_e = 60$ mils, 323Ω for $p_e = 45$ mils and 320Ω for $p_e = 30$ mils. It is evident that the three cases are rather similar except at lower frequencies. For example, the -15 dBi realized gain point occurs at 170, 155 and 160 MHz for p_e equal to 60, 45 and 30 mils respectively. As expected, more miniaturization is achieved using a smaller pitch because of the larger inductance. However, it is apparent that $p_e = 45$ mils marks the onset of diminishing returns. Additionally, the realized gain for $p_e = 30$ mils is about 0.5 dB lower on average at higher frequencies than the

$p_e = 45$ mils case. Therefore, it was concluded that the case where $p_e = 45$ mils provides the best overall performance.

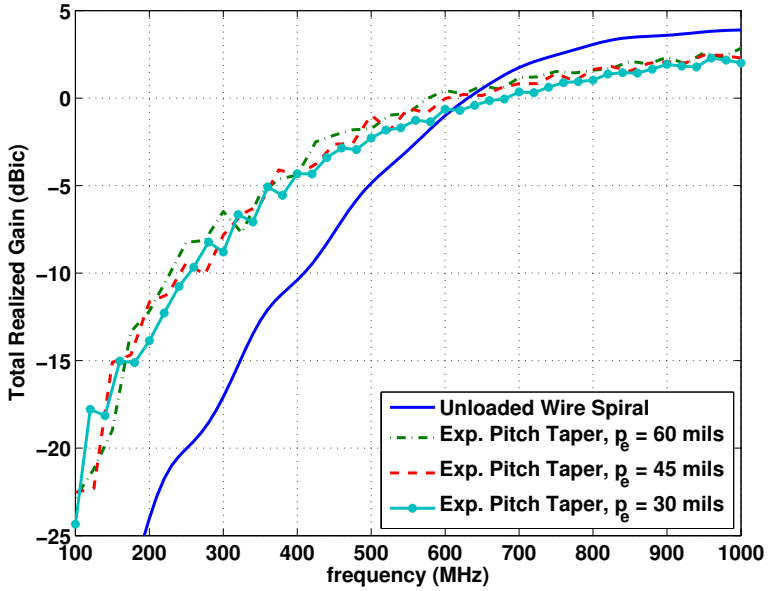

Figure 5.16: Comparison of the realized gain for selected values of the ending pitch p_e ($t = 0.25\ in$, $\delta = 0.5\pi$, $p_i = 0.9\ in$).

The next parameter to be optimized was the coil thickness t. For each thickness, the parameters p_e, δ and p_i are equal to 45 mils, 0.5π and 0.9 inches respectively. A comparison of the realized gain is shown in Fig. 5.17 for the cases where t equals 0.125, 0.25 and 0.5 inches. Essentially, from one case to the next the final inductance is approximately doubled. As before, the realized gain was calculated using an impedance Z_0 which provides the best overall mismatch efficiency. The impedance used for calculating the realized gain was 338Ω for $t = 0.125\ in$, 323Ω for $t = 0.25\ in$ and 351Ω for $t = 0.5\ in$. Comparing the cases where $t = 0.125\ in$ and $t = 0.25\ in$, the only observable difference between them is below 200 MHz where the quarter inch

thick design has a higher realized gain. Below 140 MHz, the half inch thick design has the highest realized gain but, elsewhere, its performance is worse especially above 600 MHz. This is likely the result of the initial inductance being larger than the other two cases. The initial inductance can be lowered to improve the high frequency performance by increasing the initial pitch p_i but the real issue with the half inch design is its manufacturability and large profile. That is, its thickness makes PCB fabrication difficult and increases the overall profile of the antenna. For these reasons, a quarter inch thickness was used for the final design.

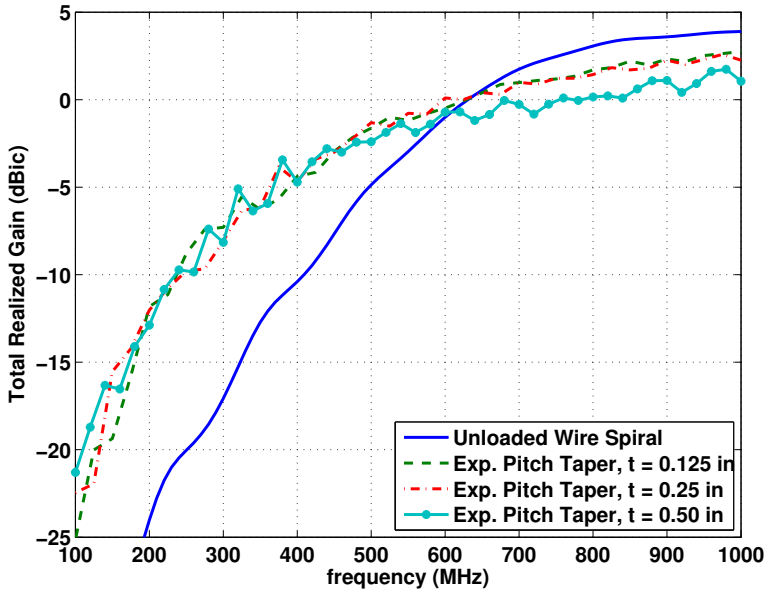

Figure 5.17: Comparison of the realized gain for different coil thicknesses t ($p_e = 45mils$, $\delta = 0.5\pi$, $p_i = 0.9in$).

In an attempt to further increase the low frequency realized gain, the width was optimized by increasing the angle δ. For each angle, the parameters p_e, p_i and t are equal to 45 mils, 0.9 in and 0.25 in respectively. The realized gain is compared in

Fig. 5.18 for the cases where δ equals 0.5π, 0.6π and 0.7π. Note that in varying δ from 0.5π to 0.7π, the width increases by a factor of 1.43. From Fig. 5.18, it is apparent that δ has minimal impact on the realized gain. Therefore, for this design, the point of diminishing return has already been reached for $\delta = 0.5\pi$.

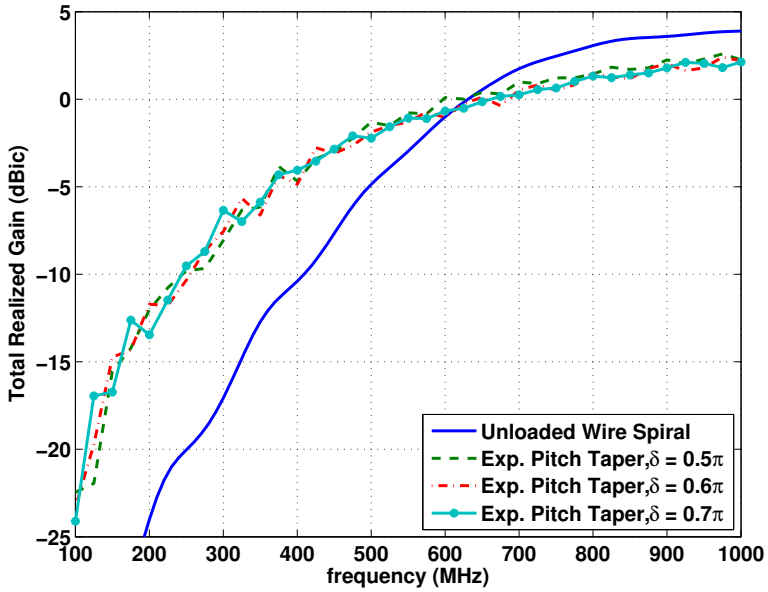

Figure 5.18: Comparison of the realized gain for different δ angles which controls the width of the coil ($p_e = 45$ mils, $t = 0.25$ in, $p_i = 0.9$ in).

The last parameter to be optimized was the initial pitch p_i. This parameter is important because it mainly determines the impedance discontinuity seen at the junction of the unloaded and loaded sections. To minimize the discontinuity, p_i should be as large as possible to make the initial inductance as small as possible. The effect of p_i on the realized gain is shown in Fig. 5.19 for the cases where p_i is ten, twenty and thirty times larger than p_e. In each case, the parameters p_e, δ and t are equal to 45 mils, 0.5π and 0.25 in respectively. From Fig. 5.19, it is observed that p_i only

has an effect on the realized gain above 500 MHz. For this range of frequencies, it is evident that a larger p_i results in a higher realized gain. Furthermore, the point of diminishing return is reached around $p_i = 20p_e$. Therefore, the final design has an initial pitch p_i equal to $20p_e$ (0.9 in).

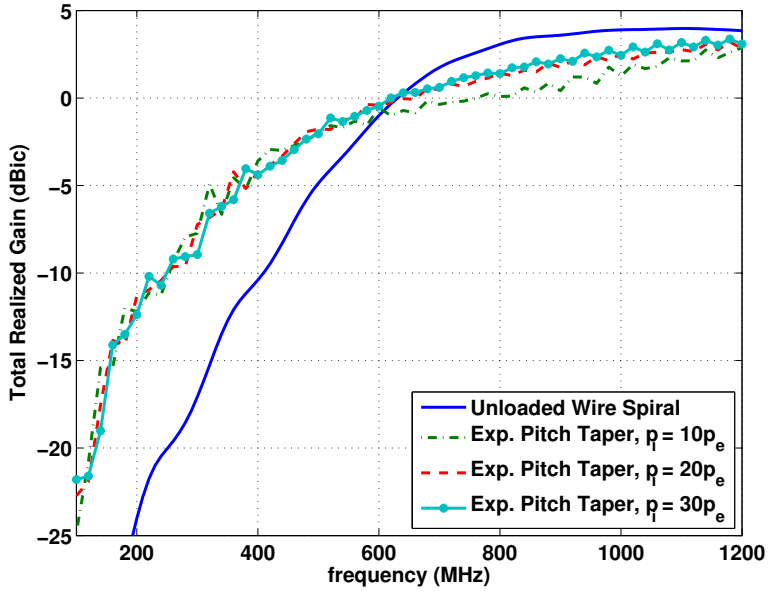

Figure 5.19: Comparison of the realized gain for selected values of the initial pitch p_i ($p_e = 45mils$, $t = 0.25in$, $\delta = 0.5\pi$).

Before proceeding to the next section, it is important to comment on the performance achieved by the inductive loading. First of all, defining the miniaturization factor based on the -15 dBi gain point, the miniaturized spiral achieves a miniaturization factor of about 2.1. This corresponds to a -15 dBi gain at about 150 MHz which is within 40 MHz of the theoretical limit for a 6" diameter aperture (limit is 111 MHz, see Fig. 2.15). Recall that the theoretical limit is for an antenna that utilizes the entire volume of the radian sphere. Since the miniaturized spiral only occupies

about 6% of the volume of the radian sphere, its performance is rather remarkable. Secondly, in comparison to a spiral loaded on both sides with dielectric material, the same miniaturization can be achieved using a dielectric constant of about 100 (see Fig. 4.7) and a thickness of 0.2". However, the dielectrically loaded spiral would weight significantly more than the inductively loaded spiral even if the thickness was tapered.

5.4.2 Fabrication and Measurement

In the previous section, all of the NEC simulations were in free space and used a wire diameter of 4 mils to ensure that each wire segment had a length-to-diameter ratio sufficiently large that the filamentary current approximation was valid. As a result, the impedance Z_0 needed to maximize the mismatch efficiency was 323Ω which is significantly larger than the typical 50Ω system impedance. One way of matching a high impedance antenna to a given system impedance is to employ an impedance transformer which also can act as the balun. In this case, if an impedance transformer were used it would have to be a custom design because a commercially available transformer with the required bandwidth and transformation ratio could not be found. As an alternative, the impedance of the antenna could be reduced to match the system impedance by increasing the wire diameter (arm width) and/or dielectric loading. This approach was used to match the antenna to a 180° M/A-COM hybrid balun (30-3000 MHz, part number H-183-4-N) which has a 100Ω output impedance and a 50Ω input impedance.

Typically, to reduce the input impedance of a spiral only the arm width needs to be adjusted. However, in this case the wire diameter can not be increased arbitrarily

if the antenna is analyzed using MOM because the accuracy of MOM relies on the validity of the filamentary current approximation. That is, the length-to-diameter ratio for each wire segment must be sufficiently large (usually greater than two). For the coiled spiral, there are many short wire segments because of the spiral curvature and structural detail of the coil. Additionally, the reduction in phase velocity caused by the inductive loading requires the coil wire segments to be sufficiently small to accurately model structure ($\lambda_g/20$ instead of $\lambda_0/20$). Therefore, the wire diameter was limited to about 20 mils. Using a 20 mil wire diameter, the required matching impedance Z_0 was reduced from 323Ω to 138Ω. As shown in Fig. 5.20, increasing the wire diameter had a negligible effect on the overall performance of the antenna as expected. To further reduce the antenna impedance from 138Ω down to 100Ω, the wire diameter could be increased further. To determine the proper wire diameter or arm width, a more computationally intensive and time consuming FEM analysis or an experimental approach would have to be used. However, since the antenna was designed to be fabricated using PCB technology, it is easier to utilize the dielectric constant of the substrate to reduce the impedance to 100Ω.

To determine the appropriate dielectric constant of the substrate simulations were carried out using FEKO since NEC does not support dielectric bodies. The challenge in these simulations was the modeling of the wire structure inside the 0.25 inch thick dielectric substrate. To best handle this situation, method of moments was used in conjunction with a multi-layered Green's function to account for the dielectric substrate. As can be expected, use of the Green's function requires the dielectric substrate to be infinite in extent. This approach was necessary because of numerical issues that were encountered when a finite dielectric layer was used. To determine

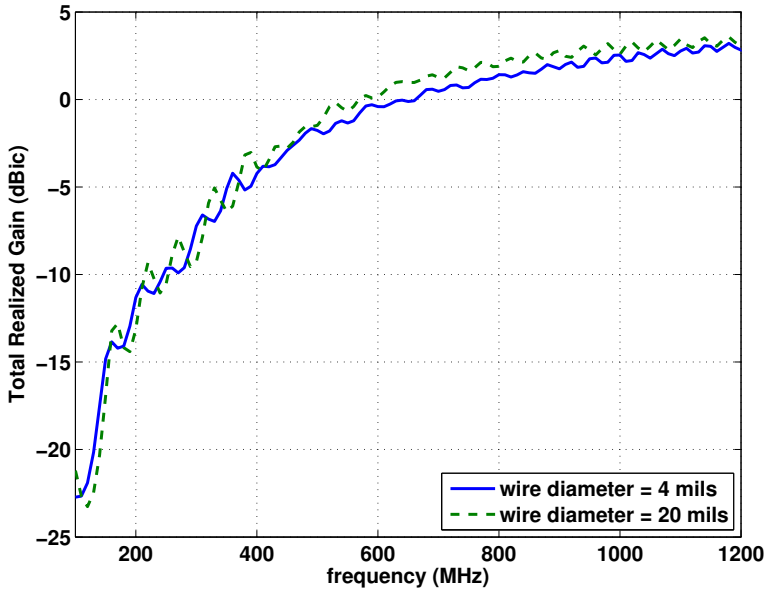

Figure 5.20: Impact of wire diameter on the total realized gain of the 6" diameter inductively loaded spiral (free-space).

the optimal dielectric constant, several simulations were carried out using different dielectric constants for the 0.25" thick layer. For each case, the impedance Z_{opt} that maximized the mismatch efficiency over the frequency range from 100 to 1000 MHz was determined as in section 5.3.1 (see equation 5.6). From the results shown in Fig. 5.21, it is clear that the desired 100Ω impedance is obtained for a dielectric constant of $\epsilon_r = 4$. Based on these results, Rogers TMM4 laminate was selected as the substrate material because it has a dielectric constant of 4.5 and it is very low-loss ($tan\delta = 0.002$).

After adjusting the antenna impedance to match the 100Ω output impedance of the balun, the antenna was fabricated on a 0.25 inch thick Roger's TMM4 substrate ($\epsilon_r = 4.5, tan\delta = 0.002$). The top of the spiral PCB is shown in Fig. 5.22 and the

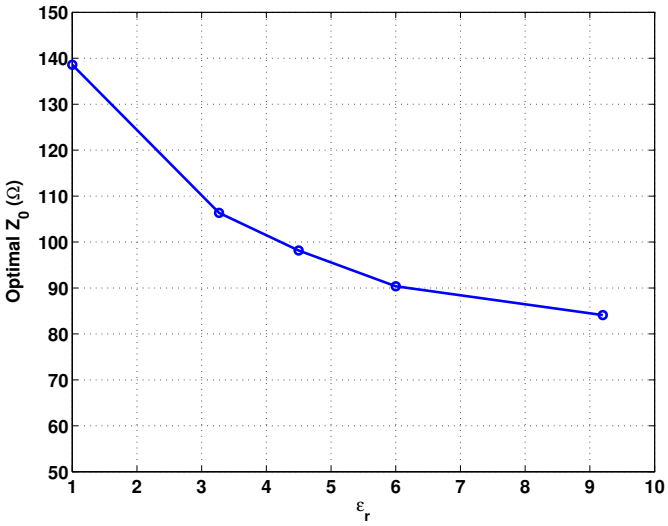

Figure 5.21: Selection of substrate dielectric constant based on its effect on the spiral impedance at high frequency.

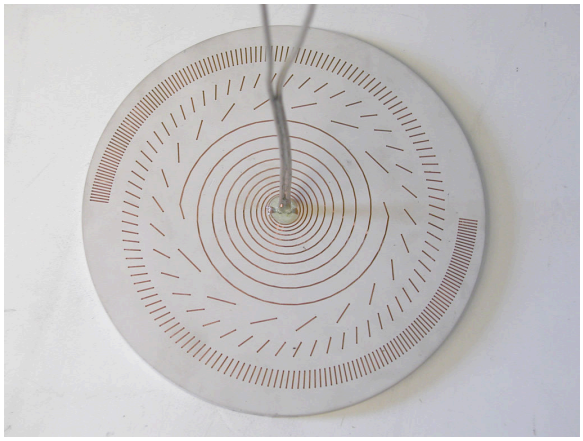

Figure 5.22: Picture of the fabricated 6 inch diameter spiral antenna (pitch taper design) on a 0.25" thick Rogers TMM4 substrate.

measured return loss and realized gain are shown in Fig. 5.23 and 5.24 respectively. In Fig. 5.24, the measured realized gain is compared with FEKO simulations for the spiral in free space and in the infinite dielectric layer. Compared to the other cases, the FEKO simulation with an infinite dielectric layer has a higher realized gain below 550 MHz especially between 250 and 500 MHz. This can be attributed to the dielectric layer being larger than the antenna as discussed previously in section 4.3.2. Also, it is possible that the lower measured realized gain between 250 and 500 MHz could be due to a problem with the measurement setup. Outside this frequency range the agreement between simulation and measurement is very reasonable. For instance, taking the average of the measurement, the -15 dBi point occurs around 167 MHz compared to 155 MHz for the simulated spiral in free space. This agreement is as good as can be expected since the antenna in each simulation is different in some way than what was measured. Unfortunately, this situation was unavoidable since FEKO could not be used to simulate the exact antenna. Nevertheless, the agreement between simulation and measurement is good enough to validate the inductively loaded spiral design.

5.5 18" Spiral Design for VHF and UHF Operation

The purpose of this section is to discuss the extension of the operating range to lower frequencies by scaling the spiral aperture. To do so, an 18" diameter aperture is considered for VHF and UHF coverage. At first, the subject of this section appears to be trivial because the operating range of the miniaturized 6" spiral from the previous section can easily be shifted to lower frequencies by simply scaling the entire geometry. That is, the 6" design can easily be scaled by a factor of three to produce an 18"

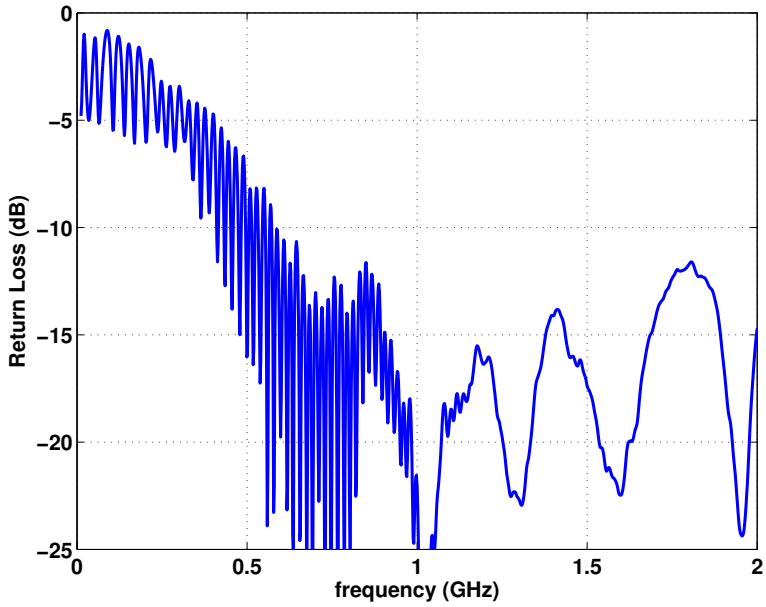

Figure 5.23: Measured return loss for the 6" diameter inductively loaded spiral in free-space.

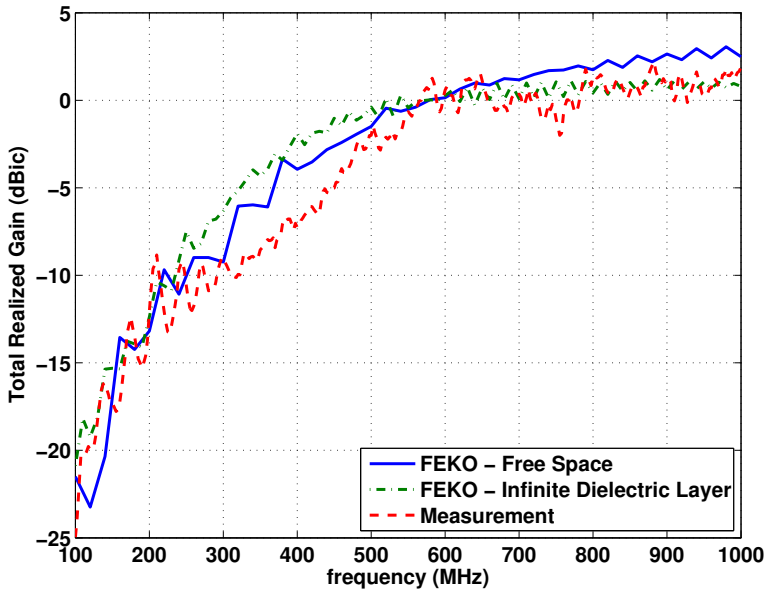

Figure 5.24: Comparison between measurement and simulation for the free standing 6" diameter inductively loaded spiral.

diameter spiral with a thickness of 0.75". However, the resulting 18" design can not be fabricated using standard PCB technology for a variety of reasons. First of all, the dimensions of the antenna exceed the standard panel size of most available materials especially in regards to the thickness. Therefore, the 18" design would require a custom panel size for fabrication. Assuming this is possible, most PCB manufacturers do not have the capability to make an 18" diameter PCB. Those that are capable do not have the capability to fabricate PCBs with thicknesses greater than three tenths of an inch. Unless the coil can be made thinner, the only viable option for fabricating larger aperture sizes is wire forming techniques. Note that the possibility of making the coil thinner is discussed in section 5.6.

In light of the facts above, wire forming techniques were employed to construct the coiled section of the spiral arm for the 18" diameter antenna. In doing so, the previous coil design had to be redesigned because the exponential variation of the pitch made fabrication extremely difficult. To ease fabrication, the redesigned coil was tapered by linearly varying the cross-sectional area of the coil while maintaining a constant pitch. Essentially, the resulting coil is a conical compression spring that is readily manufacturable by most commercial spring manufacturers. The design and optimization of this coil is discussed in more detail in the following section whereas section 5.5.2 focuses on the fabrication and measurement of the miniaturized 18" spiral.

5.5.1 Design and Optimization

The coil geometry for the 18" spiral was designed and optimized based on a 6" diameter spiral with the same geometrical parameters used in the previous 6" spiral

design ($r_0 = 0.5$ cm, $a = 0.0602$, $\delta = 0.5\pi$). Using the knowledge gained from sections 5.3 and 5.4.1, the conical coil taper design reduces to the selection of the following parameters which are the taper length L_{taper}, initial inductance L_i and final inductance L_e. In accordance with the findings in section 5.3.2, the taper length was chosen to be $1.05\lambda_0$ which was the same as the previous 6" spiral design (exponential pitch taper design). As before, the initial inductance depends upon the initial coil width w_i, thickness t_i and pitch p_i. Similarly, the final inductance depends upon the final width w_e, thickness t_e and pitch p_e. To simplify fabrication, the tapering of the coil was restricted to a linear variation in the width and thickness. Thus, the same pitch p was used for the initial and final pitch leaving five parameters to be determined. Just like the exponential pitch taper design, the final coil width was determined by the spiral arm width which depends upon the previously selected growth rate and angle δ. Based on these parameters the final width w_e was 275 mils. To make the initial inductance of the coil as small as possible yet still manufacturable, the initial width and thickness were chosen to be 22 and 20 mils respectively. Therefore, only the final thickness t_e and pitch p need to be determined or optimized. These parameters were chosen based on how much miniaturization was achieve while taking into consideration fabrication issues.

To begin, the pitch of the conical coil was optimized. Recall that in section 5.2.2 a pitch of 60 mils was used to demonstrate the potential of the coiled spiral. Since the performance was impressive, a pitch of 60 mils was used as a starting point for this optimization where the final thickness was 0.25". A comparison of the realized gain is shown in Fig. 5.25 for the cases where the pitch is 60, 45 and 30 mils. As before, the realized gain was calculated in each case using an impedance Z_0 which provides

the best overall mismatch efficiency (see equation 5.6). In comparison to the 60 mil case, it is evident that decreasing the pitch does not result in further miniaturization. Overall, the realized gain actually deteriorates across the entire frequency range. This behavior is indicative of the initial inductance being too large. The only way to further reduce the initial inductance without reducing miniaturization is to use a variable pitch as in the previous exponential pitch taper design. Since this is not a viable option for this design, the pitch was chosen to be 60 mils.

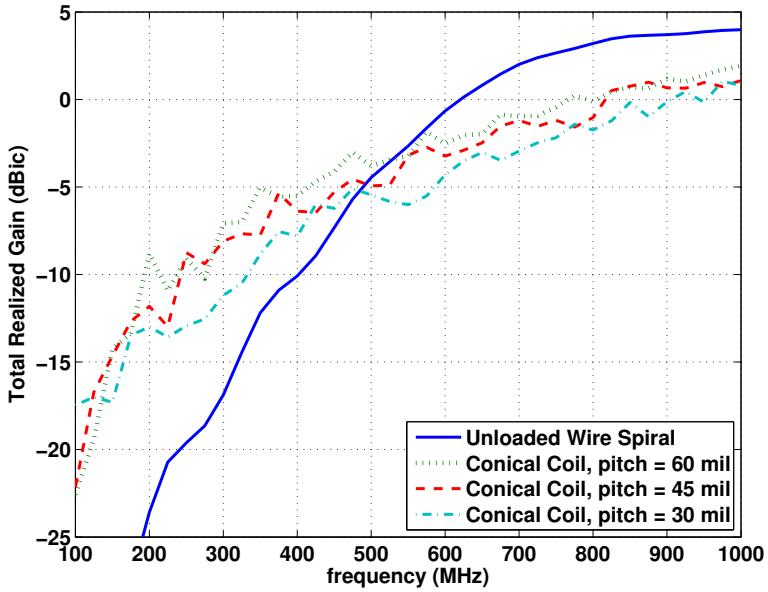

Figure 5.25: Impact of pitch on realized gain for the linear tapered conical coil design (6 inch aperture).

Using a pitch of 60 mils, the impact of the final thickness was examined by simulating the spiral with a final thickness of 0.9, 0.25 and 0.5 inches. From the realized gain curves shown in Figure 5.26, it is clear that increasing the final thickness does improve the gain at lower frequencies. Specifically, increasing the thickness from 250

mils to 500 mils, the -15 dBic gain point has shifted from 147 MHz to 130 MHz where the aperture size is only $\lambda/12$. However, increasing the final thickness also reduced the gain at the higher frequencies. More importantly, the improvement in the low frequency gain does not necessarily justify doubling the antenna profile. That is, when the antenna is used in conjunction with a ground plane, increasing the thickness requires a concurrent increase in the spacing between the antenna and ground plane which is undesirable for applications which require a low profile. Taking these observations into account, a final thickness of 0.25 was chosen based on its overall performance.

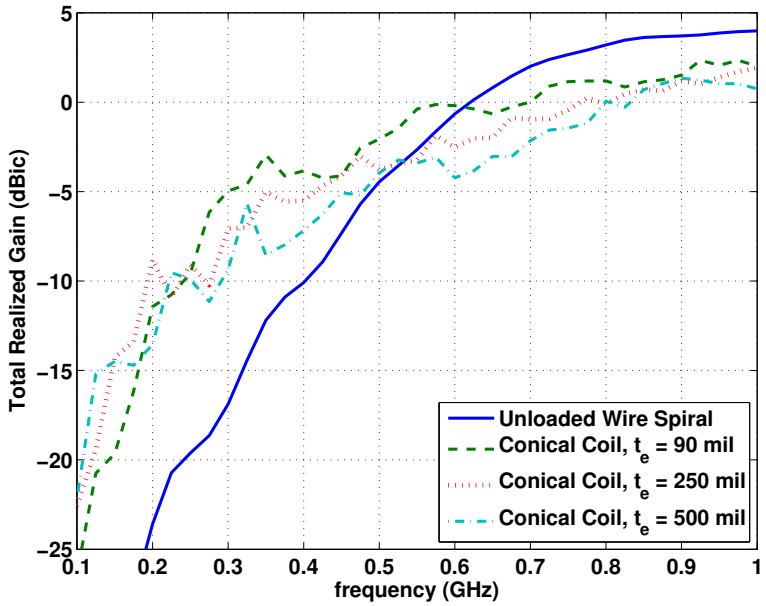

Figure 5.26: Impact of increasing coil thickness on the realized gain of the conical coil design.

Before proceeding to discuss the fabrication and measurement of the 18" spiral, it is useful to compare the performance of the conical coil design to the exponential pitch taper design. A comparison between the realized gain of the two designs is shown in Fig. 5.27. It is clear that both designs achieve a gain of -15 dBi at about 150 MHz. Thus, the conical coil design was able to achieve the same miniaturization even with the restrictions placed on the taper profile by fabrication limitations. However, the effect of the restrictions is evident at higher frequencies where the exponential pitch taper design has 2-3 dB higher gain. In spite of this, the overall performance of the conical coil design is more than adequate given the circumstances.

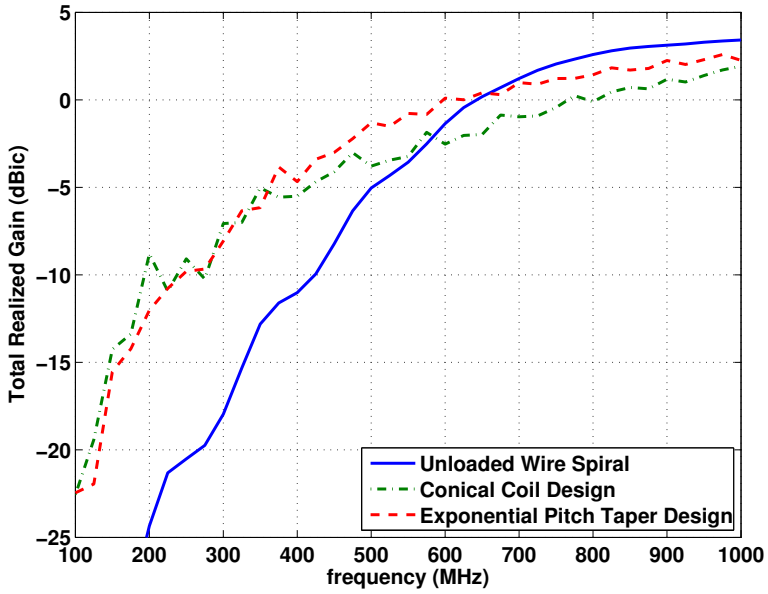

Figure 5.27: Comparison of the exponential pitch taper design and the conical coil design.

5.5.2 Fabrication and Measurement

The first step in fabricating the conical coil design was scaling the entire 6" antenna geometry, including the coil itself, by a factor of 3. To demonstrate the scalability of the design, the realized gain of the 18" and 6" spirals are compared in Fig. 5.28 as a function of their electrical size (D/λ). Clearly, their performance is nearly identical as expected.

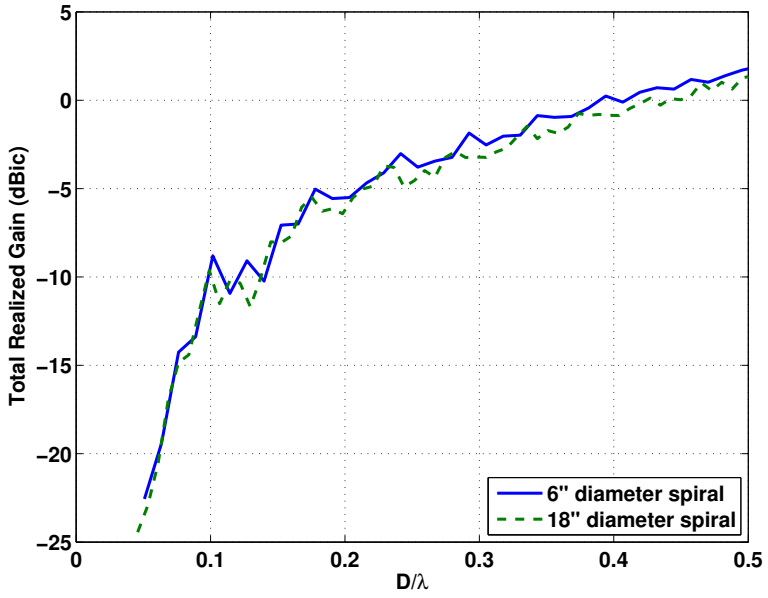

Figure 5.28: A demonstration of the scalability of the inductively loaded spiral antenna using the conical coil design.

To fabricate the 18" spiral prototype, the coiled section of the arm was fabricated by a local spring manufacturer using beryllium copper wire (20 mil diameter). The unloaded center section of the spiral was fabricated on a 19 inch diameter FR4 board (90 mils thickness) which was used to support the free standing coil. The free standing

coil was then attached to the FR4 board using epoxy. To ease fabrication of the coil, the conical coil was formed using a circular cross-section instead of rectangular. This required an adjustment to the coil geometry to maintain the inductance of the coil. The adjustment was made based on maintaining an equivalent cross-sectional area. That is, the radius of the circular coil was calculated from the cross-sectional area of the rectangular using the relation

$$r = \sqrt{\frac{wt}{\pi}} \tag{5.10}$$

where w and t are the coil width and thickness at a given location on the spiral arm. Thus, the circular coil has an initial diameter of 70 mils and a final diameter of 890 mils. To verify the equivalence of the two designs, the realized gain is compared in Fig. 5.29 and agrees quite well, especially the -15 dBi gain point. While the agreement could be made better with further adjustment of the circular coil radius, it was sufficient for testing purposes.

The fabricated 18" prototype is shown in Fig. 5.30 where the conical coiled has been constructed using wire with a 20 mil diameter. As a result of using the same 20 mil wire diameter as the 6" conical coil design, the 250Ω impedance used to match the 18" version was considerably higher. Ideally, the wire diameter of the 18" spiral should also be scaled by a factor of 3 to maintain the impedance. However, it was not possible to form the initial coil turns, which had a diameter of 70 mils, using wire with a diameter of 60 mils. Therefore, a 4 : 1 impedance transformer (1-1000 MHz) with an output impedance of 200Ω was used instead of the 100Ω hybrid balun (30-3000 MHz). A comparison of the simulated and measured realized gain is provided in Fig. 5.31 for the 18" spiral. The agreement between simulation and measurement is very good and validates the performance of the conical coil design. In essence, the

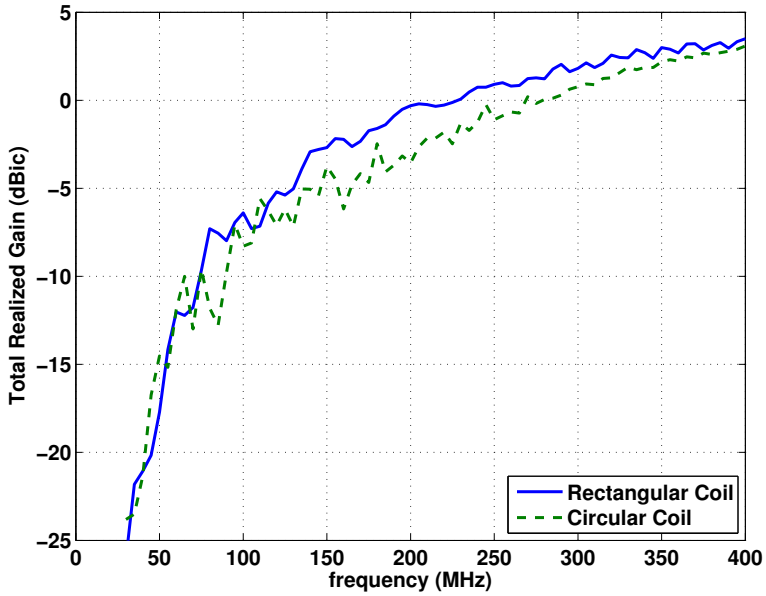

Figure 5.29: Comparison of the 18" conical coil design with a rectangular cross-section and a circular cross-section.

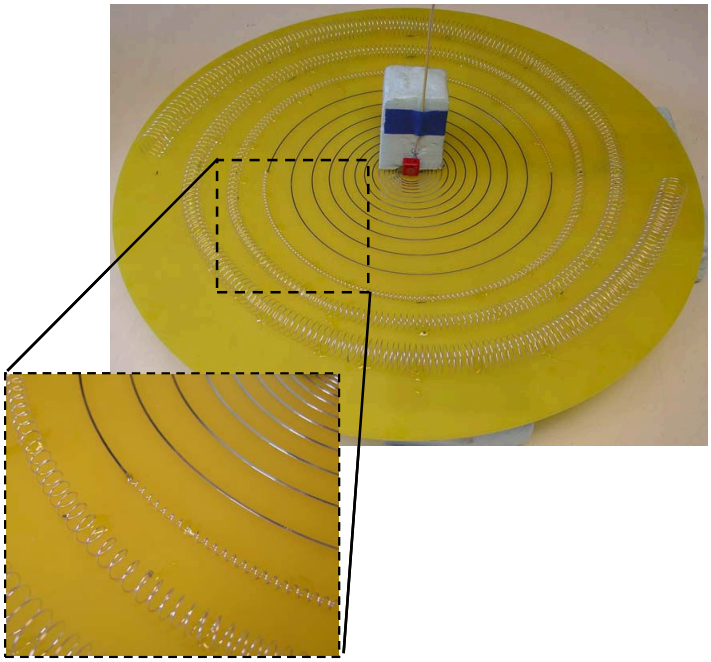

Figure 5.30: Fabricated 18 inch diameter spiral antenna with conical coiled arms.

antenna is able to achieve a gain of -15 dBic at 55 MHz where it has an aperture size of $\lambda/12$. The oscillations in the gain curve are due to impedance matching issues.

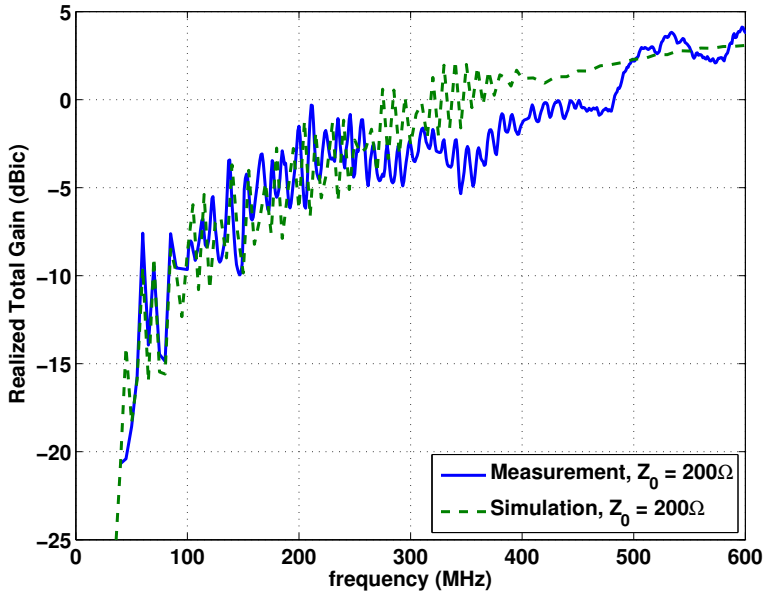

Figure 5.31: Comparison of measurement and simulation results for the 18 inch diameter spiral with volumetric inductive loading.

That is, ideally the balun should have an 250Ω output impedance instead of 200Ω. However, the M/A-COM impedance transformer (part number TP-103) was the best commercially available balun that could provide an impedance close to 250Ω over the largest bandwidth (1-1000). To improve the impedance matching, the antenna could be loaded with dielectric or a custom balun could be designed. In this case, an attempt was made to lower the impedance of the antenna by embedding the coiled section of the spiral arm in a polymer ceramic. However, this was not possible because the viscosity of the polymer ceramic prevented it from freely flowing between the coil turns. By using only the base material (silicone), the viscosity was low enough to

freely flow between the coil turns. The coiled section of the spiral arm embedded in silicone is shown in Fig. 5.32. It is remarked that the dielectric constant of silicone is

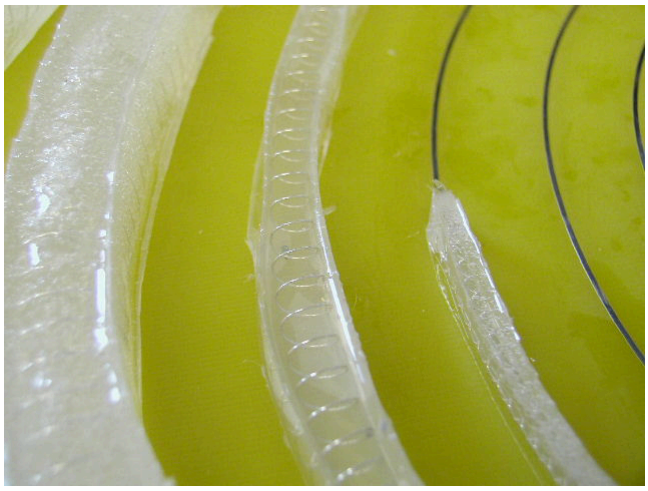

Figure 5.32: Fabricated 18 inch diameter spiral antenna with conical coiled arms embedded in silicone.

only 2.5 which is not large enough to have an appreciable effect. This is evident from Fig. 5.33 where the measured realized gain is compared for the 18" spiral with and without the silicone (see Fig. 5.34 for return loss comparison). Clearly, the peak-to-peak variation of the oscillations is smaller when the coil is embedded in the silicone but the difference is not significant. Therefore, a material with a larger dielectric constant is needed to further improve the impedance match. In the future, this can be achieved by mixing ceramic powder with a polymer base that has a sufficiently lower viscosity.

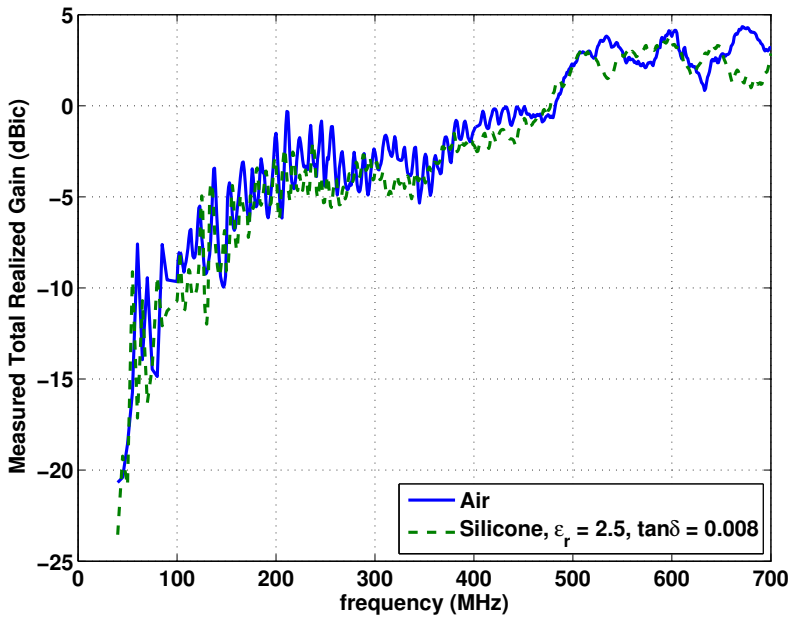

Figure 5.33: Comparison between the measured realized gain of the 18 inch diameter spiral with and without dielectric (silicone) loading.

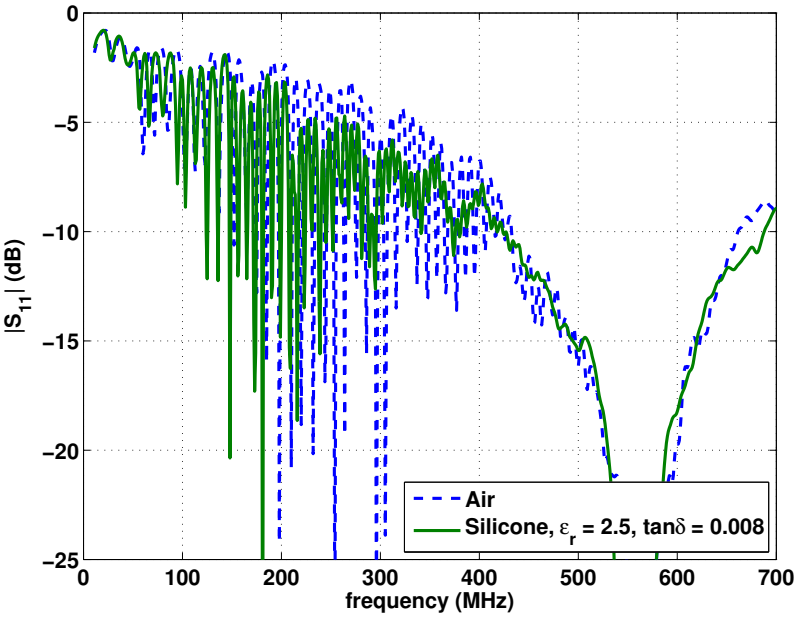

Figure 5.34: Comparison between the measured return loss of the 18 inch diameter spiral with and without dielectric (silicone) loading.

5.6 Summary

This chapter focused on the use of inductive loading to miniaturize a spiral antenna. The goal was to meet or exceed the miniaturization achieved by material loading (dielectric) in the previous chapter without significantly increasing the antenna weight. Various methods were considered for implementing the inductive loading such as lumped inductors, planar meandering and a novel coiling approach. It was shown that the coiling approach could achieve more miniaturization than the traditional planar meandering at the expense of increased fabrication complexity. Using this approach, a detailed computational study was conducted to miniaturize the spiral to the fullest extent with negligible impact at higher frequencies. The knowledge gain from this study was then employed in the design of a 6" and an 18" diameter spiral. Because of fabrication issues, the 18" spiral was not a scaled version of the 6" spiral. In regards to overall performance, the inductive loading design (coil) for the 18" spiral was inferior to the 6" spiral design (exponential pitch taper design). However, both were able to achieve a miniaturization factor of 2.1 which corresponds to a 53% reduction in size. The miniaturization achieved by these designs compares well to the theoretical limit of 2.9 which is approximately a 66% reduction in size.

In the future, the fabrication limitations which restrict the overall performance of the 18" spiral design need to be overcome. This can be accomplished by reducing the coil thickness or the physical size of the coil in general. There are two foreseeable ways in which this can be accomplished. First of all, the exponential pitch taper design (see section 5.4) can be made thinner by decreasing the pitch to compensate a reduction in thickness. This is demonstrated in Fig. 5.35 for the 6" spiral which utilizes the exponential pitch taper design. Here, the thickness has been reduced from 0.25" to

0.125" while the final pitch p_e has been adjusted to maintain the proper inductance (in both cases $p_i = 20p_e$). Clearly, the realized gain of the spiral has been maintained even though it is half as thick as the original. The extent to which the thickness can be reduced in this manner is not known but it is worth investigating in the future. It is important to note that the 0.125" thick design is still not thin enough to easily fabricate an 18" version of the antenna. Another approach is to replace the dielectric substrate with a magneto-dielectric material or to fill only the coil with a magneto-dielectric material. The larger permeability of the magneto-dielectric material would permit a physically smaller coil to achieve the same inductance as a larger coil. Therefore, a magnetic substrate could shrink the physical size of the coil making it possible to significantly reduce the thickness of coil. Note that the permeability does not necessarily need to be large to achieve a useful reduction in thickness. For instance, a μ_r of two would be quite useful assuming the magnetic losses are small. Of course, magnetic loss is the key issue for exploiting this approach especially at higher frequencies.

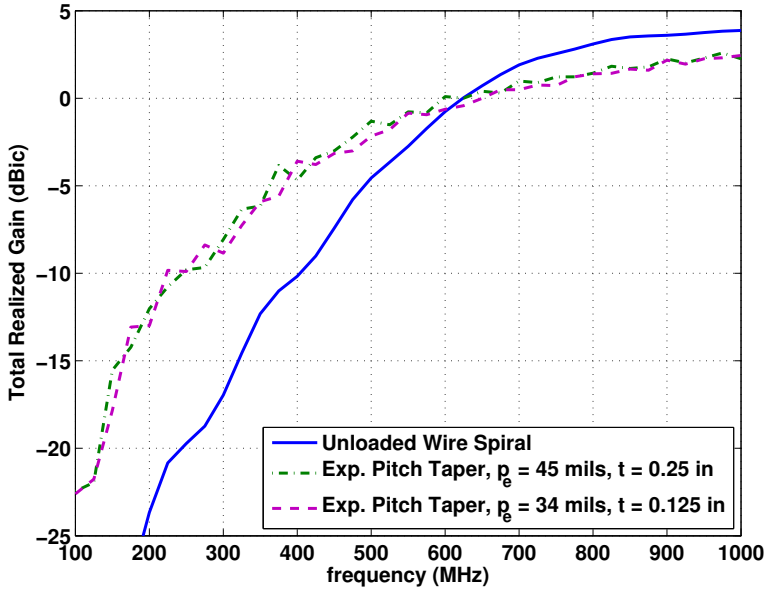

Figure 5.35: A comparison of two exponential pitch taper designs with different thicknesses (6" diameter spiral).

CHAPTER 6

FERRITE COATED GROUND PLANE FOR LOW-PROFILE BROADBAND ANTENNAS

6.1 Introduction

Most antennas have an omni-directional pattern, such as a dipole ($L < \lambda/2$), or a bi-directional pattern, such as a spiral antenna. When integrating these types of antennas into a platform such as a ship or airplane, the interaction between the platform and the antenna is unavoidable. Furthermore, the interaction with the platform can have a significant affect on antenna performance depending upon how the antenna is integrated into the platform. In most applications, the antenna is integrated in such a way as to minimize its profile. This could involve mounting the antenna flush with the platform surface, recessed or slightly protruding from the surface. Regardless of how it is mounted, the antenna is usually backed by some kind of conductive surface. In most cases, the antenna is backed by the metallic platform surface but it also could be enclosed in a metallic cavity. In any case, the presence of a metallic surface affects the performance of the antenna depending upon the electrical separation between them. If the antenna is electrically too close to the conductive surface, the antenna is effectively shorted out by the surface. This results in a small radiation resistance [68]

which, in turn, leads to a poor radiation efficiency and a smaller impedance bandwidth caused by matching difficulties (increased energy storage). Typically, this issue is addressed by making the spacing between the radiating element and conductive surface at least a quarter-wavelength at the lowest operating frequency. For low frequency applications (i.e. HF, VHF, etc.), such a spacing results in profile or height that is impractical. Therefore, for low frequency applications, there are basically two approaches for reducing the profile: 1) Reduce the profile at the expense of performance, 2) Replace the existing conducting surface with an alternative surface that minimizes performance degradation for low-profile applications.

Clearly, the first approach is not ideal since the performance degrades. This is illustrated in the following section in more detail for broadband antennas. In doing so, issues faced specifically for the spiral antenna are discussed in addition to the issues faced in general for any antenna. The remainder of this chapter focuses on alternative surfaces such as electromagnetic band-gap structures (EBG), absorbers and ferrite materials. The applicability of high impedance surfaces is discussed in section 6.3.1. Since these surfaces are not well suited for backing the miniaturized spiral antenna, the remaining sections discuss the use of ferrite materials. In particular, it is demonstrated that by coating a PEC ground plane with a ferrite layer can recover the free-space gain of the miniaturized antenna.

6.2 Issues with Metallic Ground Plane or Cavity

A metallic cavity or ground plane is commonly used to achieve unidirectional radiation and shield electronics mounted behind an antenna. The presence of the ground plane, especially when it is close to the radiating element, significantly alters

the radiation characteristics of the antenna compared to its radiation characteristics in free-space. For instance, the radiation resistance of the antenna decreases as the separation between the ground plane and radiating element decreases[18] [68]. Not only does this result in poor radiation efficiency but it also makes broadband matching difficult because the smaller radiation resistance implies a higher radiation Q. This phenomena can be readily understood from image theory.

Consider a dipole antenna located a height h above an infinite perfect electric conductor whose orientation is parallel to the PEC surface. Since the current is parallel to the PEC surface, its image has the opposite polarity and it is located a distance h below the PEC surface. As the distance between the dipole and its image decreases, the coupling between them increases and eventually they resemble an open-ended two wire transmission line operating in differential mode. The radiation from such a transmission line becomes negligible as the separation decreases because of the destructive interference between the actual current source and its image. Therefore, the radiation resistance of the dipole will decrease with decreasing separation as shown in [68]. More importantly, this occurs for any planar antenna such as the spiral whose current distribution is parallel to the PEC surface.

Another important effect, especially for broadband antennas, caused by the presence of the ground plane is an oscillatory behavior in the input impedance. This occurs when the wave guided between the ground plane and antenna is completely reflected at the truncation of the antenna structure (at the open end of the transmission line). The reflected wave then returns to the input where it interferes with

[18]Note that the directivity for a horizontal dipole or loop increases as the ground plane is brought closer [29, 68].

the next outgoing wave creating a standing wave current distribution. The resulting input impedance has an exceedingly oscillatory behavior which makes broadband impedance matching more difficult. For the spiral, the reflected current also produces undesired radiation of the opposite polarization sense because it passes through the radiation band in the opposite direction of the outgoing current.

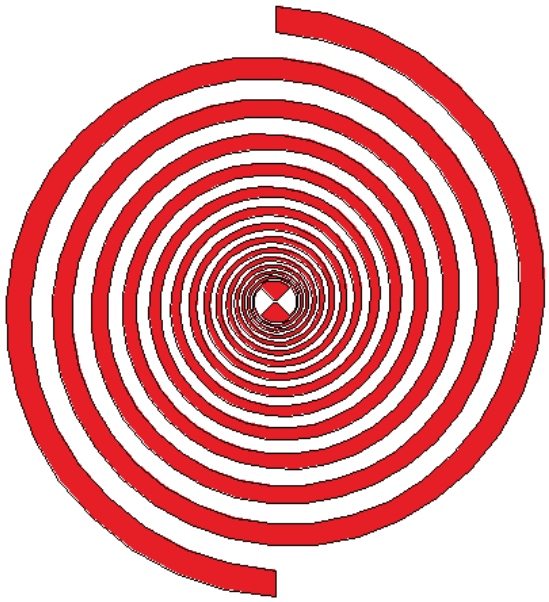

Figure 6.1: A 6 diameter circular log-spiral.

To demonstrate the affect of the ground plane on the spiral antenna, a self complementary log-spiral (shown in Fig 6.1) was simulated using Ansofts HFSS in free-space and above an infinite PEC ground plane. The spiral has a diameter D of 6 inches and an expansion ratio $\tau = 0.685$ (growth rate $a =$). For the infinite ground plane case, the spiral is located a distance of $\lambda_0/6\pi$ above the ground plane where $\lambda_0 = D\pi$. The input impedance is shown in Fig. 6.2 and the effect of the ground plane can clearly

be seen. Notice that the impedance for a free standing spiral is mainly a constant real value for $D > 0.4\lambda$ as expected. However, in the presence of a ground plane the impedance exhibits an oscillatory behavior discussed previously. This makes matching the antenna difficult especially at lower frequencies as demonstrated by the return loss shown in Fig. 6.3. In each case, the return loss has been calculated with respect to a different characteristic impedance in order to achieve the best match across the entire frequency band. Clearly, the impedance bandwidth is reduced by the presence of the ground plane and the amount of reduction will depend upon the spacing.

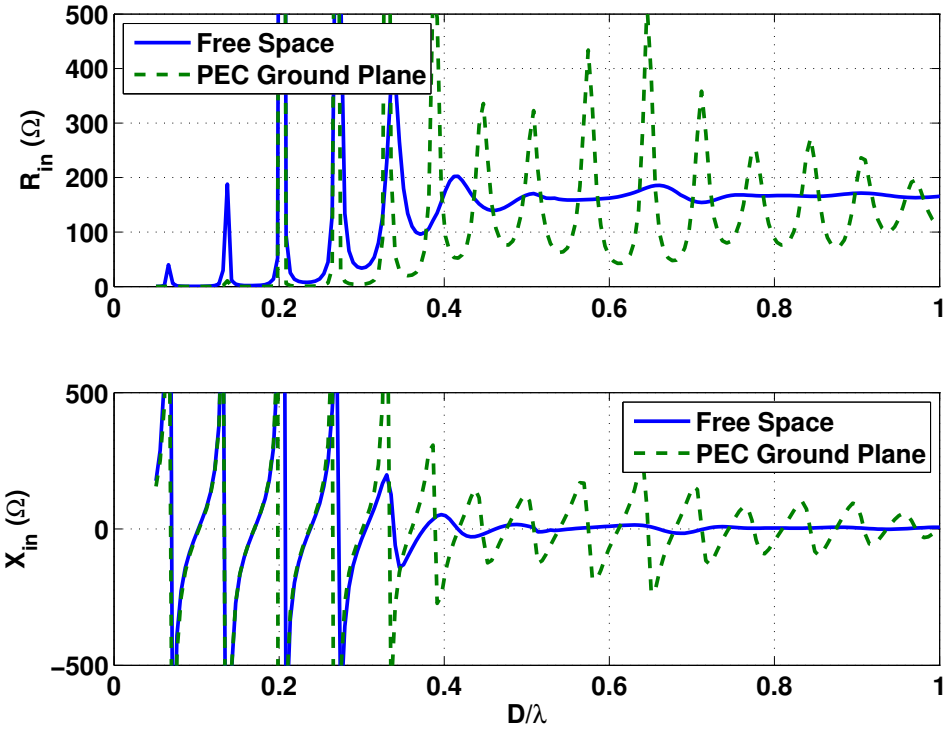

Figure 6.2: A comparison of the input impedance for a circular log-spiral (diameter, $D = \lambda_0/\pi$) in free-space and placed approximately $\lambda_0/20$ ($\lambda_0/6\pi$) above an infinite PEC ground plane.

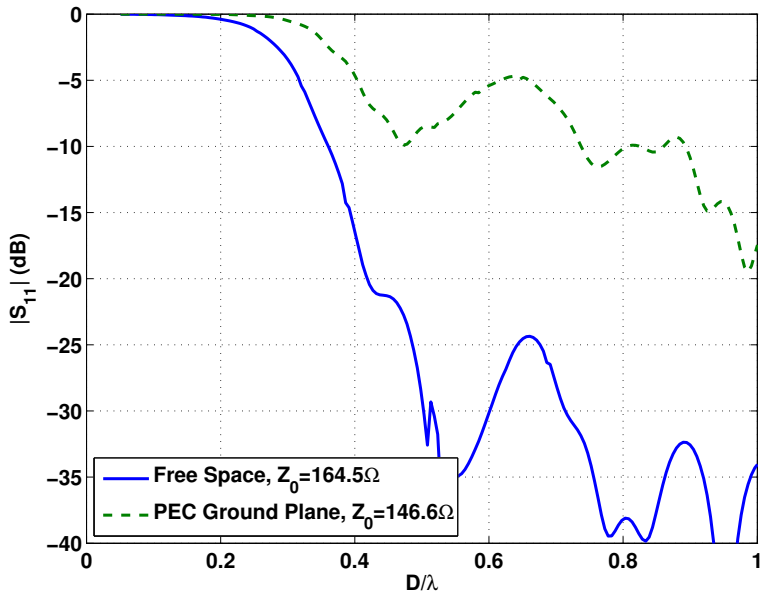

Figure 6.3: A comparison of the return loss for a circular log-spiral (diameter, $D = \lambda_0/\pi$) in free-space and placed approximately $\lambda_0/20$ ($\lambda_0/6\pi$) above an infinite PEC ground plane.

The impedance bandwidth reduction naturally translates into a reduction in the realized gain as shown in Figure 6.4. Here, the total realized gain is compared for the spiral in free-space and backed by an infinite ground plane. This result is a major concern because it implies that the presence of a ground plane can potentially negate the performance improvement obtained by miniaturizing the antenna. Therefore, it is extremely important and necessary to consider alternatives to the PEC ground plane.

Since the spiral naturally radiates a circularly polarized wave, another concern is the affect of the ground plane on polarization isolation or axial ratio. The axial ratio is shown in Fig. 6.5 for the spiral in free-space and backed by an infinite ground plane. It is evident that the presence of a ground plane results in a significant increase in the axial ratio caused by the presence of a strong LHCP component. As mentioned

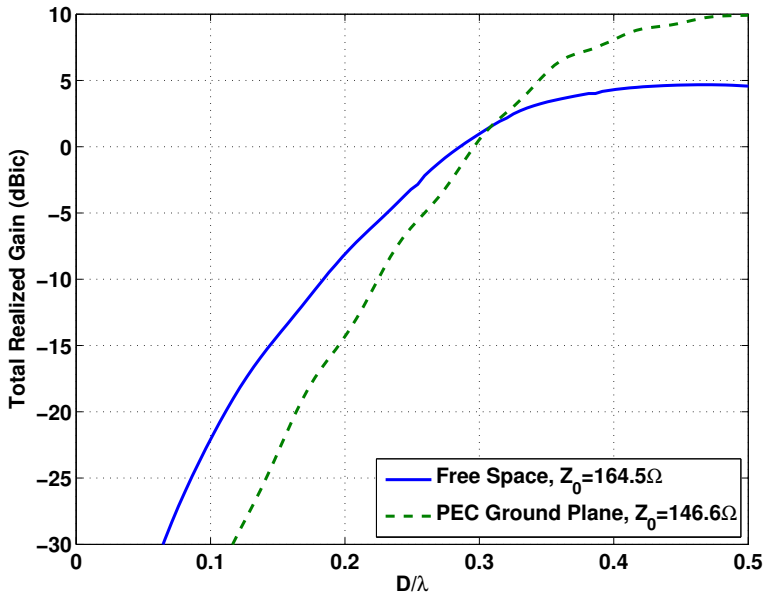

Figure 6.4: A comparison of the total realized gain for a circular log-spiral (diameter, $D = \lambda_0/\pi$) in free-space and placed approximately $\lambda_0/20$ ($\lambda_0/6\pi$) above an infinite PEC ground plane.

previously, this is attributable to the reflected current which radiates with the opposite polarization sense (in this case it is LHCP). This is issue is commonly addressed by attenuating the reflected current. Typically, the spiral is terminated using lumped resistors, resistive film or by placing absorber around it. Another approach is to coat the ground plane with absorber in an attempt to attenuate the wave guided between the antenna and ground plane. In any case, these methods affect the efficiency to varying degrees depending upon how they are applied. Whether these methods should be used depends upon how much they degrade the efficiency of the antenna when it is electrically small because the overall goal is to maintain the performance of the miniaturized antenna at these frequencies.

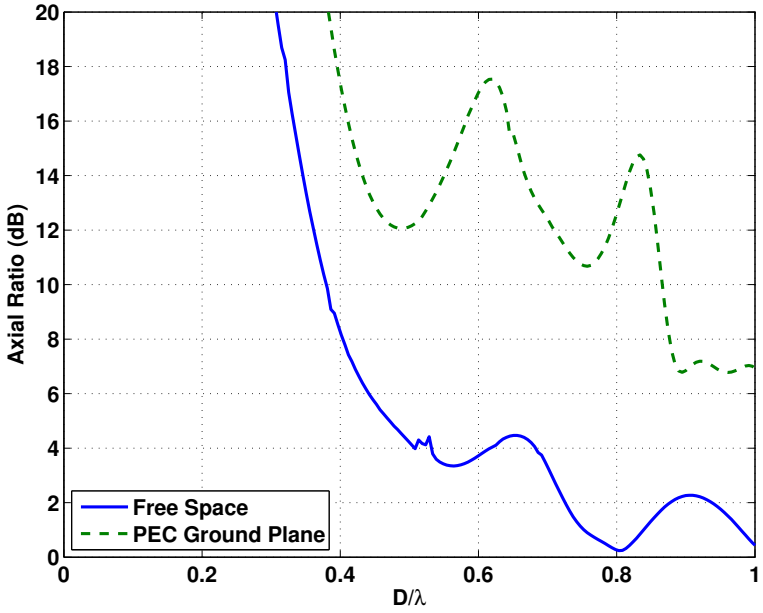

Figure 6.5: A comparison of the axial ratio for a circular log-spiral (diameter, $D = \lambda_0/\pi$) in free-space and placed approximately $\lambda_0/20$ ($\lambda_0/6\pi$) above an infinite PEC ground plane.

6.3 PEC Ground Plane Alternatives: EBG Structures

PEC ground plane alternatives can be divided into two categories which are absorptive treatments and high-impedance surfaces. In the past, absorbing materials were commonly used at the expense of radiation efficiency to address ground plane and, in particular, cavity issues [8]. The idea was to absorb all of the energy directed toward the ground plane since it was not possible to utilize it especially when the spacing was electrically small. More recently, high impedance surfaces such as EBG's [5, 6, 69] have been employed. While these high-impedance surfaces provide some improvement over the PEC ground plane, it is not sufficient in this case. The advantages and disadvantages of these surfaces are discussed in this section. Section 6.4 discusses the use of ferrite materials to overcome the disadvantages associated with high-impedance surfaces. It is noted that the discussion on the use of ferrite materials is not comprehensive in scope or theory. That is, the use of ferrite materials is presented as a proof of concept. A more comprehensive and rigorous analysis is needed to determine the optimal material parameters and to better understand the phenomena. Since this subject, in and of itself, could be a separate dissertation topic, it is left as a topic for future research.

6.3.1 Artificial Magnetic Conductors

The purpose of high-impedance surfaces, such as an EBG, is to emulate the effect of a perfect magnetic conductor[19] (PMC) over a given frequency range. That is,

[19]The existence of a PMC surface is dependent upon the existence of magnetic charge or a magnetic monopole. To date, grand unification theories (really hypotheses) have been developed by theoretical physicists that predict the existence of magnetic monopoles and, in some cases, require their existence for the theory to be valid. However, these theories have yet to be verified and magnetic monopoles have yet to be observed. In fact, at the present time, grand unification theories have been abandoned in favor of string theory which does not require the existence of magnetic monopoles.

they try to achieve a reflection phase[20] of 0° (reflectivity of +1) as opposed to the reflection phase of 180° (reflectivity of −1) obtained from a PEC surface. Recalling the previous discussion of a dipole above a PEC ground plane, if the PEC surface is replaced by a PMC surface then, from image theory, the dipole and its image form a common mode transmission line instead of a differential mode. In this case, as the separation between the actual current source and its image decreases, the interference is constructive rather than destructive. Therefore, an antenna can be placed close to a PMC surface without suffering the negative effects associated with a PEC ground plane. However, it is important to note that antennas which utilize a PEC ground plane will not benefit from a PMC ground plane. For instance, a monopole antenna or a current sheet antenna composed of capacitive type elements [29, 70][21].

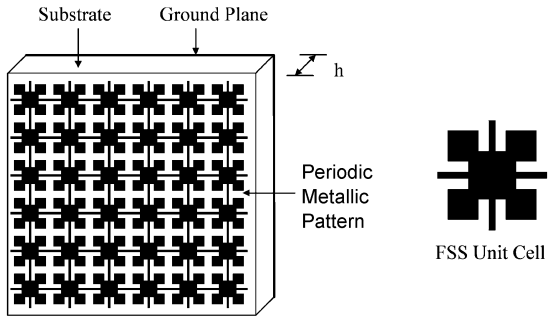

Figure 6.6: Geometry of an AMC ground plane taken from [5].

A subclass of EBG structures known as artificial magnetic conductors (AMC) are commonly used to emulate a PMC surface. The typical AMC consists of a 2-D

[20]The reflection phase is defined as the phase of the reflected electric field at the reflecting surface.

[21]If the elements are inductive then a PMC ground plane would be beneficial

frequency selective surface (FSS) etched on a dielectric substrate which is backed by a PEC ground plane (see Fig. 6.6). At the present time, the most common type of EBG or AMC is the mushroom like design illustrated in Fig. 6.7. Using these structures it is possible to achieve the desired reflection phase of 0° over a given frequency range. However, their applicability is dependent upon the bandwidth of this behavior and the size of the structure.

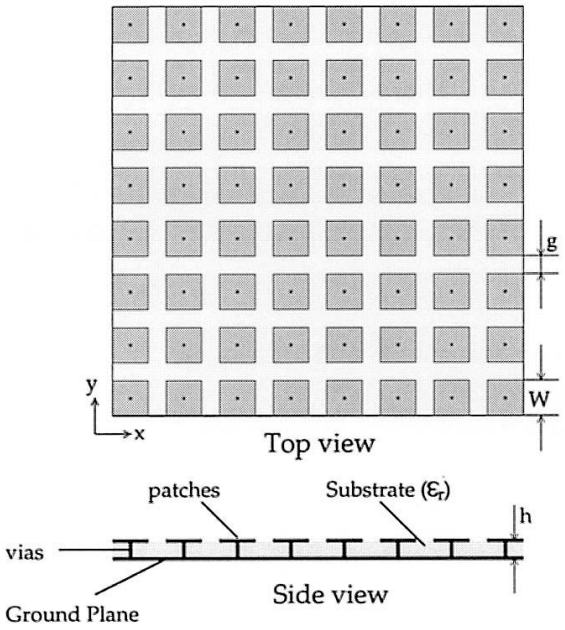

Figure 6.7: Geometry of a mushroom like EBG taken from [6].

For miniaturized broadband antennas, the limited bandwidth and size of the AMC result in several issues. The first issue is that the desired reflection phase of 0° can only be achieved over a narrow bandwidth [5]. Therefore, the bandwidth of a broadband antenna element such as a spiral will exceed the bandwidth of the AMC. However,

this issue is not as severe as it first appears. For a broadband antenna located a height h above a PEC surface, there will always be a frequency for which the electrical height is sufficient to minimize the negative effects of the PEC ground plane. Therefore, the AMC surface only needs to work below this frequency over a bandwidth that is much smaller than the bandwidth of the broadband antenna. Of course, the bandwidth is dependent upon the height h. That is, the bandwidth becomes smaller as h increases. Assuming that the AMC can achieve the bandwidth for a given h, the size of the AMC must be sufficient to resonate at these frequencies to produce the desired reflection phase. In the literature, the elements which make up the FSS are at least 0.1λ in length and the overall AMC size is 1λ at the resonant frequency [6, 71]. Such dimensions are problematic for a miniaturized broadband antenna because, at the frequencies of interest, they would result in an AMC that is larger than the antenna. In fact, the AMC surfaces in [6, 71] are larger than the antenna elements which are not miniaturized. To make matters worse, these AMC's are still not large enough to achieve a bandwidth which is comparable to the antenna in free-space [71]. Therefore, it can be concluded that an AMC is unsuitable for use with a miniaturized broadband antenna because of its size requirements and bandwidth limitations.

6.4 PEC Ground Plane Alternatives: Utilization of Ferrite Materials

This section examines the use of magneto-dielectric materials such as ferrites as an alternative to the PEC ground plane and EBG structure. There are three possible ways in which ferrite materials can be used with two of these approaches being somewhat similar in many aspects. The first approach involves using a layer of ferrite material as a high impedance surface. This requires the relative permeability μ_r

of the ferrite to be significantly larger than the relative permittivity ϵ_r over a given bandwidth as illustrated in Figure 6.8a. Just like an AMC, the goal is to achieve a reflection coefficient close to +1. The advantage of using ferrite material instead of an AMC is that its ability to achieve reflection coefficient of +1 depends upon its material parameters not its physical size (dimensions of FSS structure). However, this approach faces several problems. First of all, to achieve a +1 reflection coefficient the permeability of the ferrite would have to be infinite. Such a material is commonly referred to as a perfect magnetic material. In this case, the thickness of the ferrite material and the boundary condition at the back interface have no affect on the reflection coefficient. However, a perfect magnetic material does not exist. Therefore, the thickness and boundary condition at the back interface affect the reflection coefficient. Of course, the extent of their effect depends upon how large the ratio of μ_r to ϵ_r is. Currently available magnetic materials can have a μ_r up to two orders of magnitude larger than ϵ_r. However, this only occurs over a limited bandwidth and, usually, only at frequencies less than 100 MHz. Despite this, the high-impedance approach is still of interest because of significant interest in low-profile VHF antennas.

The second approach is a different take on the high impedance layer concept. For the high-impedance surface approach, the idea is to use a thin layer of magnetic material which has a $\mu_r >> \epsilon_r$. The second approach tries to take advantage of magnetic materials which have a $\mu_r > \epsilon_r$ by filling the region between the antenna and ground plane with magnetic material. The idea is the presence of the magnetic material will force the antenna to radiate away from the ground plane as discussed briefly in [8]. To explain this concept, consider a planar antenna such as a spiral which lies on the interface between two material half-spaces. The impedance seen by the antenna is

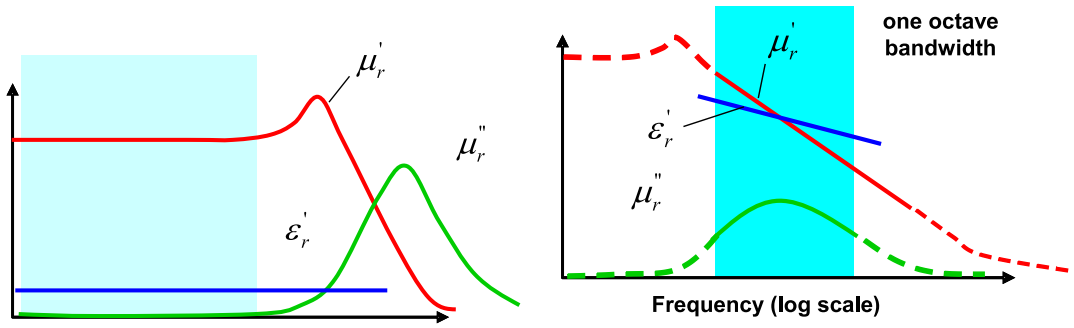

(a) High impedance surface (b) Non-conductive absorber

Figure 6.8: Desired ferrite material properties for use as a high impedance surface and as a non-conductive absorber.

the parallel combination of the characteristic impedances of these two media. The idea is the antenna acts like a generator that is driving two loads in parallel and the power split between the loads is inversely proportional to the ratio of the characteristic impedances [8]. Therefore, more power is delivered (power radiated) to the load with the smaller impedance. To deliver more power to a certain load, the permittivity of the half-space corresponding to the load can be increased or the permeability of the half-space corresponding to the other load can be increased. For an antenna backed by a cavity or ground plane, this implies that the cavity or space between the antenna and ground plane should be filled with magnetic material. In doing so, the antenna will radiate more energy away from the ground plane proportional to the difference in impedance. The advantage of this approach is that it does not take a large difference in impedance to affect the directivity of the antenna. As shown in [60] for an antenna radiating into a dielectric half-space, a difference in impedance by a factor of two has a pronounced effect on the directivity. However, this approach has several issues such

as material loss (magnetic loss tangent), weight and excitation of surface waves or resonant modes. Since the antenna is placed directly on the magnetic material, the material loss will have a significant affect on the efficiency over the entire bandwidth of the antenna. The weight of the antenna is also a major concern because of the material density and volume of material used. Lastly, pattern distortion and impedance matching issues due to the presence of surface waves or resonant modes supported by the finite volume of material are of major concern.

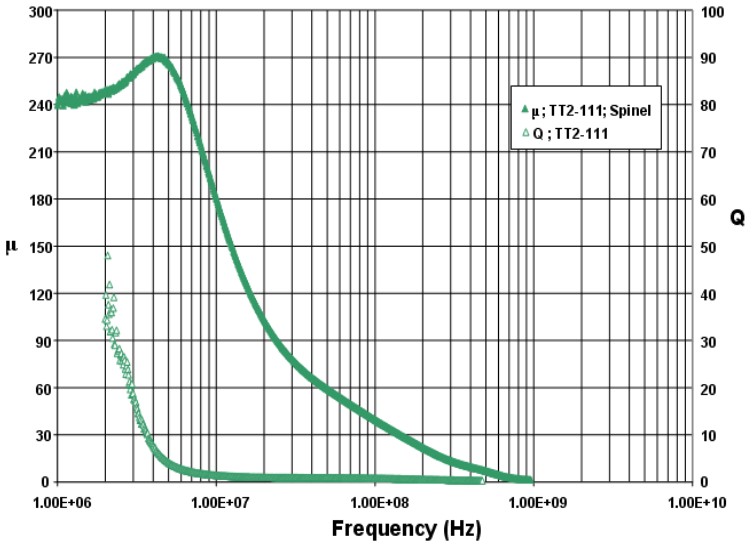

Figure 6.9: Relative permittivity and Q of some state-of-the-art magnetic materials produced by Trans-Tech. (Data provided by Trans-Tech).

Instead of redirecting the radiation, the third option absorbs energy directed toward the ground plane by filling the region with a lossy material. Ideally, the impedance of the material should be matched to free space ($\mu = \epsilon$), as shown in Figure 6.8b, so the majority of the wave can enter the material. This approach has

been commonly used in the past especially for cavity backed spirals [8]. The obvious drawback to this approach is its degradation of the radiation efficiency which depends upon the loss and volume of material. For the VHF band or lower, the most common materials that have sufficient loss are ferrites. Commonly used absorbers such as honeycomb and carbon-impregnated foam must occupy a large volume of space to be effective at these frequencies because they do not have sufficient loss. Therefore, they are not usable for low-profile antenna applications.

In light of the options presented above, it is evident that third option is the least attractive. The best option appears to be a compromise between the first and second approaches. That is, the ferrite should have $\mu_r > \epsilon_r$ over as large a frequency range as possible and the volume of material should be kept to a minimum. Based on these characteristics, a ferrite from Trans-Tech (composition number TT2-111) was found to have suitable material properties for antenna apertures larger than 6 inches in diameter. The magnetic material properties are shown in Fig. 6.9 courtesy of Trans-Tech. The dielectric constant ($\epsilon_r = 9.7$) and loss tangent ($tan\delta_\epsilon = 0.001$) are not shown but they are stable across this frequency range. For this ferrite, the frequency for which $\mu_r = \epsilon_r$ occurs at about 510 MHz. Below 510 MHz, μ_r is greater than ϵ_r as desired and the magnetic loss tangent decreases with decreasing frequency. Above 510 MHz, the ferrite behaves like an absorber because of the larger magnetic loss tangent ($tan\delta_\mu > 2$). The transition at 510 MHz from a "high-impedance" behavior to an absorptive behavior is well suited for a 6in diameter spiral because this frequency also defines the point where the spiral begins to be electrically large enough to exhibit its frequency independent behavior.

As a proof of concept, the use of this ferrite material as a high-impedance surface and backed by a PEC ground plane is examined in the remainder of this section. First, the ferrite alone is used as a high-impedance surface for an unminiaturized spiral antenna. It is shown that the ferrite itself cannot provide sufficient shielding for electronics mounted behind the ferrite. To achieve sufficient shielding, the ferrite is used in conjunction with a PEC ground plane. It is shown that the performance of the spiral antenna can be improved using a ferrite coated ground plane instead of the traditional PEC ground plane.

6.4.1 High Impedance Surface using Ferrites

To demonstrate the benefit of using ferrite material in place of the traditional PEC ground plane, a ferrite backing was constructed using seven 1 x 6.5 x 0.25 bars to form a 6.5 x 7 ferrite tile. The realized gain of an unminiaturized spiral was then measured in free-space, backed by a PEC ground plane (6.5 x 7") and by the ferrite tile. Figure 6.10 shows a comparison of the measured realized gain for these cases where the separation between the antenna and reflective surface is 1 ($\approx \lambda/24$ at 500MHz). It is clear that the gain of the spiral backed by the ferrite tile is the same as the free-standing spiral at low frequencies whereas the PEC backed spiral has considerably lower gain as expected. This clearly demonstrates the potential benefit of using ferrite material. However, there are two main issues that need to be addressed if the ferrite backing is to be a viable replacement for the PEC ground plane. The first issue is the material loss above 500MHz results in an appreciably lower gain than the free-space and PEC ground plane cases. More importantly, the

ferrite needs to provide better or equivalent shielding for electronics mounted behind it than the PEC ground plane which is the second issue.

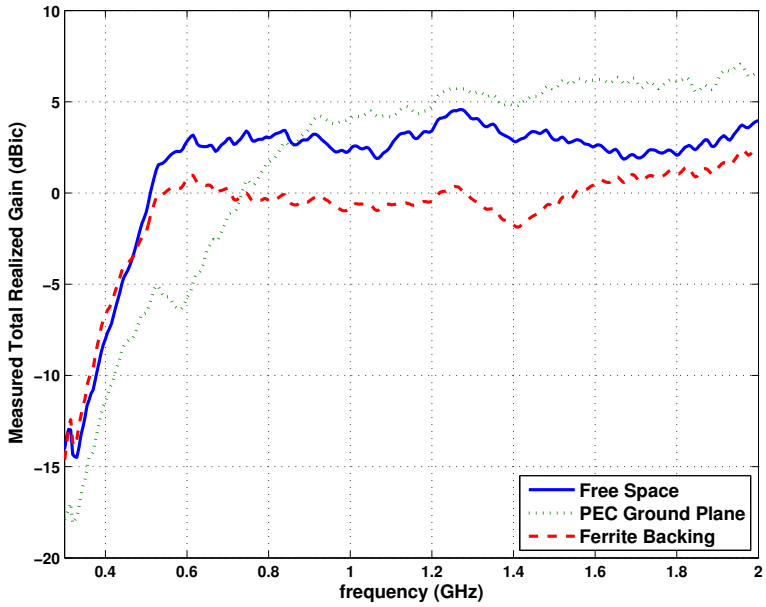

Figure 6.10: Comparison of the measured realized gain for a 6 spiral antenna with ferrite and PEC backing (1 separation in all cases).

There are two approaches that can be used to improve the gain at higher frequencies. First of all, moving the ferrite tile outside the near field of the antenna will help to improve the radiation efficiency and, therefore, the gain at higher frequencies. This is demonstrated in Fig. 6.11 where the measured realized gain is compared for a number of different spacings. As expected, the high frequency gain increases as the separation between the antenna and ferrite tile increases. Note that the free-space gain is completely recovered above 1GHz for the case where $D = 2$" ($D = \lambda/6$).

However, improving the high frequency gain by increasing the profile of the antenna is not the ideal solution.

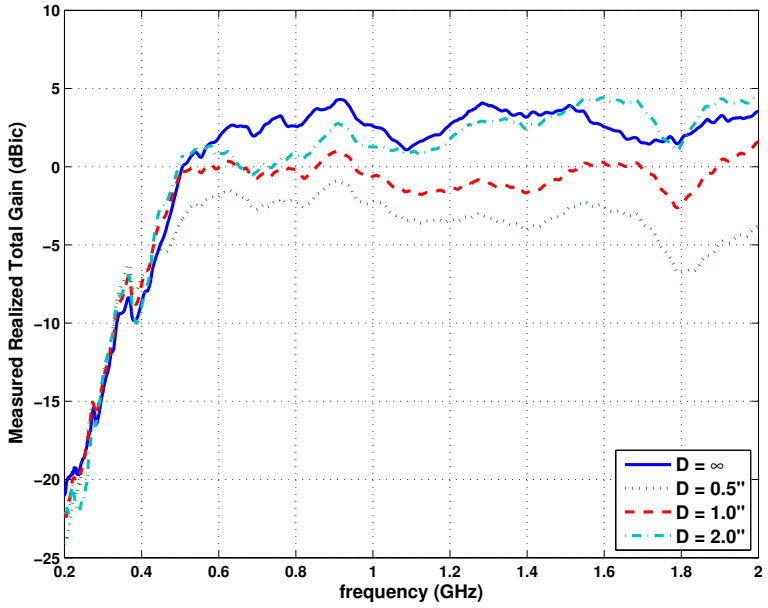

Figure 6.11: Measured realized gain of a 6 spiral antenna backed by a ferrite tile for a number of different spacings D.

Therefore, the second approach involves improving the high frequency gain while maintaining the profile. To do this, the fields of the high frequency components must be prevented from penetrating the ferrite where they are absorbed. Since the higher frequency components radiate from the center region of the spiral, the high frequency fields are predominately concentrated near the center. The obvious way to keep the fields from penetrating the ferrite is to coat the center of the ferrite with a electrically conductive material. To estimate how much of the surface needs to be coated, the measured realized gain of the spiral backed by the PEC ground plane was used. From

this result it is apparent that the PEC ground plane begins to have the highest gain at 800 MHz. Using radiation band theory, this corresponds to a four inch diameter circle. Therefore, the conductive coating should not extend beyond a radius of 2 inches and should gradually transition to the non-conductive ferrite. To realize this surface a conductive circular patch with a serrated-edge was used. The purpose of the serrated edge is to provide a transition from the conductive center to the non-conductive ferrite and to minimize diffraction from the edges. The inner and outer radius, as well as the number of serrations, were determined using an optimization process based on a Genetic algorithm coupled with a pattern search method. It is noted that in this optimization process, a PMC surface was used in place of the actual ferrite. The final patch design, shown in Figure 6.12, was made from copper tape and has an inner radius of 1.5, an outer radius of 5.2 with 27 serrations.

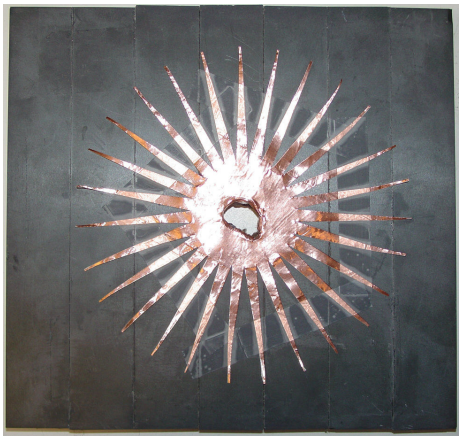

Figure 6.12: Hybrid ferrite/PEC backing.

A comparison of the measured realized gain for the spiral backed by a PEC ground plane and the hybrid ferrite/PEC backing is shown in Figure 6.13. It is apparent that

the hybrid surface provides a good compromise between the ground plane and ferrite tile alone. When compared to the ferrite alone, the hybrid surface is able to recover the free space gain almost up to 0 dBi while it significantly improves the gain above 800 MHz by more than 2 dBi.

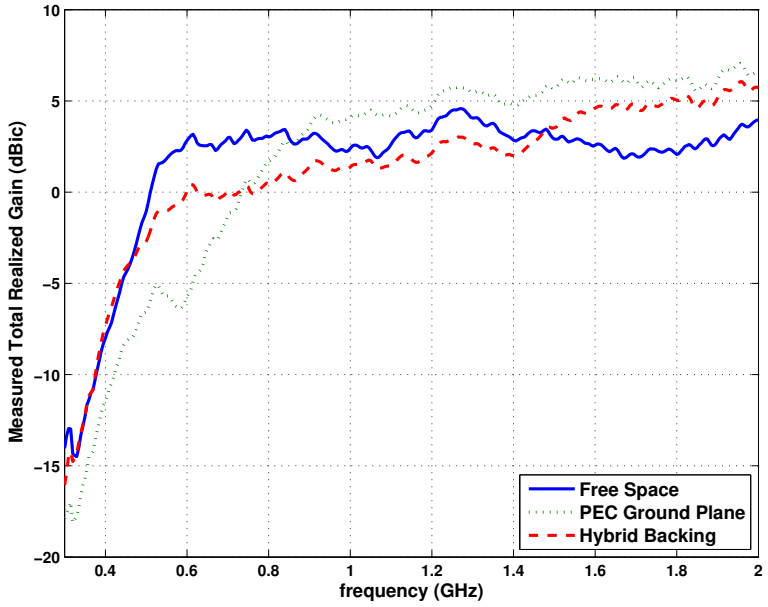

Figure 6.13: Measured realized gain for the 6 spiral antenna with hybrid backing (1 separation in all cases).

As mentioned previously, for ferrite to be used alone as a high-impedance surface, it must provide better or equivalent shielding than a PEC ground plane for electronics mounted behind it. The reflectivity of the ferrite could be measured to test its effectiveness but this would require an unreasonably large sample to measure the reflectivity down to 100 MHz or lower. Since the ferrite is being used in conjunction with an antenna, measuring the front-to-back ratio is more useful and practical option.

A comparison of the measured front-to-back ratio is shown in Fig. 6.14 for the spiral backed by a PEC ground plane and the ferrite tile without the metallic coating. Overall, the PEC ground plane has a better front-to-back ratio especially at the higher frequencies. Below 800 MHz, diffraction from the edge of the finite PEC ground plane results in more radiation toward the back. Since there appears to be little or no diffraction from the ferrite tile, it has a better front-to-back ratio at lower frequencies. However, its front-to-back ratio is at most 5 dB below 800 MHz which may not be sufficient for many applications.

One possible way to achieve a better front-to-back ratio is to combine the ferrite tile with the PEC ground plane. Furthermore, when the antenna is mounted on any platform, the presence of a ground plane around the antenna is almost unavoidable. Therefore, the following section considers how a PEC ground plane coated with a layer of ferrite would perform.

6.4.2 Ferrite Coated Metallic Ground Plane

When mounting an antenna on any platform, the presence of a conductive ground plane is inevitable. Therefore, in this section, the effect of placing a PEC surface behind the ferrite is investigated. Since the impact of the ground plane depends upon its size and shape which is in turn dependent upon the platform, two limiting cases for the ground plane size are considered. The first case considers a finite size PEC ground plane that is the same size as the antenna. The second case examines the effect of an infinite PEC ground plane with a ferrite layer that is the same size as the antenna. If sufficient performance can be achieved in these two cases then it is

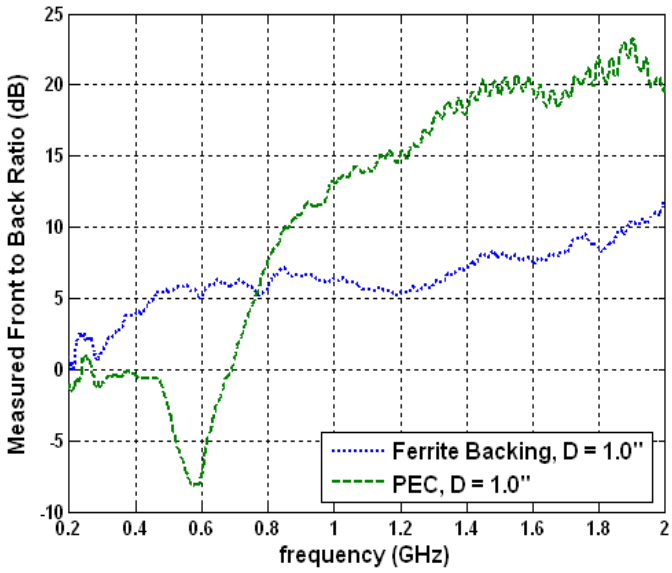

Figure 6.14: Front to back ratio comparison of the ferrite backing and ground plane.

reasonable to assume that the ferrite coated ground plane should work for any size ground plane.

Finite Ferrite Coated Ground Plane

For the finite PEC ground plane case, an unminiaturized circular 6 inch diameter spiral (see Fig. 6.1) was simulated 1" ($\lambda/24$ at 500 MHz) above a 6.25" diameter ground plane and a ferrite (Trans-Tech TT2-111) coated ground plane. The thickness of the ferrite layer is 0.25". A comparison of the total realized gain is shown in Fig. 6.15. It is evident that below 300 MHz, the ferrite coated ground plane does not perform as well as the free standing spiral. This result can be attributed to the presence of the PEC ground plane because the ferrite coated ground plane has the same realized gain as the PEC ground plane below 300 MHz. However, from 300 to 800 MHz, the realized gain of the ferrite coated ground plane is 2 to 5 dBi higher

than that obtained using the PEC ground plane. Furthermore, it is better than the free-space case over a small frequency range (400-500 MHz). Based on the return loss (see Fig. 6.16) and directivity ($>$ 2 dBi on average), the overall performance of the ferrite coated ground plane should be better than the free standing spiral over a larger frequency range. However, its performance is limited by its poor radiation efficiency (see Fig. 6.17) which also accounts for the lower realized gain above 800 MHz. Lastly, a comparison of the front-to-back ratio is shown in Fig. 6.18. It is apparent that the front-to-back ratio has improved with the addition of the PEC ground plane to the extent that it is better than the PEC ground plane over the entire frequency range.

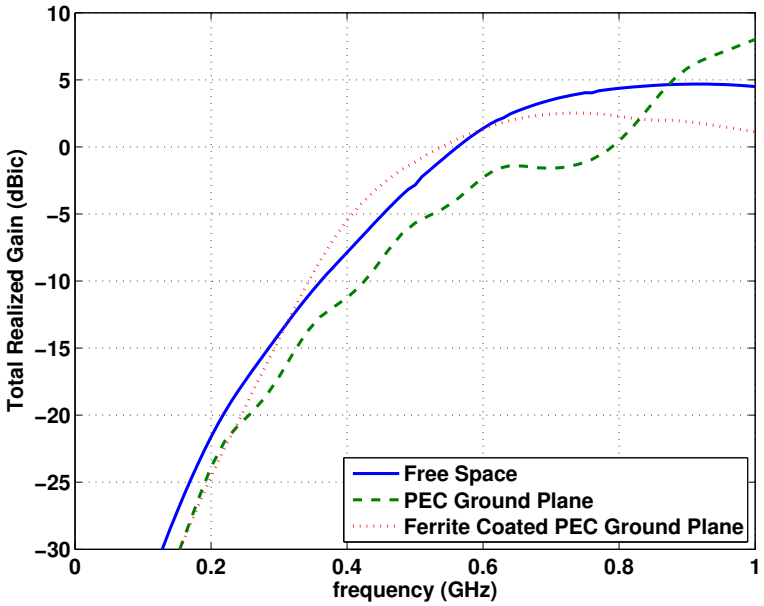

Figure 6.15: Comparison of the total realized gain (simulation result) of a spiral antenna above a finite PEC ground plane and a finite ferrite coated PEC ground plane.

Overall, the presence of a finite PEC ground plane behind the ferrite layer did not significantly depreciate the performance. Actually, the ferrite coated ground plane was able to maintain or exceed the realized gain of the free-standing spiral down to the -15 dBi gain point. For the unminiaturized spiral, this result is more than satisfactory in regards to the realized gain. The only concern with ferrite coated ground plane is the radiation efficiency. At higher frequencies the radiation efficiency can be improved by coating the top surface of the ferrite with a conductive material as shown previously. The same effect could possibly be achieved by removing some of the ferrite to expose the PEC behind it. This approach has the additional benefit of reducing the weight of the antenna. For lower frequencies, the only way to improve the radiation efficiency is to use another material that has a similar μ_r and ϵ_r but with a lower magnetic loss tangent.

Infinite Ferrite Coated Ground Plane

Having seen that the presence of a finite PEC ground plane behind the ferrite layer does not significantly affect the performance, the impact of an infinite PEC ground plane is considered. Fig 6.19 shows the previously used 6in spiral above an infinite ground plane that is partially coated with a ferrite material. The ferrite layer is 6.25 inches in diameter and 0.25 inches thick. A comparison of the realized total gain is shown in Fig 6.20 with and without the ferrite layer. Below 500 MHz, the realized gain obtained using the infinite PEC ground plane is more than 3 dBi lower than the finite case (see Fig. 6.15). Conversely, the realized gain of the infinite ferrite coated ground plane is very similar to the finite size case. Consequently, the realized gain of the ferrite coated ground plane is between 5 to 10 dBi better than the PEC ground plane. Furthermore, in comparison to the free-standing spiral, the difference in the

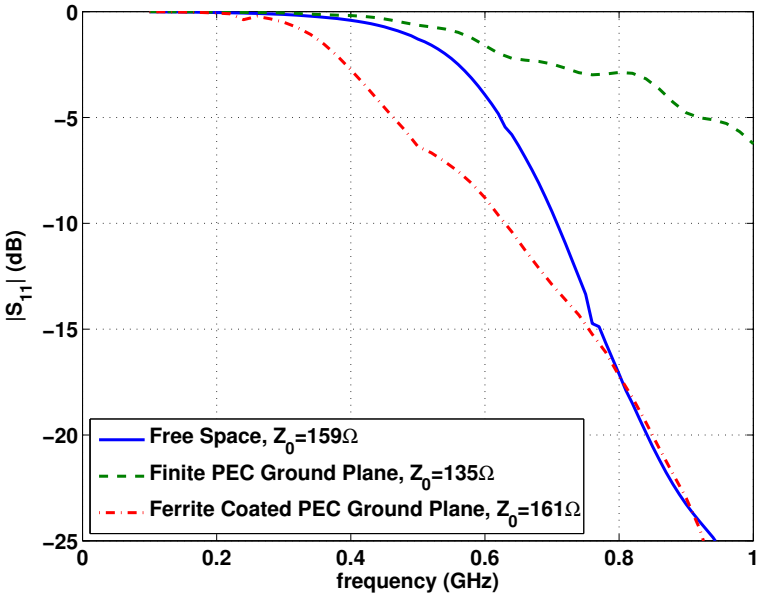

Figure 6.16: Comparison of the return loss (simulation result) of a spiral antenna above a finite PEC ground plane and a finite ferrite coated PEC ground plane.

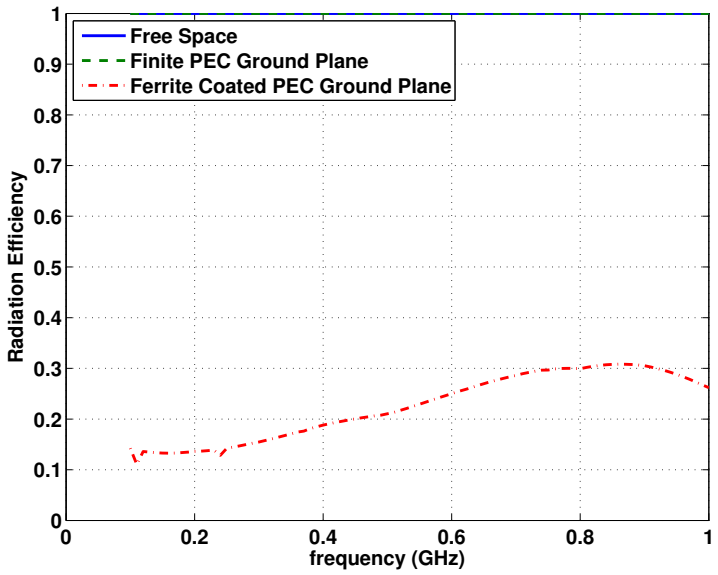

Figure 6.17: Comparison of the radiation efficiency (simulation result) of a spiral antenna above a finite PEC ground plane and a finite ferrite coated PEC ground plane.

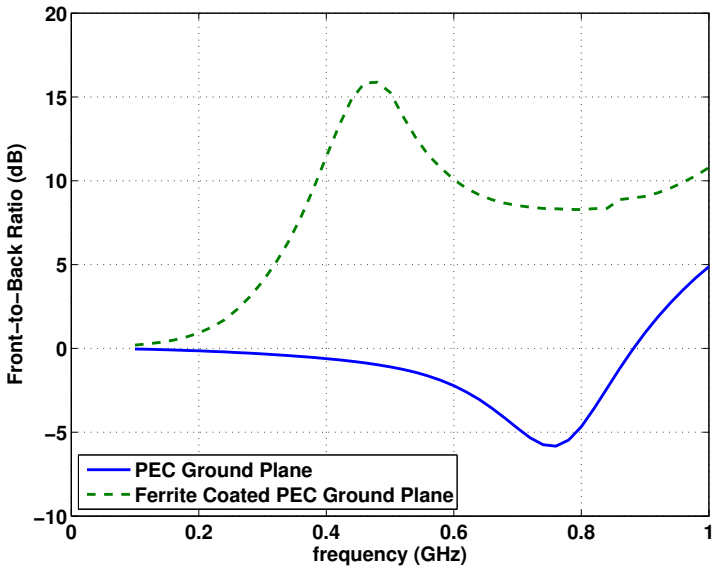

Figure 6.18: Comparison of the front-to-back ratio (simulation result) of a spiral antenna above a finite PEC ground plane and a finite ferrite coated PEC ground plane.

realized gain is relatively the same as it was for the finite case. With regards to this result, it appears that the ferrite coated ground plane is relatively unaffected by the size of the PEC ground plane behind it.

6.4.3 Potential Future Improvements

Before proceeding with the integration of the ferrite coated ground plane with the miniaturized spiral from chapter 5, it is worthwhile to consider how the thickness and material properties of the ferrite affect the performance. In doing so, insight can be gained into potential improvements that can be made for future designs. To start, the effect of the ferrite layer thickness is examined using the previous infinite PEC ground plane setup (see Fig. 6.19). The original or baseline design was a 0.25" thick

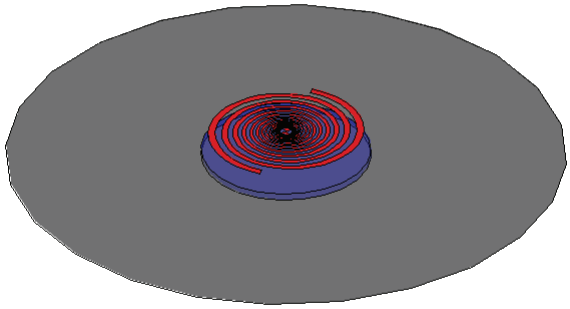

Figure 6.19: Spiral antenna above an infinite PEC ground plane partially coated with a ferrite material.

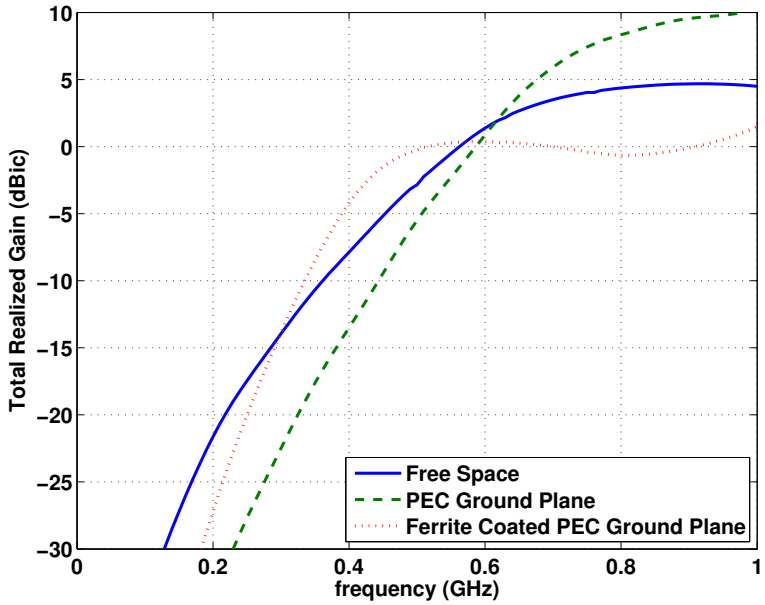

Figure 6.20: Comparison of the total realized gain for a spiral in free-space, backed by an infinite PEC ground plane and backed by a ferrite coated ground plane.

which corresponds to an electrical thickness of about $\lambda_0/100$ at 500 MHz. In terms of the guided wavelength λ_g $\left(\lambda_g = \lambda_0/\sqrt{\epsilon_r \mu_r}\right)$, the thickness is about $\lambda_g/10$ at 500 MHz. Therefore, the baseline thickness is relatively thin which helps to minimize the weight of the antenna. To demonstrate the impact of the thickness, two additional thicknesses were considered which are 0.125" and 0.5". The effect of the ferrite layer thickness on the total realized gain is shown in Fig 6.21. It is evident that increasing the thickness improves the realized gain at lower frequencies (below 500 MHz) but makes it worse at higher frequencies (above 500 MHz). Conversely, decreasing the thickness improves the gain at higher frequencies but leads to a lower gain at lower frequencies.

The trend at higher frequencies is a result of the radiation efficiency improving as the thickness decreases. This trend makes sense because less material should lead to less absorption. This is especially true at higher frequencies where the magnetic loss tangent of the ferrite can be up to four times larger than it is at lower frequencies. The trend observed at low frequencies by increasing the thickness is consistent with the behavior alluded to in [8]. That is, if the region between the antenna and ground plane is filled with a high impedance material, more radiation should be directed away from the ground plane which in turn should improve the directivity in the forward direction.

The observed trend implies the possibility of improving the design by tapering the thickness of the ferrite. That is, instead of using a uniformly thick disk of ferrite, the thickness should be tapered in the radial direction starting with zero thickness at the center and finishing with a maximum thickness t_{max}. In doing so, the low frequency realized gain can be further improved using a thickness greater than 0.25" while

concurrently improving the radiation efficiency at higher frequencies. Furthermore, it may be possible to accomplish this using the same volume of ferrite material as the original design and, therefore, the weight of the antenna will remain unchanged. In light of this, such a design needs to be considered in the future.

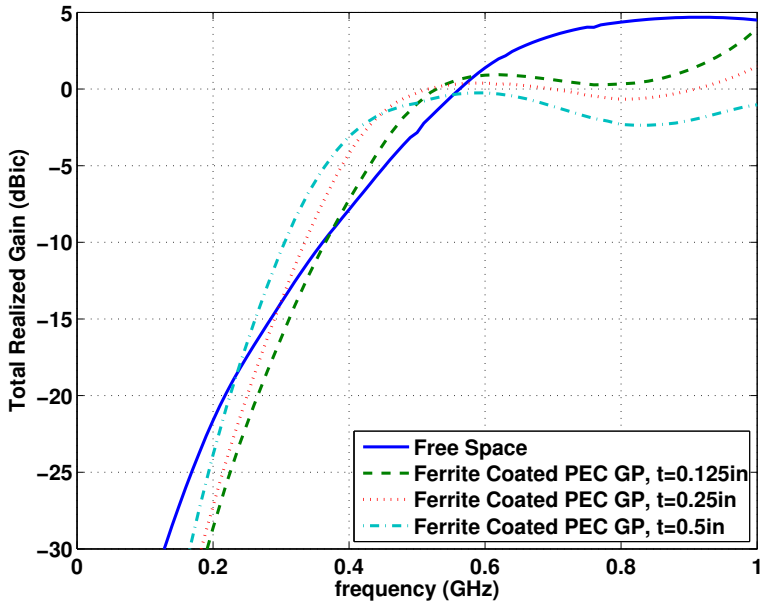

Figure 6.21: Impact of ferrite layer thickness t on the total realized gain for a spiral backed by a ferrite coated ground plane.

6.5 Integration of Ferrite Coated PEC Ground Plane with Miniaturized Spiral

In the previous section an unminiaturized spiral was used to demonstrate the potential benefits of using a ferrite coated ground plane in place of the traditional metallic (PEC) ground plane. The focus of this section is the integration of the ferrite coated ground plane with the miniaturized 6" (see Fig. 5.22 in section 5.4) and 18"

(see Fig. 5.30 in section 5.5) spirals from the previous chapter. The following section discusses the integration with the 6" spiral and the subject of last section is the 18" design.

It is important to note that, for both spiral designs, the integration process was predominately experimental because of difficulties in simulating the entire antenna design. That is, method of moments (MOM) is efficient and extremely accurate when simulating the miniaturized spiral in free-space. However, when finite material volumes are included, it becomes difficult to get accurate results in an efficient manner unless a Green's function approach is used. However, the Green's function approach requires the material layers to be infinite in extent. Analyzing the problem using the finite element method (FEM) also presents problems because it requires an incredibly large number of unknowns to accurately model the fine details of wire spiral structure in addition to the material volumes. In fact, the number of unknowns is so large that it makes simulation on a current desktop PC (3 GHz dual-core processor with 2 GB of RAM) impractical. Therefore, the simulation results presented in this section are used to validate the experimental results.

6.5.1 6" Diameter Spiral for UHF Operation

Since the previous demonstration of the ferrite coated ground plane utilized a 6" unminiaturized spiral, integration with the miniaturized 6" spiral was a relatively straight forward process. To begin, the final configuration of the fabricated miniature low-profile spiral is shown in Fig. 6.22b. The spiral element shown in Fig. 6.22a was fabricated using a 0.25 inch thick Rogers TMM4 laminate ($\epsilon_r = 4.5, tan\delta = 0.002$). It was suspended 1 inch above the ferrite coated ground plane, resulting in a total

thickness of 1.5 inches since the ferrite layer was 0.25 inch. The entire antenna is enclosed by a PVC side wall. The antenna element and FCGP are secured to the PVC side wall using epoxy. In addition to the epoxy, the FCGP was further secured using a layer of fiber-glass. A top view of the PVC cavity showing the ferrite layer and the 1.5" diameter copper patch is provided in Fig. 6.22c. The ground plane was constructed using copper tape to coat the back surface of the ferrite and it is shown Fig. 6.22d.

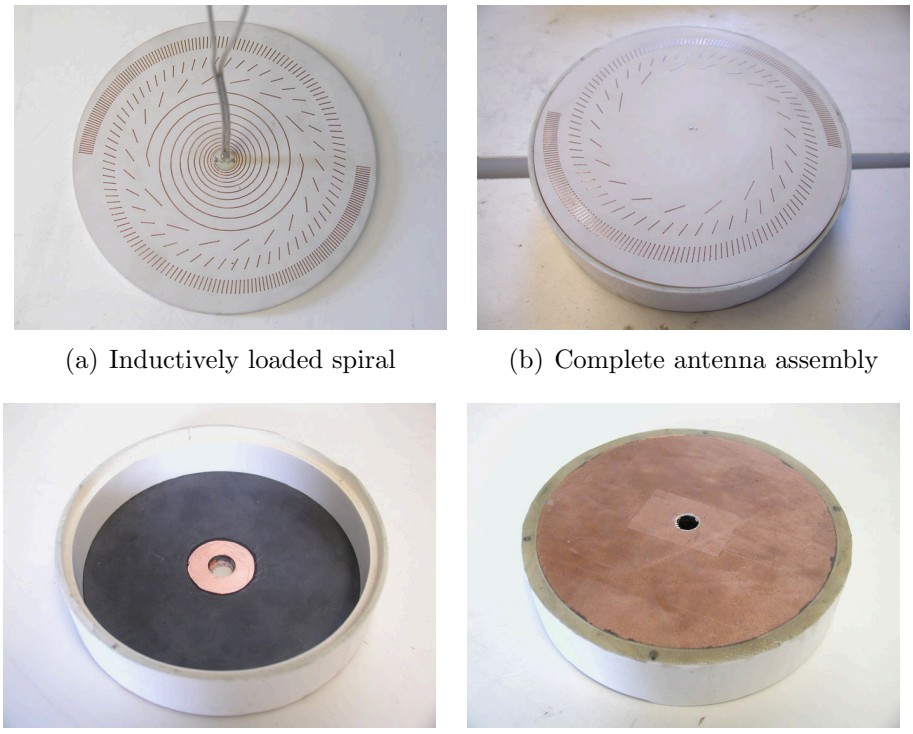

(a) Inductively loaded spiral (b) Complete antenna assembly

(c) Inside PVC cavity (d) Bottom view of antenna

Figure 6.22: Photos of the fabricated 6" inductively loaded spiral antenna. (a) Bottom side of the inductively loaded spiral PCB. (b) Top side of the complete antenna assembly showing the PVC cavity. (c) View of the PVC cavity showing the ferrite material and copper patch on top of the ferrite. (d) Bottom view of the antenna cavity showing the copper ground plane.

Fig. 6.23 shows the measured total realized gain for the miniaturized spiral itself and when placed above the FCGP. Also shown is the measured realized gain of an unminiaturized 6" diameter spiral above a copper ground plane (6" diameter). The measured return loss is shown in Fig. 6.24. It is evident that the realized gain for spiral backed by the FCGP is almost identical to the free-standing spiral above 300 MHz. Below 300 MHz, the two curves begin to diverge. This trend is very similar to what was observed for the unminiaturized antenna in section 6.4.2. In comparison to the free-standing spiral, the miniaturized spiral above the FCGP achieves a gain of -15dBi at about 190 MHz instead of 170 MHz for the free-standing spiral. Despite this degradation, the unminiaturized spiral with a metallic ground plane (-15 dBi gain at 340 MHz) would have to be about 1.82 times larger in diameter (11 inches) to achieve the same performance. It is also remarked that at 190 MHz the aperture size of the antenna is $\lambda_0/10$ and the profile is only $\lambda_0/40$.

The spacing between the antenna element and FCGP was determined experimentally by measuring the realized gain for a variety of spacings that ranged from 0.5" to 1.5". A comparison of some of the measurements is shown in Fig. 6.25. Each case is delineated by its total height h or profile. Since the ferrite and antenna element are both 0.25" thick, the separation between them is h minus 0.5". From Fig. 6.25 it is evident that, for the given heights, only the realized gain above 1 GHz is affected by the height. Over this frequency range, a height of 1.5" provides the best trade-off between recovering the free-space realized gain while maintaining a low-profile.

In an attempt to improve the high frequency gain, a copper patch was placed on the top surface of the ferrite as in section 6.4.2. The optimum size of the reflective copper patch was determined experimentally by measuring the realized gain for a

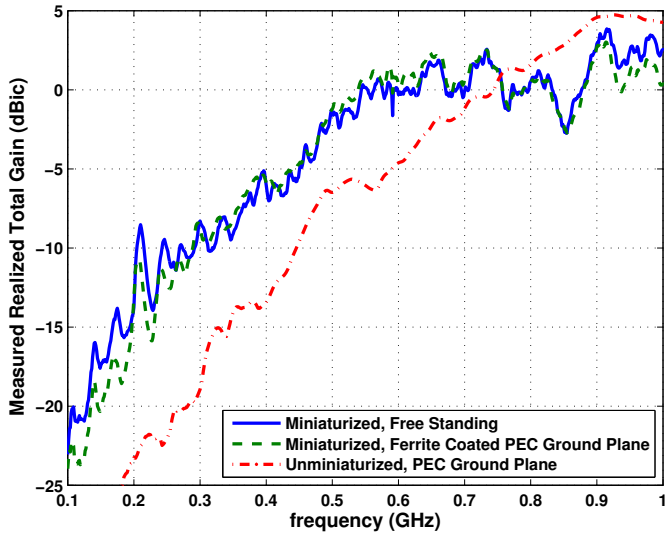

Figure 6.23: Measured Realize gain of the inductively loaded (miniaturized) spiral with and without the ferro-metallic ground plane as compared to unloaded (unminiaturized) spiral backed by a copper ground plane.

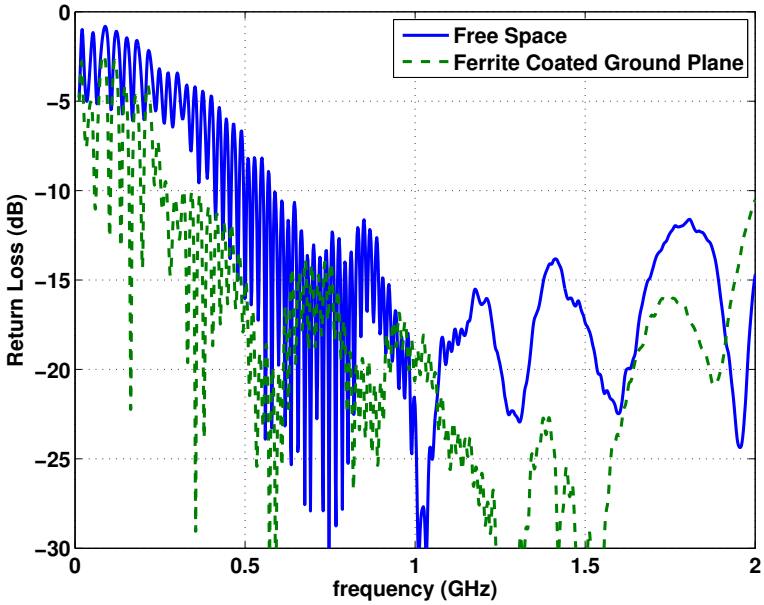

Figure 6.24: Measured return loss of the inductively loaded (miniaturized) spiral with and without the ferro-metallic ground plane.

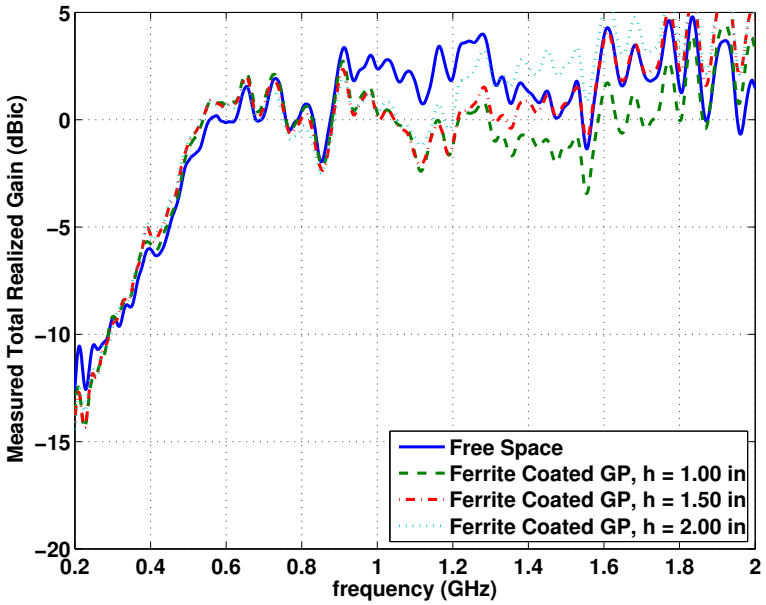

Figure 6.25: Optimum spacing between the 6" miniaturized spiral and ferrite coated ground plane based on measured realized gain.

variety of diameters ranging from 1.5" to 3". Fig. 6.26 shows a comparison of the measurements for a diameter of 1.5" and 3". It is apparent that the 3" diameter patch increases the gain at higher frequencies at the expense of reducing the gain at lower frequencies. As the diameter is made smaller, the gain increases less at higher frequencies and the gain at lower frequencies recovers to the case without a patch as expected. The 1.5" diameter patch provides the best trade-off but it does not significantly enhance the realized gain. Furthermore, it was found that adding a serrated edge to the patch had a negligible effect. Therefore, the benefit of using the copper patch is questionable. However, since the 1.5" copper patch has a negligible effect, it maybe possible to remove some of the ferrite, exposing the ground plane behind the ferrite, without impacting the realized gain. This would reduce the weight

of the antenna which is extremely beneficial especially for airborne applications where payload is crucial.

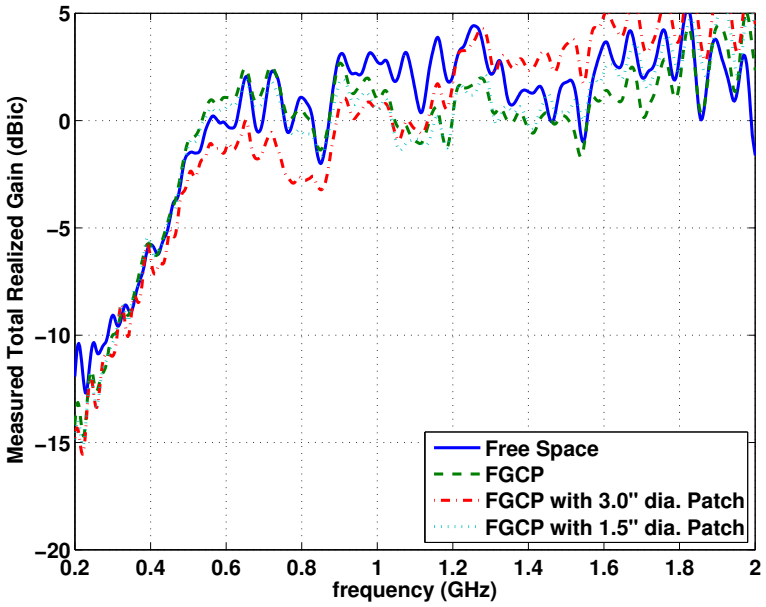

Figure 6.26: Optimum copper patch size for the 6" miniaturized spiral based on measured realized gain.

To validate the experimental results, FEKO was used to simulate the 6" miniaturized spiral with the FCGP using two different approaches. The first approach uses the planar Green's function to take into account the FCGP and the Rogers TMM4 substrate. As mentioned previously in section 5.4, the Green's function approach is used to overcome the difficulty in simulating the coiled spiral in a finite dielectric medium. In this approach, the use of the planar Green's function requires the material layers to be infinite in extent. Therefore, this approach is mainly useful for

providing a "first order" approximation to the actual finite antenna design. Regardless, this approach is extremely efficient and provides a practical way for optimizing the material properties of the ferrite in the future. The total realized gain obtained from FEKO using the planar Green's function is shown in Fig. 6.27 for the miniaturized spiral in free space, above an infinite PEC ground plane and above an infinite FCGP (0.25 inch thick ferrite layer). As expected, below 500 MHz the realized gain is significantly lower for the PEC ground plane case because of the lower mismatch efficiency. However, the gain obtained using the FCGP is nearly identical to the free space case. In fact it is slightly higher because of the infinite size of the FCGP. In general, the result agrees reasonably well with the experimental result.

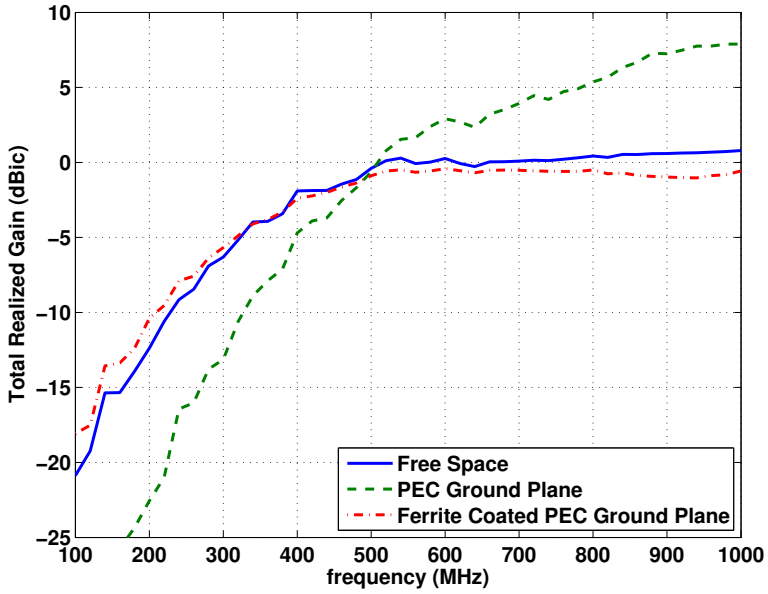

Figure 6.27: FEKO simulation result for the total realized gain of the miniaturized 6 inch diameter spiral when placed above an infinite PEC ground plane and an infinite ferrite (Trans-Tech TT2-111) coated ground plane.

For the second approach, the Rogers TMM4 substrate is excluded from the simulation which allows the FCGP to be finite in extent. The exclusion of the Rogers TMM4 substrate mainly affects impedance matching which can easily be accounted for by properly adjusting the matching condition. A comparison of the simulated and measured total realized gain for the finite size FCGP is shown in Fig. 6.28. For the simulation, the mismatch efficiency was calculated using an impedance of about 142Ω instead of 100Ω to account for the absence of the TMM4 substrate. Clearly, the simulated and measured results agree extremely well which validates the FEKO simulation and the design.

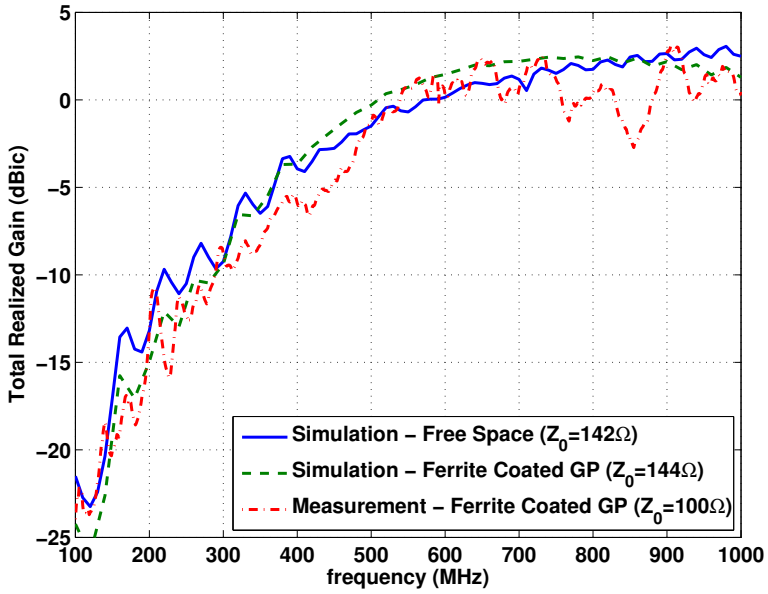

Figure 6.28: FEKO simulation result for total realized gain of the miniaturized 6 inch diameter spiral when placed above a finite ferrite (Trans-Tech TT2-111) coated PEC ground plane.

6.5.2 18" Diameter Spiral for VHF and UHF Operation

In section 5.5 a baseline for the performance of the 18" antenna was established by measuring it in free space. The purpose of this section is to discuss the integration of this antenna with the FCGP and how it performs in comparison to the free-standing antenna. The assembled antenna is shown in Fig. 6.29 which consists of the antenna itself, a custom machined aluminum ground plane, a custom made plastic ABS sidewall or radome (see Fig. 6.30) and a 0.25" thick layer of Trans-Tech TT2-111 ferrite. The ground plane, ABS sidewall and ferrite layer are more clearly shown in Fig. 6.30 in addition to the the 5" diameter copper patch on the top surface of the ferrite. The ferrite layer was constructed from 23 individual tiles (4" x 4" x 0.25") which were cut to form an 18 inch diameter circle using a diamond blade. Additionally, a hole was made in the center of the disk to accommodate the feeding cable and the ferrite was attached to the ground plane using epoxy. The ground plane was machined from a piece of aluminum by a local machine shop (Kyron Tool and Machine Co.). It is 21 inches in diameter and the center section (19 inches in diameter) has been recessed 0.375 inches to accommodate the ferrite and provide additional support for the ABS sidewall. the plastic sidewall was fabricated by bending and joining two strips of 0.5 inch thick ABS plastic to form a cylinder that has an inner diameter of 18 inches, an outer diameter of 19 inches and is 3.375 inches in height. The ABS sidewall was attached to the aluminum ground plane using a combination of screws and epoxy.

The measured realized gain of the 18 inch spiral with the FCGP is shown in Fig. 6.31 in addition to the antenna in free space and above a PEC ground plane. It can clearly be seen that the ferrite ground plane offers significant improvement over the PEC ground plane below 300 MHz as expected. However, below 200 MHz, the

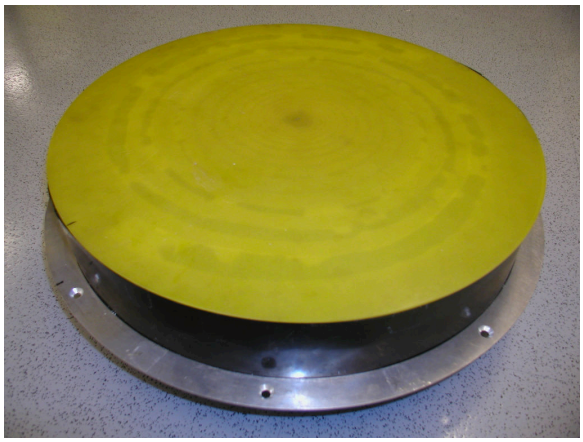

Figure 6.29: Picture of the 18 inch diameter spiral showing the complete antenna.

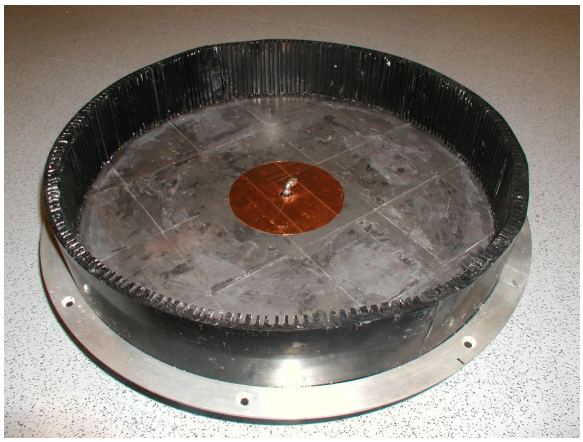

Figure 6.30: Picture of the enclosure for the 18 inch diameter spiral showing the ferrite coated (Trans-Tech TT2-111) aluminum ground plane, the black plastic (ABS) sidewall and the 5" diameter copper patch.

gain for the ferrite ground plane case is worse than the free standing spiral which contradicts the result obtained for the six inch spiral in section 6.5.1. It is believed that the reason for this discrepancy can be attributed to the electrical thickness of the ferrite layer. That is, assuming that the initial operating frequency for the 6" spiral is 150 MHz, the ferrite has a $\mu_r \approx 34$ and $\epsilon_r \approx 9.6$ at 150 MHz which results in an electrical thickness of about $\lambda_g/20$. Since scaling the aperture size by a factor of three corresponds to a shift in the operating frequency by a factor of three, the initial operating frequency for 18" spiral should be 50 MHz. At 50 MHz the ferrite has a $\mu_r \approx 60$ and $\epsilon_r \approx 9.6$ which corresponds to an electrical thickness of about $\lambda_g/40$. Therefore, compared to the 6" design, the electrical thickness of the ferrite layer at the initial operating frequency is half as thick. There are two ways to increase the electrical thickness. First, the thickness of the material could be increased at the expense of increasing the weight. Since the current antenna already weights close to 25 lbs, this is not an attractive option because it is estimated that by doubling the thickness of the ferrite the antenna would weight close to 40 lbs. A better option is to find a more suitable material that has a larger μ, ϵ or both. If a more suitable material can't be found, then the next best option is to consider a tapered thickness design using the current ferrite as mentioned in section 6.4.3.

The only other way to improve the low frequency gain using the current configuration is to increase the separation between the antenna and the ferrite ground plane. From Fig. 6.32 it is apparent that increasing the separation from 3 inches to 6 inches is sufficient to almost completely recover the free space gain below 200 MHz. However, this approach is not as appealing as finding a more suitable ferrite material or a tapered thickness design using the current ferrite.

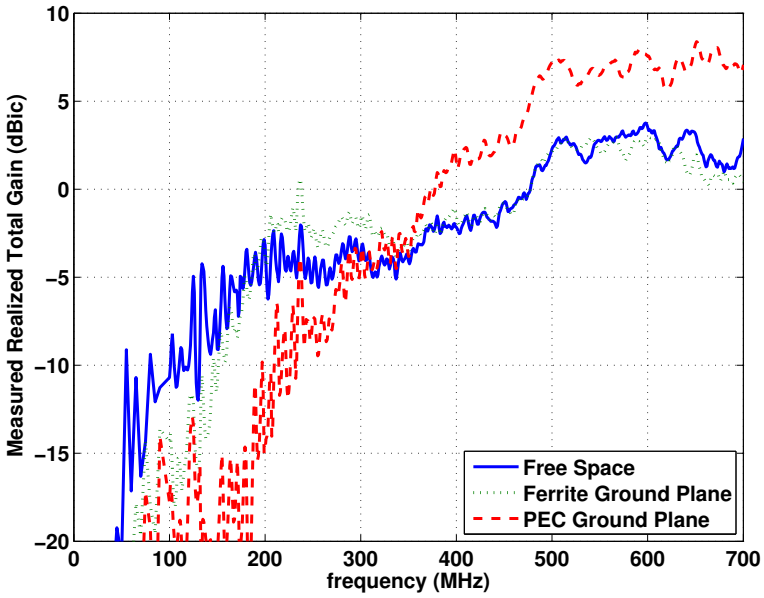

Figure 6.31: Comparison of the measured realized gain of the 18" inductively loaded (miniaturized) spiral with the ferrite coated ground plane (3" separation), a traditional copper ground plane (3" separation) and free-standing.

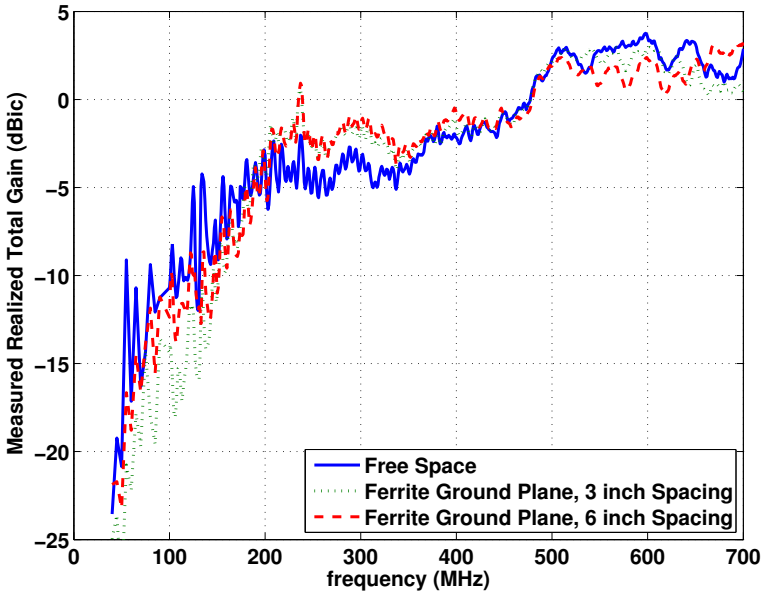

Figure 6.32: Comparison of the measured realized gain of the 18" inductively loaded (miniaturized) spiral backed by the ferrite coated ground plane with a separation of 3 inches and 6 inches.

Shifting the focus from the low frequency gain, an attempt was made to improve the high frequency gain by introducing a metallic patch on top of the ferrite as in section 6.4.1. To determine the new patch geometry, a series of measurements were made using a circular patch and varying the diameter from 4 to 9 inches. The separation between the antenna and ground plane was 3 inches in all cases. It was observed that the gain above 500 MHz could be increased by increasing the size of the patch but at the expense of decreasing the gain between 200 and 500 MHz. Based on this trade-off, the optimal diameter was determined to be 5 inches. Also, it was found that using a serrated edge, as in section 6.4.1, offered no improvement. Therefore, the resulting patch geometry was a five inch diameter circle, as shown in Fig. 6.30, and the improvement obtained from the addition of this patch is shown in Fig. 6.33. It is apparent that the inclusion of the patch eliminated the gain drop around 800 MHz caused by the ferrite which is about a 3 dB improvement. However, this caused a minor reduction (about 1 dB) in the gain between 200 and 300 MHz.

6.6 Summary

In this chapter, the performance degradation caused by an electrically small separation between a metallic ground plane and antenna element was addressed. Alternatives to the metallic ground plane were considered such as EBG structures and ferrite materials. For the miniaturized spiral, EBG structures were deemed to be unsuitable because of bandwidth limitations and size requirements. It was found that a ferrite coated ground plane (FCGP) provided a more suitable solution to the problem. Using a commercially available ferrite from Trans-Tech (TT2-111), it was demonstrated using simulations and measurements that the FCGP could almost completely recover

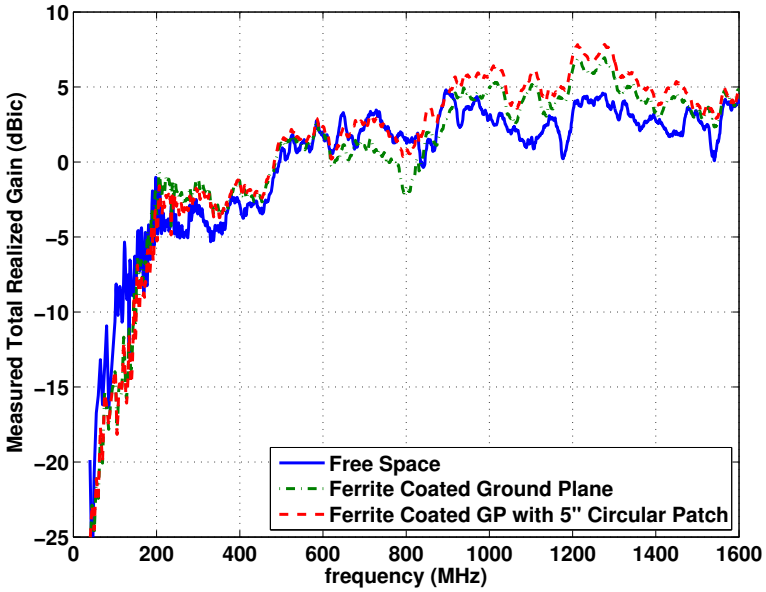

Figure 6.33: Comparison of the measured realized gain of the 18" inductively loaded (miniaturized) spiral backed by the ferrite coated ground plane with and without a 5" diameter copper patch.

the free-space realized gain of the miniaturized 6" spiral. For the larger 18" spiral, it was observed that the performance obtained using the FCGP was not as good as the free standing spiral because of the frequency dependent material properties of the ferrite. However, the performance was still better than the spiral backed by a traditional metallic ground. It is believed that with proper selection of the material properties and thickness of the ferrite layer this issue can be overcome in future designs.

CHAPTER 7

CONCLUSION

7.1 Summary and Conclusions

In this thesis, the size reduction of an UWB antenna was examined. The objective was two fold. The primary goal was to reduce the aperture size of an antenna using miniaturization techniques such as material loading and reactive loading. The secondary objective was to minimize the antenna profile without sacrificing performance. The primary objective was the focus of Chapters 2 through 5 and the secondary objective was the subject of Chapter 6.

Specifically, in Chapter 2 the fundamental limitations on antennas were used to determine the extent to which the size of an UWB antenna could be reduced and still achieve a specified level of performance. This was accomplished using the minimum Q antenna concept (Chu-Wheeler Q limit) and Fano-Bode matching theory. By combining these concepts, a relation was derived for a high-pass system response to determine the minimum electrical size (cut-off size or frequency) that could achieve a given realized gain or in-band reflection coefficient. Essentially, this relation established a theoretical limit for how much size reduction or miniaturization could be achieved.

Taking the miniaturization limit into consideration, Chapters 3 through 5 focused on the size reduction of preexisting UWB antenna designs through the application of miniaturization techniques. In particular, Chapter 3 discussed the concept of antenna miniaturization in general by using a dipole antenna to illustrate the importance of phase velocity and electrical size with regards to radiation. It was shown that, by controlling the phase velocity via miniaturization techniques, the dipole could resonate at frequencies where it is electrically too small to do so naturally. By establishing resonance at a given ka, it was shown that the radiation Q, radiation resistance and impedance bandwidth of the electrically small antenna were improved significantly. However, the improvement was limited by the electrical size (Chu-Wheeler Q limit) as expected and the antenna design itself. This observation illustrated a crucial point about miniaturization which is, for a given ka, miniaturization techniques can improve the performance of an antenna but they cannot overcome the limitations of the antenna design itself. That is, reducing the phase velocity of an arbitrary antenna design will not turn it into a minimum Q antenna. Therefore, the ideal minimum Q antenna performance cannot be achieved using miniaturization alone. In addition to discussing antenna miniaturization in general, the proper method of reducing the phase velocity, using either material or reactive loading, for an UWB antenna was also discussed. Using a spiral antenna, it was shown that the loading should be concentrated in the low frequency region since loading the high frequency region has adverse effects. Furthermore, the loading should be introduced gradually (tapered) to prevent possible discontinuities that may result in additional adverse effects. Using this approach or methodology, the performance of the spiral could be improved at

frequencies where it is electrically small ($ka < 1$) while minimizing degradation at frequencies where it is electrically large ($ka > 1$).

Using the results from Chapter 3, Chapters 4 and 5 focused on the design, analysis, fabrication and measurement of a miniaturized spiral antenna using material (dielectric) loading and reactive (inductive) loading respectively. It was demonstrated that both approaches alone could be used to achieve the same amount of miniaturization (about 55% reduction in size). From this perspective, neither dielectric loading or inductive loading can be considered superior to the other. However, based on practical considerations such as weight, ease of fabrication and surface waves, inductive loading was found to be more advantageous. The implementation and optimization of the inductive loading was discussed in depth in Chapter 5. The spiral antenna was inductively loaded using a novel method that involved coiling the spiral arm such that it resembled a helix. It was shown that this approach could achieve more miniaturization than tradiational planar meandering at the expense of increasing fabrication complexity. This inductive loading approach was applied to the design of a 6" and 18" diameter spiral. Both designs were extensively optimized and were able to achieve a miniaturization factor of about 2.15 (based on -15 dBi realized gain point) which corresponds to a size reduction of about 54%. This compares well to the theoretical miniaturization limit of 2.9 ($\approx 65\%$) which is for a minimum Q antenna that utilizes the entire volume of the radian sphere. Since the miniaturized spiral only occupies about 6% of the volume of the radian sphere, its performance is rather remarkable.

Finally, in Chapter 6 a new ground plane concept was presented to overcome adverse effects caused by an electrically small separation between an antenna and a metallic ground plane. The proposed ground plane consisted of a traditional metallic

ground plane coated with a layer of ferrite material (Trans-Tech TT2-111). It was demonstrated, using simulations and measurements, that the reduction in realized gain caused by the presence of a metallic ground plane could almost be eliminated by using the ferrite coated ground plane (FCGP). Therefore, the realized gain of the miniaturized 6" spiral above the FCGP (1 inch separation) was almost the same the free-standing miniaturized spiral. Furthermore, this was achieved using a total height or profile of 1.5 inches which corresponds to an electrical size of only $\lambda/40$ at the lowest frequency of operation (about 170 MHz). However, it was observed that for larger aperture sizes the performance obtained using the FCGP was not as good as the free standing case because of the frequency dependent material properties of the ferrite. However, the performance was still better than a spiral backed by a traditional metallic ground and this issue can be overcome in future designs with proper selection of the ferrite material properties and layer thickness.

7.2 Future Work

Opportunities for future work involve new low Q antenna designs, further refinement of the inductively loaded spiral design and developing a further understanding of the ferrite coated ground plane concept. These subjects are discussed in more detail in the following sections.

7.2.1 Low Q Antenna Designs

This thesis focused on the application of antenna miniaturization techniques to preexisting antenna designs to approach the limits discussed in Chapter 2. The problem with this approach is that preexisting antenna designs such as the spiral do not utilize the entire volume of the radian sphere which encloses it. In fact,

the miniaturized spiral designs of chapter 5 only occupy around 6% of the available volume. In order to approach the limit discussed in section 2.6, the Q of the antenna must approach the Chu-Wheeler Q limit. This can only be accomplished by utilizing the entire volume of the radian sphere such that there is no stored energy inside the sphere of radius a and only the lowest spherical modes exist outside it (TM_{01} and TE_{01}) [2]. Therefore, to come closer to the limit, future work should focus on creating original antenna designs that can achieve a lower Q and better performance.

It is remarked that the subject of achieving the Q limit has already been examined to some extent. Most notably, Harold Wheeler has proposed two antenna designs that could come close to the Q limit for a single mode but not reach it without the use of high-contrast materials [16, 72]. The antennas proposed by Wheeler are the spherical inductor and spherical cap dipole which are illustrated in Fig. 7.1. Wheeler predicted that the spherical inductor could achieve a Q three times the theoretical limit and the spherical cap dipole could achieve a Q 1.5 times the limit [16, 72]. To some extent, this has been verified by Thal [46] and Lopez [72]. It is interesting to note that in theory, only the spherical inductor with a perfect magnetic core ($\mu_r = \infty$) can achieve the Q limit for $ka << 1$ [16, 46]. In view of these findings, the work by these authors should be examined in more detail to gain insight into the design of low Q antennas.

7.2.2 Inductively Loaded Spiral Design

Based on the discussion in section 7.2.1, it is believed that the low frequency performance of the exponential pitch taper spiral design can not be improved upon in a significant way. However, there is room for improvement in other areas. The most notable is overcoming the fabrication limitations which prohibit the use of the

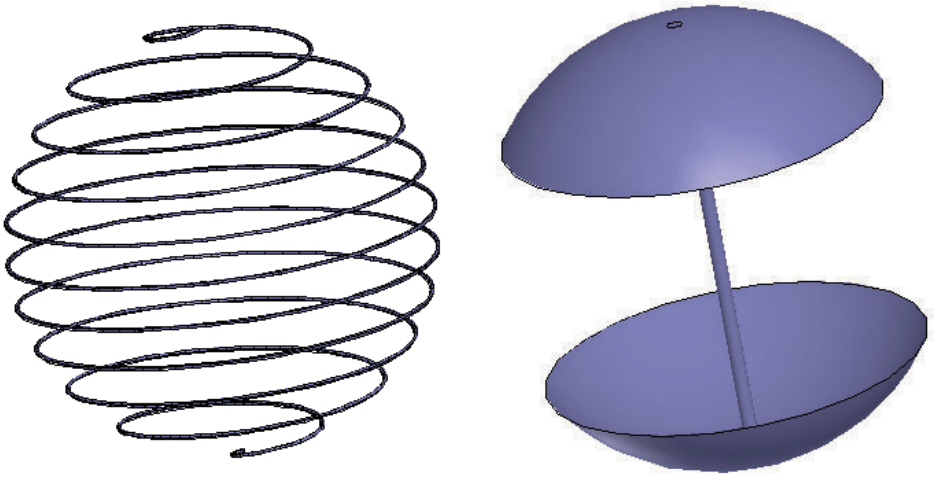

(a) Spherical Inductor (b) Spherical Cap Dipole

Figure 7.1: Wheeler's proposed low Q antennas. *a*) Spherical inductor antenna for excitation of TE_{01} mode. *b*) Spherical cap dipole antenna for excitation of TM_{01} mode.

exponential pitch taper design for aperture sizes greater than 14 inches. As mentioned in section 5.6, this can be accomplished by reducing the thickness of the coil by either using the pitch to compensate for a reduction in thickness or embedding the coil in a magneto-dielectric material. A thinner coil design also has the additional benefit of reducing the substrate thickness. The thinner substrate will help to alleviate surface wave issues which will occur at higher frequencies and reduce the weight of the antenna.

7.2.3 Optimization of Ferrite Coated Ground Plane

In this thesis, the discussion on the ferrite coated ground plane was not comprehensive in scope or theory. The idea was presented as a proof of concept to illustrate

its potential. Therefore, a more comprehensive and rigorous analysis is needed to determine the optimal material parameters and to better understand the phenomena. By doing so, the proper ferrite material can be selected for use in a given frequency band which, currently, limits the scalability of the entire antenna design. That is, the spiral can easily be scaled to operate over any frequency range with the proper performance but the ferrite coated ground plane cannot.

As mentioned in section 6.4.3, another opportunity for future work is in the shaping or tapering of the ferrite material. The current design employs a ferrite layer with a uniform thickness. It might be possible to achieve the same performance by tapering the thickness of the ferrite layer. That is, the ferrite layer can be made thinner near the center of the ground plane (high frequency region) where it is not necessarily needed. By doing so,the weight of the antenna could be reduced significantly since the ferrite layer constitutes more than half of the antennas weight. If this is possible, such a design would considerably improve its applicability to airborne applications especially UAVs which have a very limited payload.

BIBLIOGRAPHY

[1] A. R. Lopez, "Review of narrowband impedance-matching limitations," *IEEE Antennas and Propagation Magazine*, vol. 46, no. 4, pp. 88–90, August 2004.

[2] L. J. Chu, "Physical limitations of antenna Q," *Journal of Applied Physics*, vol. 19, p. 11631175, December 1948.

[3] R. F. Harrington, *Time-Harmonic Electromagnetic Fields*. John Wiley & Sons, Inc., 2001.

[4] R. M. Fano, "Theoretical limitations on the broadband matching of arbitrary impedances," Ph.D. dissertation, Massachusetts Institute of Technology, 1947.

[5] D. Kern, D. Werner, A. Monorchio, L. Lanuzza, and M. Wilhelm, "The design synthesis of multiband artificial magnetic conductors using high impedance frequency selective surfaces," *IEEE Transactions on Antennas and Propagation*, vol. 53, no. 1, pp. 8–17, January 2005.

[6] F. Yang and Y. Rahmat-Samii, "Reflection phase characterizations of the ebg ground plane for low profile wire antenna applications," *IEEE Transactions on Antennas and Propagation*, vol. 51, no. 10, pp. 2691–2703, October 2003.

[7] T. J. Talty, D. Yingcheng, and L. Lanctot, "Automotive antennas: trends and future requirements," *IEEE Antennas and Propagation Society International Symposium*, vol. 1, p. 430433, July 2001.

[8] R. H. DuHamel and J. P. Scherer, "Frequency-independent antennas," in *Antenna Engineering Handbook*, 3rd ed., R. C. Johnson, Ed. McGraw-Hill, Inc., 1993, ch. 14, pp. 18–25.

[9] A. Gangi, S. Sensiper, and G. Dunn, "The characteristics of electrically short, umbrella top-loaded antennas," *IEEE Transactions on Antennas and Propagation*, vol. 13, no. 6, pp. 864–871, November 1965.

[10] S. R. Best, "A discussion on the properties of electrically small self-resonant wire antennas," *IEEE Antennas and Propagation Magazine*, vol. 46, no. 6, pp. 9–22, December 2004.

[11] ——, "On the resonant properties of the koch fractal and other wire monopole antennas," *Antennas and Wireless Propagation Letters*, vol. 1, no. 1, pp. 74–76, 2002.

[12] H. A. Wheeler, "The radian sphere around a small antenna," *Proceedings of the I.R.E.*, vol. 35, p. 13251331, August 1959.

[13] S. A. Schelkunoff, "A mathematical theory of linear arrays," *Bell System Tech. J.*, vol. 22, pp. 80–107, 1943.

[14] T. T. Taylor, "A discussion of the maximum directivity of an antenna," *Proc. I.R.E.*, vol. 36, p. 1135, 1948.

[15] R. P. Feynman, R. Leighton, and M. Sands, *The Feynmen Lectures on Physics: Volume 1.* Addison-Wesley, 1961.

[16] H. A. Wheeler, "Fundamental limitations of small antennas," *Proceedings of the I.R.E.*, vol. 35, pp. 1479–1484, December 1947.

[17] R. F. Harrington, "Effect of antenna size on gain, bandwidth, and efficiency," *J. Res. Nat. Bureau Stand.*, vol. 64D, pp. 1–12, January 1960.

[18] J. S. McLean, "A re-examination of the fundamental limits on the radiation Q of electrically small antennas," *IEEE Transactions on Antennas and Propagation*, vol. 44, no. 5, pp. 672–676, May 1996.

[19] R. E. Collin and S. Rothschild, "Evaluation of antenna Q," *IEEE Trans. Antennas Propagat.*, vol. AP-12, pp. 23–27, January 1964.

[20] R. L. Fante, "Quality factor of general idea antennas," *IEEE Trans. Antennas Propagat.*, vol. AP-17, pp. 151–155, March 1969.

[21] R. C. Hansen, "Fundamental limitations in antennas," *Proceedings IEEE*, vol. 69, pp. 170–182, February 1981.

[22] D.-H. Kwon, "On the radiation Q and the gain of crossed electric and magnetic dipole moments," *IEEE Transactions on Antennas and Propagation*, vol. 53, no. 5, pp. 1681–1687, May 2005.

[23] R. F. Harrington, "On the gain and beamwidth of directional antennas," *I.R.E. Transactions Antennas Propagation*, vol. AP-6, pp. 219–225, January 1958.

[24] R. C. Hansen, *Electrically Small, SuperDirective, and Superconducting Antennas.* John Wiley & Sons, Inc., 2006.

[25] R. L. Fante, "Maximum possible gain for an arbitrary ideal antenna with specified quality factor," *IEEE Trans. Antennas Propagat.*, vol. 40, no. 12, pp. 1586–1588, December 1992.

[26] W. Geyi, "Physical limitations of antenna," *IEEE Transactions on Antennas and Propagation*, vol. 51, no. 8, pp. 2116–2123, August 2003.

[27] J. McLean, H. Foltz, and R. Sutton, "Conditions for direction-independent distortion in UWB ANTENNAS," *IEEE Transactions on Antennas and Propagation*, vol. 54, no. 11, pp. 3178–3182, November 2006.

[28] D. M. Pozar, "Polarization of maximum gain antennas," *IEEE Transactions on Antennas and Propagation*, vol. 55, no. 7, pp. 2113–2115, July 2007.

[29] B. A. Munk, *Finite Antenna Arrays and FSS*. John Wiley & Sons, Inc., 2003.

[30] H. J. Carlin, "Network theory without circuit elements," *Proceedings of the IEEE*, vol. 55, no. 4, pp. 482–497, April 1967.

[31] D. C. Youla, L. J. Castriota, and H. J. Carlin, "Bounded real scattering matrices and the foundations of linear passive network theory," *I.R.E. Transactions on Circuits Theory*, vol. CT-6, pp. 102–124, March 1959.

[32] G. Nedlin, "Energy in lossless and low-loss networks, and Fosters reactance theorem," *IEEE Transactions on Circuits and Systems*, vol. 36, no. 4, pp. 561–567, April 1989.

[33] R. M. Foster, "A reactance theorem," *Bell Syst. Tech. J.*, vol. 3, p. 259, 1924.

[34] H. W. Bode, *Network Analysis and Feedback Amplifier Design*. D. Van Nostrand Co., 1945.

[35] R. M. Fano, "Limitations on the broadband matching of arbitrary impedances," *Journal of the Franklin Institute*, vol. 249, no. 1, pp. 57–83 & 139–154, January & February 1960.

[36] A. R. Lopez, "Wl multiple tuning techniques," Hazeltine Wheeler Laboratory Memorandum, Tech. Rep. G300-73-RL9012, January 1973.

[37] D. M. Pozar, *Microwave Engineering*, 2nd ed. John Wiley & Sons, Inc., 1998.

[38] G. L. Matthaei, L. Young, and E. M. T. Jones, *Microwave Filters, Impedance-Matching Networks and Coupling Structures*. McGraw-Hill Book Company, Inc., 1964.

[39] H. A. Wheeler, "Wideband impedance matching," Wheeler Labs, Tech. Rep. 418, May 1950, report is available at http://www.arlassociates.net.

[40] ——, "The wide-band matching area for a small antenna," *IEEE Transactions on Antennas and Propagation*, vol. AP-31, no. 2, pp. 364–367, March 1983.

[41] D. K. Cheng, *Field and Wave Electromagnetics*, 2nd ed. Addison-Wesley Publishing Company, Inc., 1989.

[42] H. J. Carlin and R. L. Rosa, "Broadband reflectionless matching with minimum insertion loss," in *Proc. Symp. Modern Network Synthesis*, New York, N. Y., April 1952.

[43] E. N. Gilbert, "Impedance matching with lossy components," *IEEE Transactions on Circuits and Systems*, vol. CAS-22, no. 2, pp. 96–100, February 1975.

[44] S. A. Schelkunoff, "Theory of antennas of arbitrary size and shape," *Proceedings of the I.R.E.*, vol. 29, no. 9, pp. 493–521, September 1941.

[45] J. D. Kraus and R. J. Marhefka, *Antennas*, 3rd ed. McGraw-Hill, Inc., 2001.

[46] H. L. Thal, "New radiation Q limits for spherical wire antennas," *IEEE Transactions on Antennas and Propagation*, vol. 54, no. 10, pp. 2757–2763, October 2006.

[47] G. S. Smith, "Teaching antenna radiation from a time-domain perspective," *The American Journal of Physics*, vol. 69, no. 3, pp. 288–300, March 2001.

[48] C. A. Balanis, *Advanced Engineering Electromagnetics*, 2nd ed. John Wiley & Sons, Inc., 1997.

[49] D. S. Filipovic and J. L. Volakis, "Broadband meanderline slot spiral antenna," *IEE Proceedings. Microwaves, Antennas and Propagation*, vol. 149, no. 2, pp. 98–105, April 2002.

[50] G. J. Burke, E. K. Miller, and A. J. Poggio, "The Numerical Electromagnetics Code (NEC) - a brief history," *Antennas and Propagation Society International Symposium, 2004 IEEE*, vol. 3, pp. 2871–2874, June 2004.

[51] A. D. Yaghjian and S. R. Best, "Impedance, bandwidth, and q of antennas," *IEEE Transactions on Antennas and Propagation*, vol. 53, no. 4, pp. 1298–1324, April 2005.

[52] R. Bawer and J. J. Wolfe, "The spiral antenna," *I.R.E. International Convention Record*, March 1960.

[53] B. H. Burdine, "The spiral antenna," Massachusetts Institute of Technology, Research Laboratory Technical Report, Tech. Rep., April 1955.

[54] G. G. Bush, "Generalization of snoek's limit for modeling initial permeability of magnetic materials," *Journal of Applied Physics*, vol. 63, no. 8, pp. 3765–3767, April 1988.

[55] J. L. Snoek, "Dispersion and absorption in magnetic ferrites at frequencies above one Mc/s," *Physica*, vol. 14, no. 4, pp. 207–217, May 1948.

[56] M. W. Nurnberger and J. L. Volakis, "Extremely broadband slot spiral antennas with shallow reflecting cavities," *Electromagnetics*, vol. 20, no. 4, pp. 357–376, July 2000.

[57] B. A. Kramer, M. Lee, C.-C. Chen, and J. L. Volakis, "Design and performance of an ultrawide-band ceramic-loaded slot spiral," *IEEE Transactions on Antennas and Propagation*, vol. 53, no. 7, pp. 2193–2199, July 2005.

[58] R. G. Corzine and J. A. Mosko, *Four Arm Spiral Antennas*. Artech House, 1990.

[59] D. B. Rutledge, D. P. Neikirk, and D. Kasilingam, "Integrated-circuit antennas," in *Infrared and Millimeter Waves*, K. J. Button, Ed. Academic Press, 1983, vol. 10, pp. 1–90.

[60] G. S. Smith, "Directive properties of antennas for transmission into a material half-space," *IEEE Transactions on Antennas and Propagation*, vol. AP-32, no. 3, pp. 232–246, March 1984.

[61] N. G. Alexopoulos, P. B. Katehi, and D. B. Rutledge, "Substrate optimization for integrated circuit antennas," *IEEE Transactions on Microwave Theory and Techniques*, vol. MTT-31, no. 7, pp. 550–557, July 1983.

[62] M. Lee, C.-C. Chen, and J. L. Volakis, "Ultra-wideband antenna miniaturization using distributed lumped element loading," *IEEE Antennas and Propagation Society International Symposium*, vol. 1B, pp. 549–552, July 2005.

[63] J. Rashed and C. T. Tai, "A new class of wire antennas," *IEEE Transactions on Antennas and Propagation*, vol. 39, no. 9, p. 14281430, September 1991.

[64] J. E. Rowe, *Nonlinear Electron-Wave Interaction Phenomena*. Academic Press Inc., 1965.

[65] G. E. Forsythe, M. A. Malcolm, and C. B. Moler, *Computer Methods for Mathematical Computations*. Prentice-Hall, 1976.

[66] R. P. Brent, *Algorithms for Minimization without Derivatives*. Englewood Cliffs, New Jersey: Prentice-Hall, 1973.

[67] *Genetic Algorithm and Direct Search Toolbox*, The MathWorks, Inc., 2007, http://www.mathworks.com/access/helpdesk/help/toolbox/gads/.

[68] C. A. Balanis, *Antenna Theory: Analysis and Design*. John Wiley & Sons, Inc., 1989.

[69] J. M. Bell, M. F. Iskander, and J. J. Lee, "Ultrawideband hybrid EBG/ferrite ground plane for low-profile array antennas," *IEEE Transactions on Antennas and Propagation*, vol. 55, no. 1, pp. 4–12, January 2007.

[70] B. A. Munk, *Frequency Selective Surfaces: Theory and Design*. John Wiley & Sons, Inc., 2000.

[71] J. M. Bell and M. F. Iskander, "A low-profile archimedean spiral antenna using an EBG ground plane," *IEEE Antennas and Wireless Propagation Letters*, vol. 3, pp. 223–226, 2004.

[72] A. R. Lopez, "Fundamental limitations of small antennas: Validation of wheeler's formulas," *IEEE Antennas and Propagation Magazine*, vol. 48, no. 4, pp. 28–36, August 2006.